A biologically-inspired eye model for testing oculomotor control theories

by

Mahkameh Lakzadeh

B.A.Sc., University of British Columbia, 2008

A THESIS SUBMITTED IN PARTIAL FULFILLMENT
OF THE REQUIREMENTS FOR THE DEGREE OF

Master of Applied Science

in

THE FACULTY OF GRADUATE STUDIES
(Mechanical Engineering)

The University Of British Columbia
(Vancouver)

January 2012

Abstract

This research presents a new biologically motivated robotic model of the human eye. The model incorporates aspects of the anatomy that are functionally important for understanding biological oculomotor systems. The 3DOF robotic eye is driven by 6 DC motors through low friction dyneema cables. The DC motors represent muscle actuation while dyneema cables represent the 6 extraocular muscles (EOM). The globe's natural orbital support is emulated by a low-friction gimbal structure that supports the eye on the anteroposterior axis at the back of the globe, where there is no tendon interference. Moreover, we have used the Buckingham Π theorem dimensionless analysis to scale the geometric and dynamic properties of the biological eye according to the model's specified dimensions and inertia. Lastly, to confirm the functionality of the eye and to verify that the initial design requirements have been satisfied, we have implemented a controller design to drive this redundant (6 actuators, 3 DOF) system.The presented robotic eye model is to be employed as a test bed for testing theories about oculomotor control. Furthermore, this system could also be used to assess proposed surgical corrections for various oculomotor diseases.

Table of Contents

List of Tables

List of Figures

Glossary

VOR	vestibulo-ocular reflex
EOM	extraocular muscles
IP	insertion point
AZ	annulus of zinn
BTSC	ball terminated set screw
MI	moment of inertia
MR	medial rectus
LR	lateral rectus
SR	superior rectus
IR	inferior rectus
SO	superior oblique

IO	inferior oblique
AD	analog to digital convertor
DA	digital to analog convertor

Acknowledgments

I wish to extend my sincerest gratitude to my supervisors, Dr. Antony Hodgson and Dr. Dinesh Pai for their continuous support and inspiration. Under their supervision and guidance, I have grown intellectually and professionally and for that I will always be grateful. I also thank them for providing me with research fellowship and the equipment necessary for completing my thesis.

To my colleagues in the sensorimotor lab, Mr. Garrett Jones, Dr. Shinjiro Sueda, Mr. Sanghoon Yeo, Mr. Martin Lesmana, Dr. Timothy Edmunds and Mr. David Levin, you have become dear friends that I will cherish always. Thank you for your supporting hand, knowledge, and friendship over the past few years. I have learned many things from you and will always hold dear, memories of my time with you. To my dear friend Marius, whom I have had the pleasure of knowing since the start of my studies at UBC. You have been a constant encouragement, who has pushed me to become more passionate about my career. Thank you for helping me grow spiritually and professionally. To my dear friends Sama Ghnaim and Jeanie Chan, I extend my deepest appreciation for your continuos support and friendship.

I wish to thank my dear husband Hamed, whose unconditional support and love has kept me going throughout the years. Thank you for all the sleepless nights that you spent by my side. I have never met a more generous and loving person than you and I am truly grateful to have you in my life. Thank you for making me be a better version of myself.

Finally, I wish to extend my love and gratitude to my parents, who have selflessly devoted their lives to bettering mine. Thank you for making impossibles possible, thank you for allowing me to grow on my own while guiding me in the right direction, and most importantly thank you for teaching me the true meaning of unconditional love. For all this and more, I will always be indebted to you. To my loving sister Pardis, you are my best friend and companion and I wouldn't want to imagine life without you. Thank you for believing in me even when I don't.

Chapter 1

Introduction

1.1 Motivation

Vision is a remarkable sensing capability which allows humans and other animals to perceive the world in great detail. It is clear that the use of this sense is essential for our ability to quickly assess our surrounding world and determine what actions to take to achieve our goals. Blindness, through retinal or optical nerve damage, is perhaps the most obvious failure of our visual system; nevertheless, malfunctions of our oculomotor system (i.e. the system that controls our eye movement), could prove to be equivalently impairing.

Although it may not be apparent, our ability to perceive the world is greatly dependant on the movement of our eyes; this sets biological visual systems apart from cameras. It is a curious fact that in order for us to see, we first need to recognize that there is something worth looking at [18, 29, 67]. Consequently,

our eyes are constantly in motion, both to stabilize the visual image on the retina and to move the fovea to objects of interest using fast saccadic eye movements. Saccades are necessary for our visual awareness because like a number of other animals humans have high clusters of visual receptors on an area $1mm$ in diameter, known as the fovea, at the centre of our field of view. Therefore to achieve maximum visual acuity the fovea needs to be directed onto the area of interest. Vestibulo-ocular reflex is another eye movement that facilitates a clear visual field by counteracting head motions by moving the eye in the opposite direction. The necessity of this movement becomes evident during activities such as walking or running during which our visual field remains unaffected despite the constant up and down movements of our head.

Much of the work for identifying the mechanisms of these eye movements are done in physiology labs, where neural connections are traced out and their responses to various stimuli are measured. However, to test their plausibility, theories about the neurology of eye movements must be tested by engineers on physical eye models. Such models have been developed for various body parts; for instance, Matsuoka et al. [36] has created a robotic index and thumb finger to study the motor control of human hand. In addition, to study the physical mechanics of the human jaw, Stavness et al. [55] have created an anatomically accurate, dynamic computer model of the human jaw.

Furthermore, understanding the tight integration between how we move our eyes and what we perceive is critical to understanding how certain diseases or injuries affect vision as well as finding potential solutions for treating these condi-

tions. One such condition is strabismus, where the eyes are not aligned with each other and thus their gazes are positioned on 2 different points in space which could prevent proper binocular vision and depth perception. Strabismus could either be the result of a brain malfunction or lack of coordination in the EOMs which could arise with age [9, 30]. Consequently, if our diagnoses lead to proposed surgical corrections, we will often want an accurate patient-specific model of the eye in order to perform simulated surgeries to determine the optimal outcome. While it is theoretically possible to build a purely virtual model for the vision system, it is wise to validate such models against real physical systems to ensure that no surprising un-modelled effects emerge, such as unaccounted dynamic properties or friction. Furthermore, in certain circumstances it maybe very difficult to simulate all the inputs which will be experienced in real life and in these situations it is necessary to have an accurate physical model of the vision system.

Finally, insights obtained from biology could aid the future development of robotic eyes and for such applications in robotics there must be tests performed on real physical systems. vestibulo-ocular reflex (VOR) is one example of biological eye movement that would have practical applications in robotics. VOR is the eye movement in response to head motion whereby the eyes are moved in the opposite direction of the head motion thus, stabilizing the image on the retina. Understanding and implementing such control strategies would be very favourable in stabilizing camera images in a moving robot; a process which would require testing on a physical model.

1.2 Problem Statement

The steps required for transforming theories about various computational neuroscientific models into facts can be represented by Figure 1.1. Specifically, known characteristics of a sensorimotor system, including its anatomy and control strategies are used to construct an anatomically accurate physical model, which consists of a geometrically accurate robot controlled by a biologically inspired control algorithm. Subsequently, known behaviors of the biological system will be implemented on the constructed model and its results will be compared to biological data to verify theories. Furthermore, a physical model could also help to uncover unknown behaviors of a sensorimotor system that could not be easily determined theoretically. Ultimately, the goal of such research is to reveal how our central nervous system controls our body movements.

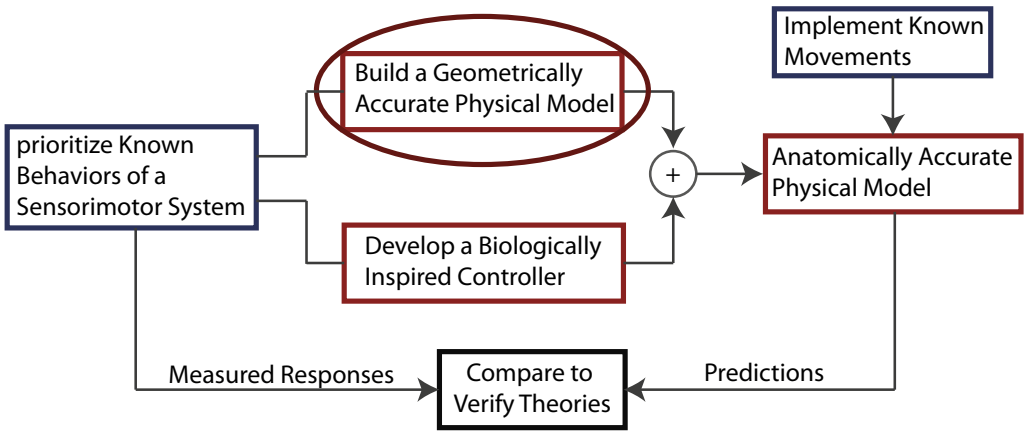

Figure 1.1: Verifying known biological theories using physical models

This same method is applied to the study of the oculomotor system. Eye move-

ments are actuated by what appears to be a simple system of three agonist and antagonist muscle pairs. This implication of tractability has attracted many scientists and neurobiologists to the subject of eye movement over the years. As a result, there are more theories about the neurology of eye movements than of any other human movements. However, even though much is known about oculomotor physiology [32], many aspects of the mechanics of the eye, its musculature, and how it is controlled remain poorly understood (e.g., see [16] for a taste of the current controversies). Therefore, the study of this sensorimotor system would benefit from a physical model to unravel the unknown facts and confirm or dispute existing theories.

The research presented in this thesis is focused on creating a geometrically accurate robotic eye to be used as a testbed for studying the oculomotor system. As discussed above, in addition to a geometrically correct robot, an anatomically accurate model must also include a biologically-inspired control algorithm. However, this is beyond the scope of this thesis and thus development of a biological controller and implementing the various eye movements are left as future work.

1.3 Literature Review

Most current robotic visual systems are used purely as sensors that provide visual information, and so their designs are focused mostly on the mechatronic performance rather than biologically realistic movement [1–3, 7, 28, 42, 45, 68].

For instance, Pongas et al. [45], have designed a set of miniature eyes to be implemented in a humanoid doll. Two miniature CMOS cameras are placed in

spherical supports and a single motor-gear system controls their horizontal movement simultaneously. Two similar systems are responsible for the vertical movement of each individual eye. Mechanisms similar to the Pongas doll eyes have been created by other groups, including Asfour et al. [2] and Beira et al. [7]. Both Asfour and Beira have created 3DOF pair of eyes to be used in their humanoid robots. However, contrary to the model developed by Pongas et al. [45], these eyes have a common tilt controlled by a motor through a belt and separate pans, again driven by a motor through belt.

Yet another tilt/pan robotic eye unit has been developed by Miwa et al. [42] for their humanoid robot (WE-4). Once again, the tilt for both of the Miwa eyes are controlled by 1-DOF while their pan is controlled by 2-DOF. Tilt is driven by a belt mechanism through a DC motor and 2 other DC motors rotate the eyes horizontally using a tendon driven system and torsional springs.

There are also some visual systems that are inspired by the perceptual development used by humans, and specifically cognitive development in infants. For example, Zhang et al. [68] has produced a vision system that develops its vision gradually. This robot is capable of distinguishing objects from one another, tracking objects as well as understanding the relation between various objects. Such models are therefore more concerned with the visual processing component of vision rather than eye movements.

Thus to conclude, none of the vision units discussed above have focused on replicating the biological details that are responsible for human eye movements, features that are crucial if the model is to be used in scientific research or clinical

applications.

1.3.1 Other Eye Models

Although emulating the anatomy of human eyes is not typically included in the development of visual systems for robots, a few biologically inspired robotic eyes have been created for the purpose of scientific research. Most notable is the 2D physical model MAC-EYE, developed by Biamino et al. [8]. The MAC-EYE was designed with the intention of creating a tendon driven mechanism capable of implementing Listing's Law[1] and therefore, it incorporates human like kinematics and actuation properties. More specifically, this robotic eye is composed of a sphere, held in place by a low friction support, actuated by four DC motors through cables that represent the four recti muscles of the eye. However, since the MAC-EYE has been built for researching a specific ocular phenomenon, it lacks some essential features for testing a broader range of the existing oculomotor theories. In particular, it lacks the oblique muscles and even though the obliques may not be necessary for Listing's Law-compatible movements, many eye movements such as ocular counter-roll and combined eye-head movements violate Listing's Law. Furthermore, the MAC-EYE does not include an accurate placement of the tendons on the globe, a feature that is believed to have significant impact on oculomotor control [49].

Wang et al. [63] have recently constructed a biologically inspired robotic eye.

[1]Listing's Law states that all eye orientations that are achievable from a given initial gaze direction are reached by rotating the eye about a set of corresponding axes that lie on a specific plane

Unlike the MAC-EYE, this robotic eye has 3 Degrees of Freedom (DOF) and it is driven by 3 pairs of agonist/antagonist Pneumatic Artificial Muscles (PAMs). This Robotic eye is supported by a ball joint located in the centre of the globe. However, the chosen design and assembly process of this joint enforces a non-spherical globe shape, resulting in an inaccurate geometrical representation. In addition, the length-force properties of PAMs were tuned based on data from skeletal muscles which have been proven to be very different from EOMs [46]. Furthermore, similar to the MAC-EYE, this robotic eye disregards the significance of an exact EOM insertion point (IP) placement and sets the PAMs symmetrically about the globe's axis.

Another pneumatically-actuated 2 DOF robot eye has been constructed by Lenz et al. [35]. A web camera mounted on a 2 DOF gimbal system represents the globe, which is driven by 4 pneumatic artificial muscles (PAM) emulating the EOMs. This robot is used to evaluate the performance of a vision stabilizing control algorithm that is inspired by the cerebellar function in vestibulo-ocular reflex(VOR) of humans. Once again in addition to the drawbacks of the PAM actuators, this model also does not possess other significant features of the ocular plant including 3 dimensionality, accurate tendon IP and an accurate globe geometry.

A number of simulated biologically inspired eye models have also been developed for the purpose of scientific research [38, 65]. For instance Wei [65] has created a bio-mechanical simulator of the oculomotor plant, which includes features such as "subject-specific orbit models" and accurate EOM strain properties.

Mehmood et al. [38] have also designed a simulated model of the human eye to assess the importance of tendon insertion points for mechanically implementing listing's law. Nevertheless, as discussed previously, despite the evident advantages of a simulated model it is instructive to have a physical model.

1.4 Research Objectives

The objective of this research was to construct a biologically realistic robotic eye that can serve as a platform for understanding how the human oculomotor plant works. The motivation for this research is similar to that of the ACT hand developed by Matsuoka's group [59], which was developed to study and discover mechanism and control strategies used to provide robust, adaptable and skillful human hand movements. Clearly, it is not possible to precisely replicate a biological eye because of the many important facts about the relevant anatomy that are still being discovered and due to the limitations of the technology available to implement an eye model. Rather, I hope to capture some significant features of biological eyes that are not present in typical robot eyes. Specifically: (1) 3D eye movement, which includes not only "pan and tilt" movements but also torsional movements about the visual axis, (2) actuation using six pairs of muscles/actuators (hence redundant, with an approximately antagonistic arrangement of actuators), (3) specific insertions and origins of muscles on the globe of the eye, which are believed to have a significant influence on oculomotor behavior and (4) proper dimensionless scaling of the geometric and dynamic properties of the ocular system, including but not limited to the globe diameter, and inertia; a process necessary for

a proper performance comparison between the model and the biological system.

1.5 Organization of Thesis

This thesis is organized as follows. Chapter 2 provides some background on the biology of the oculomotor system. Chapter 3 discusses the mechanical and electromechanical design requirements. Based on the laid out requirements I then present the mechanical design of the robotic eye in Chapter 4. Appendix A provides more details about the mechanical design process. The kinematics of the resulting system and its control are discussed in Chapter 5. Given the controller developed in Chapter 5 the performance of the robotic eye is assessed by implementing on the robot a series of movements resembling the biological eye movements the results of which are given in Chapter 6. Finally Chapter 7 concludes the thesis and discusses the future work.

Chapter 2

Background

The ocular plant is a complicated structure, and a full understanding of it requires an in-depth knowledge of both the anatomy and the physiology of early visual and cerebral processing. However, when we consider the eye positioning machinery, the subject of this thesis, only certain biological features and behaviours are necessary to be included in the system. Consequently, the scope of this review is limited to anatomical information that is of importance to the kinematics of the eye, such as the extraocular muscles and the neural function required for replicating biologically inspired eye movements. And it excludes details of acquiring the image including image mapping and the role of the retina and iris in early visual processing. For a more extensive discussion of these topics please refer to *The neurology of eye movements* by Leigh, R.J textbook [34].

2.1 Anatomy

The eye sits within a pyramid-shaped bony structure called the orbit. It is held within the middle of this space by a layer of fibrous connective tissue called *Tenon's capsule*. The *Tenon's capsule* provides the cavity for the eye to move within the periorbital fat, which maintains the globe in an anterior position. Three pairs of muscles known as the extraocular muscles (EOM) insert into the globe, and it is the innervation of these muscles that generate the force required to rotate the globe in three dimensions. Figure 2.1 illustrates the six EOM; they are: medial rectus (MR), lateral rectus (LR), superior rectus (SR), inferior rectus (IR), superior oblique (SO), inferior oblique (IO). This 3D model was developed by Wei et al. [65] from MRI data.

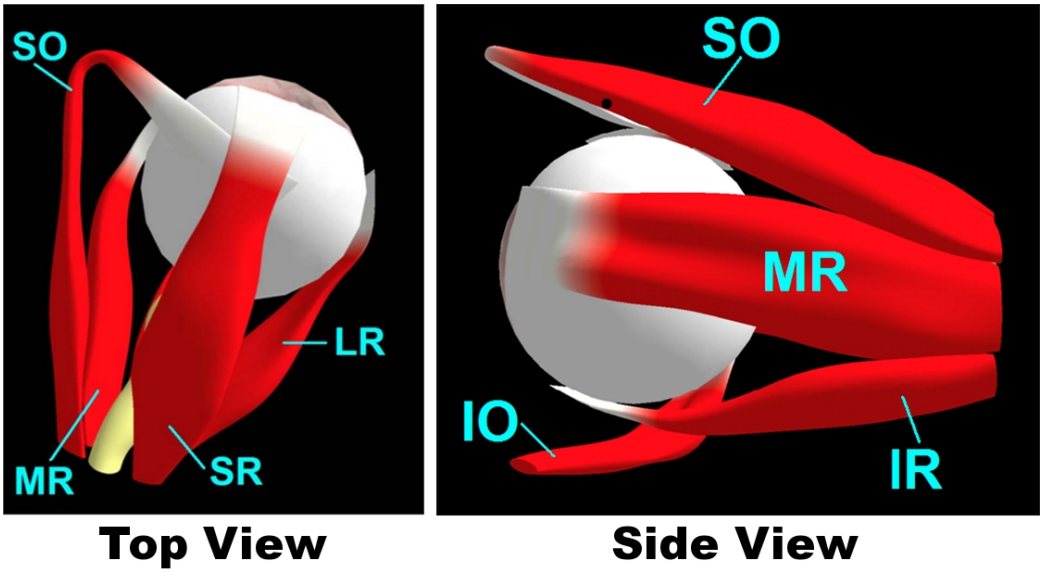

Figure 2.1: 3D model of the right eye, reconstructed from MRI [65]

The four recti muscles originate from the the annulus of zinn (AZ), a fibrous ring of tissue that encircles the optic nerve. The conical orbital walls point outward at approximately a 23° angle. Thus, in primary position the superior and inferior rectus lines of action are approximately at a 23° angle with respect to the anterioposterior axis of the globe [47]. The recti muscles have a fairly constant muscle length of about $37mm \pm 0.7$ while their tendon lengths vary between $3-7mm$ [61].

The SO is the longest EOM, with $30mm$ muscle length and $30mm$ tendon length. It also originates from the AZ but its path is redirected through the trochlea, a tissue pulley structure attached to the medial orbital wall, such that it is aligned with the ceiling of the orbital wall and makes an approximate 54° angle with the anterioposterior axis of the globe [51, 61]. Unlike all the other EOMs, the IO arises from the medial orbital wall, anterioinferior to the globe. This $37mm$ long muscle continues from its origin in a path backward, upward and laterally between the orbital walls and the IR, and it inserts onto the globe through a $1-2mm$ tendon. This results in an approximate 51° angle between the IO and globe's vertical plane [62].

The EOMs are activated by the three cranial nerves III, VI and IV. The oculomotor or third cranial nerve supplies the SR,IR, MR, and IO while the abducens or the sixth cranial nerve is responsible for activating the LR. Finally, the fourth cranial nerve, also known as the trochlear nerve, supplies the SO muscle.

Abduction[1] and adduction[2] of the eye is primarily achieved by contracting the LR and MR respectively. These pairs of opposing muscles are called antagonist pairs. According to *Sherrington's law of reciprocal innervation*, a muscle's stimulation is accompanied by inhibiting its antagonist [21]. As a result, abduction is achieved by contracting the LR and relaxing the MR. Given the binocular vision of humans, synchronized movements of both eyes are required for directing the gaze in a given direction. Consequently, the neural control of the EOM of one eye is partnered with the control of the other eye. These partnering EOMs in each eye are known as yoke muscles. For example, in a right gaze the LR of the right eye is the yoke muscle for the MR of the left eye and vice versa. The activations of these yoke muscles are described by *Hering's law of equal innervation*, which states that the muscles receive equal and simultaneous innervation, based on the position of the eye [23].

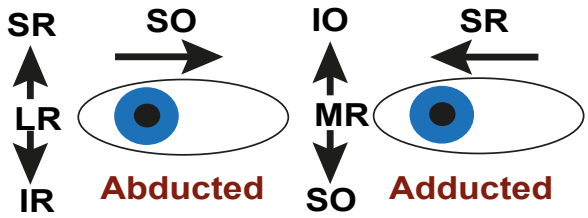

Figure 2.2: The arrows indicate the pulling direction of the EOMs for the abducted and adducted eye

The MR and LR muscles primarily act to abduct and adduct the eye regardless of the eye orientation. However, the action of the SR,IR, IO, SO varies depending

[1]Abduction is the movement of the cornea away from the midline of the eye.
[2]Adduction is the movement of the cornea towards the midline of the eye.

on whether the eye is abducted or adducted. An abduction of 23°, aligns the SR and IR with the axis of the eye, which makes them primarily elevators and depressors. In this orientation, the SO intorts the eye (rotates the globe medially while the IO extorts the eye (rotates the globe temporally). Conversely, in an adducted eye, elevations and depressions are achieved primarily by the IO and SO, while intorsion and extortions become the duty of the SR and IR, respectively. Figure 2.2 illustrates the function of EOMs for the abducted and adducted eye.

2.2 Eye Movement

As mentioned previously, eye movements are an essential part of acquiring visual information. We move our eyes to either shift our gaze to direct the fovea onto the object of interest or to stabilize the image on the retina. Saccades, smooth pursuits, and vergence movements are gaze shifting mechanisms, while vestibular-ocular and optokinetic reflexes are the movements responsible for gaze stabilization during head movement. In addition, although not immediately apparent, maintaining visual gaze (or visual fixation) requires activating the EOMs as well as micro-saccades, which are necessary for proper stimulation of the photo-sensitive cells. This review is focused on the two most frequent eye movements: saccades and smooth pursuits. These are also the two main movements that are to be implemented on the eye model presented in this thesis. For more information about eye movements see [33, 66].

2.2.1 Saccadic Eye Movement

Saccades are rapid and abrupt simultaneous movements of both eyes, which essentially change the point of fixation in a short period of time. Saccades are the basic mechanisms for a number of eye movements including fixation and rapid eye movements. However, the main purpose of saccadic eye movements is to place small visually interesting parts of a scene onto the fovea, where they can be sensed with the highest resolution. This is because like many other animals with fovea, the human brain builds a mental 3D model of the scene based on the small parts of a scene sensed through the fovea. Saccades are the fastest rotational movements in the human body, reaching angular speeds of 500 Deg/sec in humans and up to 1000 Deg/sec in monkeys. Due to the extremely high angular velocities, no visual processing can be performed and therefore saccadic movements are controlled without visual feedback. Initiation of a saccade can take up to 200ms and it lasts between 20ms - 200ms, depending on the amplitude[3] of the saccade [33, 52].

Saccade magnitudes could reach values as high as 90°. However, for magnitudes larger than 20° they are generally accompanied by a head movement. The angular velocity of the saccade is related to its amplitude. This relationship is linear for amplitudes of up to 60°, but as we approach the maximum possible eye velocity, this relationship becomes nonlinear and saturates. In fact, the proportionality of a saccade's peak velocity to its magnitude is called the *main sequence* [5]

[3]The amplitude of a saccade is described as the angular distance traveled by the eye during the saccade

and is what distinguishes saccades from other types of eye movement.

2.2.2 Smooth Pursuit Eye Movement

Smooth pursuit is the movement of our eyes as they track a moving target. Similar to saccades, the main goal of this movement is to keep the target close to the fovea. However, unlike saccades, pursuits are triggered by the movement of the target, and in fact in most cases subjects are not able to initiate a pursuit without a moving target. Consequently, the role of smooth pursuit movement is to match the eye velocity to that of the moving target. This velocity is normally relatively low (in the order of tens of degrees per second), which provides sufficient time for visual processing. This means that, unlike saccades, pursuits are controlled with constant visual feedback. However, despite this visual feedback, there are occasional large errors that are compensated for by *corrective saccades*. In fact, target velocities of larger than 30 Deg/sec are usually composed of alternating periods of pursuit and saccades.

Chapter 3

Design Requirements

This section gives an overview of the specified requirements for both the structural and the mechatronic design. These requirements were mainly selected to ensure that the final eye model would be an adequate testbed for studying the oculomotor system.

3.1 Structural Requirements

Our design decisions have primarily focused on creating an eye model that mimics the geometric and anatomic properties critical to the static and dynamic performance of the human eye. As discussed in the following paragraphs, such requirements are satisfied by a three dimensional, appropriately scaled model that represents the agonist/antagonist EOM accurately.

It is not trivial to extend controllers in 1D to 3D; as a result, a three dimensional model becomes crucial in understanding how human eye movements are

controlled. This is because, when rotations around a single axis are considered, angular velocity is simply the time derivative of the orientation, and artificial one dimensional oculomotor controllers rely on this fact. However, this does not hold in three dimensions since multidimensional rotations are non-commutative. Therefore, a significant part of unraveling the oculomotor controller is recognizing how this non-commutativity is dealt with. In fact,there is much debate over whether the neural controllers are accounting for this non-commutativity [25, 37] or are the orbital mechanics (orbital pulleys) compensating for this by making the ocular plant appear commutative to the neural controller [15, 16, 41, 48, 50]. Consequently, in addition to having three dimensions, the model must include, or at least have the potential of including, the orbital pulleys if it is to be used as a testbed for assessing the merits of the different sides of the debates.

As most movements in humans, ocular movements are accomplished by the pulling force of the agonist/antagonist muscle pairs. Therefore, an essential part of understanding the oculomotor controllers is recognizing the relationship between the direction of the torque produced by contracting the EOM and the resulting 3D orientation of the eye. Further [26] has proven analytically that it is incorrect to simplify muscle pairs by replacing them with "single bidirectional" muscles, as has been commonly done previously [17, 48, 50, 56]. Consequently, it is apparent that representing all 6 EOMs is a key feature that must be incorporated in the design of a geometrically accurate eye model. A full representation of the EOM entails the incorporation of:

1. Muscle actuation

2. Tendons (Force carriers between the globe and the actuation.)

3. Accurate tendon attachment locations

Biologically accurate tendon attachment locations on the globe are usually neglected in the modelling of the eye, mostly to simplify the kinematic analysis involved. Nevertheless, there is mathematical evidence that shows how the specific location of these attachments could in fact simplify the job of the neural controller [49]. Thus, to further examine such speculations, it is important to replicate this characteristic.

An essential part of creating a geometrically accurate model is replicating the human eye geometry. However, physical constraints including available part sizes and accessibility of the testbed create limitations on how feasible this duplication can be. Nevertheless, the model's size and inertia effects the required forces, natural frequencies and velocities. As a result it is crucial to have a procedure whereby all the essential properties are scaled in relation to the model's specified dimensions and inertia. Here, we have used the *Buckingham* π *theorem* to meet this requirement. By ensuring that key Π variables are equivalent in the real eye and our model, we can scale the model up at our convenience without losing any information.

The globe support structure is another important component of this design. A suitable structure must allow for the three dimensional movement of the globe within the same range as the biological eye. In addition, the design must allow room for a clear routing of the tendons and allow accessibility to various parts

of the model as it is to be used as a testbed. Actually, this part proved to be the most involved in terms of design work since simply reproducing the biological equivalent of connective tissues is not trivial. Section 2.1.4 includes explaining the detailed design of this structure, including the additional requirements that had to be taken into account.

It must be noted that a number of reasonable assumptions were made early on. Firstly, the eyeball is taken to be a perfect sphere, which is a very close approximation aside from the slight anterior bulging where the cornea is located. It is also assumed that the centre of rotation of the eye is fixed and located at the centre of the sphere. This is a minor assumption as, in actuality, the centre of the eye is only 1.3 mm posterior to this assumed location [19]. Furthermore, the centre of the real eye has non-zero velocity, however these velocities are very small and are generally ignored [19]. Finally, mechanical constraints such as material strength,weight, friction and sizing played a significant role in the final decisions made throughout the design process. Consequently, as the design process progressed, a number of other assumptions were made, which will be explained in context in the forthcoming chapter.

3.2 Mechatronic Requirements

Before discussing the established requirements for an appropriate controller, I would like to reiterate that the primary purpose of this thesis is to introduce an anatomically accurate eye model. Consequently, the main goal of implementing a control algorithm is to evaluate the performance of this robot eye. This means

the presented control algorithm is not inspired by existing theories about how the brain controls the oculomotor plant. Nonetheless, the desired performance of this controller was chosen to be comparable with eye behaviour during a saccadic eye movement. This was to ensure a reasonable equivalence between the performance of the eye model and the documented behaviour of human eyes. Saccades are

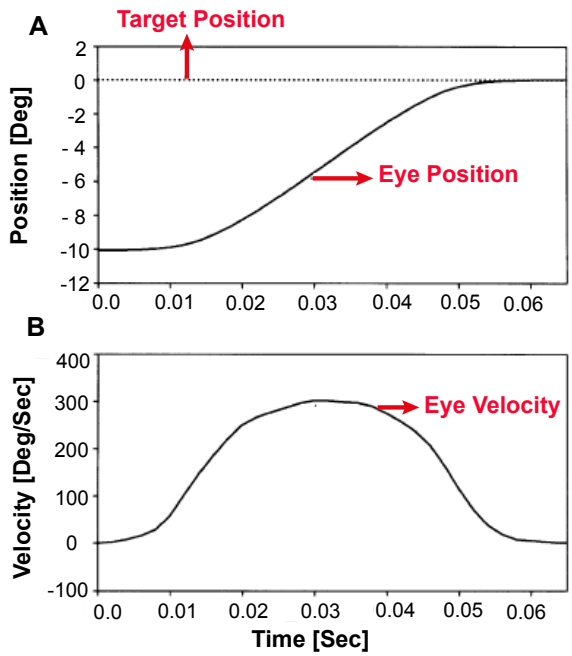

Figure 3.1: Position and velocity profile of a 10° saccade [31]

one of the most studied and well known movements of the human body. Over the years, scientists such as DA. Robinson and many others have characterized the

behaviour of saccadic eye movements [6, 20, 31, 33, 52]. Figure 3.1 illustrates the position and velocity profile of a 10° saccade. This saccade is completed in $40ms$ with the velocity reaching values as high as 300 Deg/sec. These values increase with increasing saccade magnitude, a relationship described by the term *main sequence of saccades* [5]. Furthermore, the steady state error of a saccade is on the orders of 10th of a degree and saccadic eye movements are characterized by their overdamped response[1] [33].Ultimately, these elements became the basis of the requirements set out for the control algorithm presented in this thesis. Specifically the controller must enforce:

1. An overdamped response

2. A steady state error of $<= 0.1^\circ$

[1]A response where there is no oscillation about the steady state value, as illustrated in Figure 3.1 A

Chapter 4

Structural Design

This chapter will present the guidelines used to design the tendon-driven eye model presented in this thesis. The chapter is organized based on the *Structure Requirements* outlined in Chapter 3. **Scaled Model Design** is discussed in Section 4.1. Section 4.2 will explain how **Musculotendons** are represented. Finally in Section 4.3, I will discuss the design and manufacturing process of the **Globe Support Structure**.

4.1 Scaled Model Design

The human eye is approximately 24 *mm* in diameter with an inertia[1] of approximately 4×10^{-7} Kgm^2 [69]. In addition, the orbital connective and fatty tissues that support the globe exert passive forces depending on the globe's position [53]. An important part of creating an anatomically accurate model is reproducing these

[1]This includes the inertia of the optic-nerve head, Tenon's capsule, and the EOMs.

geometric and dynamic properties. However, mechanical constraints make it difficult to reproduce these essential properties at such a small scale. This creates implications for how comparable our model will be to the biological eye. For instance, if the eye model does not share the same diameter, inertia, stiffness and damping properties, then the step and velocity responses of our model may be irrelevant to the biological responses. Consequently, it is crucial to devise a technique whereby common methods such as step and velocity responses can be used to assess the model when exact duplication of geometric and dynamic properties are not feasible.

One such method is the *Buckingham* Π *theorem*. Buckingham states that laws of physics can be expressed in a form independent of the units used [10, 12]. In other words, lets consider a problem that can be expressed by a set of dimensionally homogenous equations with n "dimensional variables", q_1,q_2, $\ldots$,q_n, as illustrated in Equation 4.1.

$$F(q_1, q_2, \ldots, q_n) = 0 \quad or \quad q_1 = f(q_2, \ldots, q_n) \tag{4.1}$$

Now if we let k denote the number of fundamental dimensions that are required to describe the n dimensional parameters (In the case of the ocular system these dimensions are, mass (M), length (L), time (T)) , then we can express Equation 4.1 by $j = n - k$ dimensionless and independent quantities known as Π groups, Π_1,Π_2, $\ldots$, Π_j, as seen in Equation 4.2. These "Π groups" are not unique; nevertheless they are independent of each other, in the sense that each one may vary

while the other stay constant.

$$G(\pi_1, \pi_2, \ldots, \pi_j) = 0 \quad or \quad \pi_1 = g(\pi_2, \ldots, \pi_j) \tag{4.2}$$

The Π theorem has 2 favourable attributes that could decrease the complexity of the problem in hand considerably:

1. When analytical equations are difficult or impossible to set up and solve for a given problem, the Pi theorem(more generally, dimensional analysis) can be used to infer the existing relations between some of the variables of the problem.

2. The size of a given problem is reduced by the number of fundamental parameters present in the problem.

Physical modelling, where a given system is scaled up or down, is an example of when Π analysis can be used to establish the relationship amongst the parameters of a given physical system. This relationship stays unchanged across all scales of the model.

Consequently, to create a physical model of the ocular plant, I used Π analysis to obtain a set of non-dimensional variables that must stay homogeneous across all sizes. This provides a platform for a valid conversion of physical quantities across the eye model and the biological eye. The following lists the steps that I took to arrive at the non-dimensional parameters for the ocular plant.

1. I determined the important variables governing the eyeball, while considering the physical significance of each chosen parameter. Most important in

choosing these governing quantities is their independence from one another, in other words modifying one parameter must not affect the others.

2. I then expressed each parameter in terms of the basic units of mass(M), length(L), and time(T).Table 4.1 gives a list of these parameters.

Table 4.1: The selected dimensional variables

Parameter	Unit	Fundamental Units	Description
τ	$[Nm]$	$[ML^2T^{-2}]$	Applied torques
B	$[Nm/rad/s]$	$[ML^2T^{-3}]$	Ocular damping constant
K	$[Nm/rad]$	$[ML^2T^{-2}]$	Ocular stiffness constant
I	$[Kgm^2]$	$[ML^2]$	Inertia
D	$[m]$	$[L]$	Globe diameter
ω	$[rad/s]$	$[T^{-1}]$	Globe Velocity
α	$[rad/s^2]$	$[T^{-2}]$	Globe acceleration [1ex]

3. Given the 7 quantities concerned in expressing the dynamic behavior of the eye and the 3 basic dimensions required to express them, I arrived at 7-3 = 4 non-dimensional quantities or π groups, which were formed as a combination of the 7 dimensional quantities. These π groups take the general form of:

$$\Pi = I^a D^b \tau^c B^d K^e \omega^f \alpha^g$$

Then the dimensional equivalent is expressed as:

$$\Pi = M^a L^{2a} L^b M^c L^{2c} T^{-2c} M^d L^{-2d} T^{-3d} M^e L^{2e} T^{-2e} T^{-f} T^{-2g}$$

To have Π be a non-dimensional number, the powers of all the separate

dimensions must add up to zero. Hence we arrive at the equations in 4.3.

$$\begin{aligned} a+c+d+e&=0 \\ 2a+b+2c+2d+2e&=0 \\ -2c-3d-2e-f-2g&=0 \end{aligned} \tag{4.3}$$

4. There are 7 unknowns and 3 equations therefore a solution may be found by arbitrary choosing values for 4 and solving the equations in 4.3 to find the other 3 unknowns. By selecting $c = 1$, $e = 0$, $f = 0$, and $g = 0$ we arrive at Π_τ:

$$\Pi_\tau = \frac{\tau^3}{IB^2}$$

Π_K is found by selecting $d = 0$,$e = 1$, $f = 0$, and $g = 0$:

$$\Pi_K = \frac{K}{\tau}$$

Setting $c = 0$, $d = 0$, $f = 1$, and $g = 0$ we find Π_ω as:

$$\Pi_\omega = \omega\sqrt{\frac{I}{K}}$$

Finally when we set $c = 0$, $d = 0$, $f = 0$, and $g = 1$ we find Π_α as:

$$\Pi_\alpha = \alpha\frac{I}{K}$$

Subsequently, the ocular plant may be expressed as a function of the resulting

Π variables:

$$G(\frac{\tau^3}{IB^2}, \frac{K}{\tau}, \omega\sqrt{\frac{I}{K}}, \omega\frac{I}{K}) = 0$$

This could be solved for any of the the Π groups, for instance solving it for Π_τ

$$\frac{\tau^3}{IB^2} = g(\frac{K}{\tau}, \omega\sqrt{\frac{I}{K}}, \omega\frac{I}{K}) \tag{4.4}$$

It is important to realize that the Π groups are not just numbers; rather, they represent important quantities that give insight to the physics of the model. For instance, let's consider the situation where we wish to find the required applied torque to move the eye model to a desired position, given data from the biological eye. In this case we can apply 4.4 to the eye model and the biological eye, with the primes representing the eye model.

$$\begin{aligned} \tfrac{\tau^3}{IB^2} &= g(\tfrac{K}{\tau}, \omega\sqrt{\tfrac{I}{K}}, \omega\tfrac{I}{K}) \\ \tfrac{\tau'^3}{I'B'^2} &= g(\tfrac{K'}{\tau'}, \omega'\sqrt{\tfrac{I'}{K'}}, \omega'\tfrac{I'}{K'}) \end{aligned} \tag{4.5}$$

Then, as the Pi theorem states, the arguments of function g are the same for both the model and the biological eye. Therefore, the value of the function would be the same in both cases and, as demonstrated in 4.6, the model's torque can be found in terms of the given biological torques:

$$\begin{aligned} \tfrac{\tau^3}{IB^2} &= \tfrac{\tau'^3}{I'B'^2} \\ \tau'^3 &= \tfrac{I'B'^2}{IB^2}\tau^3 \end{aligned} \tag{4.6}$$

An identical process would be carried out for finding other characteristics for the eye model, such as stiffness, given the known eye behaviours. Moreover, applying this method in reverse would be valuable in the validation process. Namely, by appropriately scaling model quantities such as the velocity profile, we can directly compare the performance of the model eye and the biological eye.

4.2 Musculotendon Representation

As discussed previously, creating an anatomically accurate model of the human eye also includes developing an actuation system that mimics the passive and active properties of the human EOM. Here I have chosen to use a tendon-driven structure where muscle active contractions, simulated by electromagnetic actuators, are transferred to the eye globe through cables that represent the ocular tendons. The details of these design decisions are explained in section A and B, respectively.

Furthermore, I have chosen to model and provide the passive properties of the EOMs in software rather than using a physical representation. This is because the perceived passive force of the ocular plant is associated with more than just the EOMs; it also includes other biological features such as connective orbital tissues and the optic nerve. A software representing the passive forces allows us to lump or separate these different parts, which becomes important when deciding on an appropriate ocular control algorithm. For instance, the authors of [49] have argued that to reach an accurate understanding of the ocular control algorithms used by the brain, it is essential to separate the muscular and orbital passive proper-

ties, whereas typically the ocular plant dynamics are lumped together in the most commonly used ocular models [48, 54, 58]. Consequently, this method of representation is preferred despite the complexity that it adds to the control algorithm.

A. Muscle Actuation

There have been a number of attempts to design an actuator that mimics the properties of human muscles. Amongst these are shape memory alloys [44], and pneumatic actuators [13] and specifically the most commonly used pneumatic actuator, the MacKibben actuator, or air muscle [14, 57]. All these actuators have been designed to mimic properties of skeletal muscles, which are known to be very different from the EOMs [46]. These actuators essentially have reproduced the quasi-static force-length relationship of the skeletal muscles and for the most part do not match the compliance characteristics of the real muscles. It is possible to construct a custom-made air muscle with properties of the EOMs, however a further shortcoming of pneumatic muscles is that their activation representation is not easily adjustable and thus it becomes difficult to capture the unique features of the EOMs. As a result, we have decided to use DC motors as our actuators. This allows incroporating the biological EOM and orbital properties in the control algorithm. In addition, unlike the fixed activation and force-displacement relationship produced by the pneumatic actuators, controlled DC motors allow for EOM activation representation that is adjustable for each muscle.

B. Tendon Representation

As is commonly assumed [17, 48, 50, 54, 56] , we have chosen to model the tendons as thin cables rather than as bands, which would more accurately model the physical shape of real EOM [26]. This is a reasonable assumption since the cable's width would only affect the area over which existing tendon forces are applied and would not effect the force balance on the globe. Furthermore, regardless of this assumption, the cables provide a simple yet appropriate replacement for the biological tendons, since just like the tendons they can only exert a pulling force. This is an important resemblance, which in theory provides a set of control challenges for the tendon- driven eye model that are similar to those that our brain must overcome.

I considered a number of different cables before deciding on a material that met the preceding specifications. Most importantly the cable must be lightweight with very high strength, and should be stiff relative to the compliance that is to be implemented in the controller. High stiffness and low weight would allow us to ignore the dynamic properties of the cables, thus making them ideal force carriers between the motors and the globe. This is also enables us to replicate the existing stiffness in the biological tendons purely in software without being concerned with uncertain material properties. Moreover, the cables must also have a smooth finish and a low coefficient of friction in order to minimize the friction with contacting surfaces.

Low stretch ($< 0.04\%\ inch/ft$ for 20 million cycles), nylon coated, stainless steel cables were the initial selection and they were attached to small screws

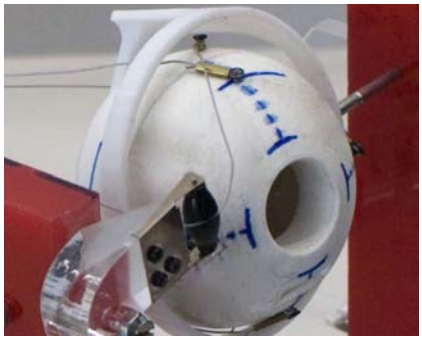

Figure 4.1: Tendon attachment with steel cables

threaded through the thickness of the globe, as shown in Figure 4.1. Furthermore, the presence of the nylon coating creates a smooth, low friction sliding contact between the cables and the globe. However, these steel cables have a large bending stiffness; namely they can not easily bend around sharp corners, which makes the routing and fastening of the cables rather difficult.

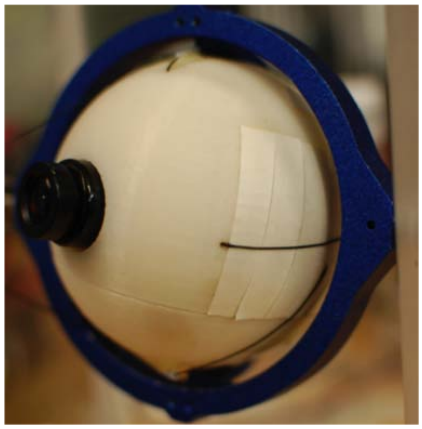

Figure 4.2: Tendon attachment with dyneema cables

For this reason, the steel cables were replaced with dyneema cables, a High

Modulus Polyethylene(HMPE) fibre. With a tensile strength of 3200 MPa, dyneema offers an extremely high strength to weight ratio. Dyneema also offers low elongation (E-modulus of 110 *GPa*, which is about 4 orders of magnitude larger than the 70 *kPa* [64] E-modulus of EOM tendons). This allows us to ignore the elastic and dynamic properties of the dyneema cables and view them as an ideal force transporters, which has great implications on simplifying the calculations required to find the actual torque transferred from the motors to the globe. Furthermore, compared to the steel cables the dyneema cables are small in diameter (0.8mm vs. 0.3mm) which makes it easier to handle them. They also benefit from very small bending stiffness, thus considerably simplifying the fastening and routing of the cables. Figure 4.2 illustrates the cable-globe attachments with the dyneema cables; here the cable is simply run through small holes in the globe and is secured in place by knotting it at the other end. This process greatly simplified the assembly process and it also reduced interference between fasteners of the cable and various parts of the model.

As mentioned in Chapter 3, it has been shown that biologically accurate tendon insertion locations could have great implications on how the brain controls eye movements [49], and thus it is important to include this feature in the design of our eye robot. Therefore, since the eye robot presented here is 2.5[2] times larger than the biological eye, all the biological attachment data from literature [60] must also be scaled by this factor.

[2] The eye robot has a 60*mm* diameter and the biological eye has a diameter of 24*mm*. This dimension for the model was limited by the size of the available camera.

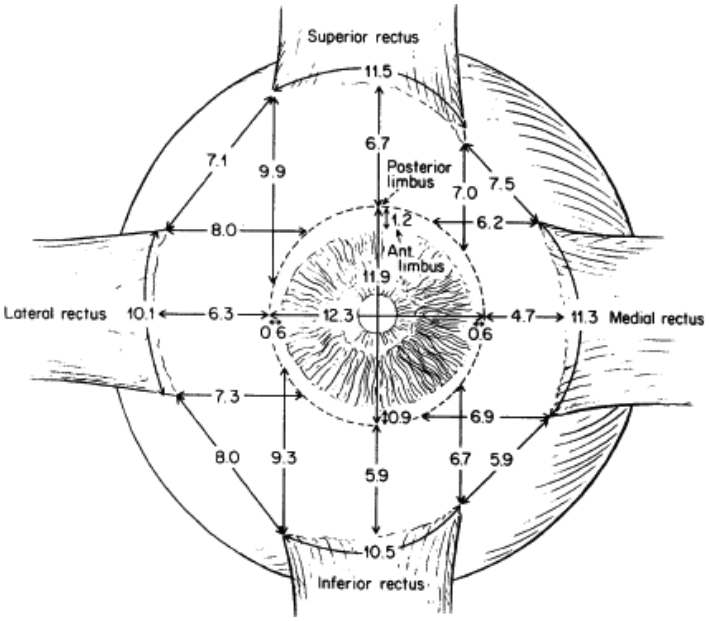

Figure 4.3: Rectus lines of insertion, [60]

EOM-globe attachments span a curved line, as shown in Figure 4.3. However, to simplify the modelling and analyzing process we have chosen to approximate this curve as a single point called the insertion point (IP), which is illustrated in Figures 4.1 and 4.2. This is a common assumption made by many researchers working on building an eye model [8, 49, 63] and no concerns have been reported about the potential implications of this assumption on how the oculomotor system is controlled. The IPs are taken to be at the mid point of the insertion curve, and it is the location of these selected points that are then scaled by the diameter ratio of the eye model to the human eye. Table 4.2 shows biological IPs, taken from the literature [49], and the corresponding scaled versions used in the model.

In addition to an accurate representation of the IP, routing of the tendons is

Table 4.2: The biological and the scaled insertion points *(*The coordinate is taken to be at the centre of the eye globe)

Extraocular muscle	Biological IP [mm]	Scaled IP[mm]
MR	[8.4, -9.2, 0]	[20.2, -22, 0]
LR	[6.7, 10.5, 0]	[16.2, 25, 0]
SR	[7.3, 0, 10]	[17.6, 0, 24.1]
IR	[7.7, 0, -9.8]	[18.4, 0, -23.5]
SO	[-4.5, 3, 11.2]	[-10.8, 7.1, 26.9]
IO	[-7.9, 9.6, 0]	[-19, 23, 0]

another key factor in reproducing the lines of action of the EOMs. To achieve this, the anchoring points, sometimes called pulleys, of each tendon were placed to force the cable to follow the same geometry as the EOM. This geometry was specified based on the anterioposterior axis of the globe and the angle that each EOM makes with it. These angles are listed in Table 4.3.

Table 4.3: Angles between the anterioposterior axis of the globe and the EOMs [60]

Extraocular muscle	Angle [deg]
SR	23
IR	23
SO	54
IO	51

Two types of anchoring were used, one for the recti muscles and one for the obliques. In the biological ocular plant, the four recti muscles and the superior oblique muscle originate from a common conical structure, called the AZ. In the eye robot this structure is reproduced using a low friction teflon cube, Figure 4.4. The teflon block has a small circular opening for each converging tendon to pass

through. There is a minor modification in our model, however: only the four recti tendons are routed through the modelled AZ structure. This decision was made in order to develop the most efficient and convenient motor arrangement, with the four recti motors located behind the globe and the oblique motors positioned to the right of the eye model.

For the obliques, once again attention was directed towards reproducing the tendon's precise lines of action, rather than exactly replicating the biological anchoring location. In this case the tendons were routed through very low friction plastic tubes glued into hooks as seen in Figure 4.4. This provided a low friction solution which was easy to incorporate into the design. Figure 4.4 also illustrates the motor mounting arrangements as well as the motor-cable attachment mechanism. Small aluminum static pulleys (OD=15m) were screwed to the motor shafts with setscrews and used to attach the cables to the the motors; the cables were then passed through openings in the pulleys and were knotted to keep them in place.

4.3 Globe Support Structure

The biological eyeball is suspended inside the conical walls of the orbit in an elegant manner. It is supported and protected by a layer of fibrous connective tissue called "Tenon's Capsule". The Tenon's Capsule provides a cavity for the eye to move within the periorbital fat which maintains the globe in an anterior position. Furthermore, there are ligaments connecting the EOM to the orbital walls and it is the action of these ligaments that is responsible for the smooth and dampened eye movements.

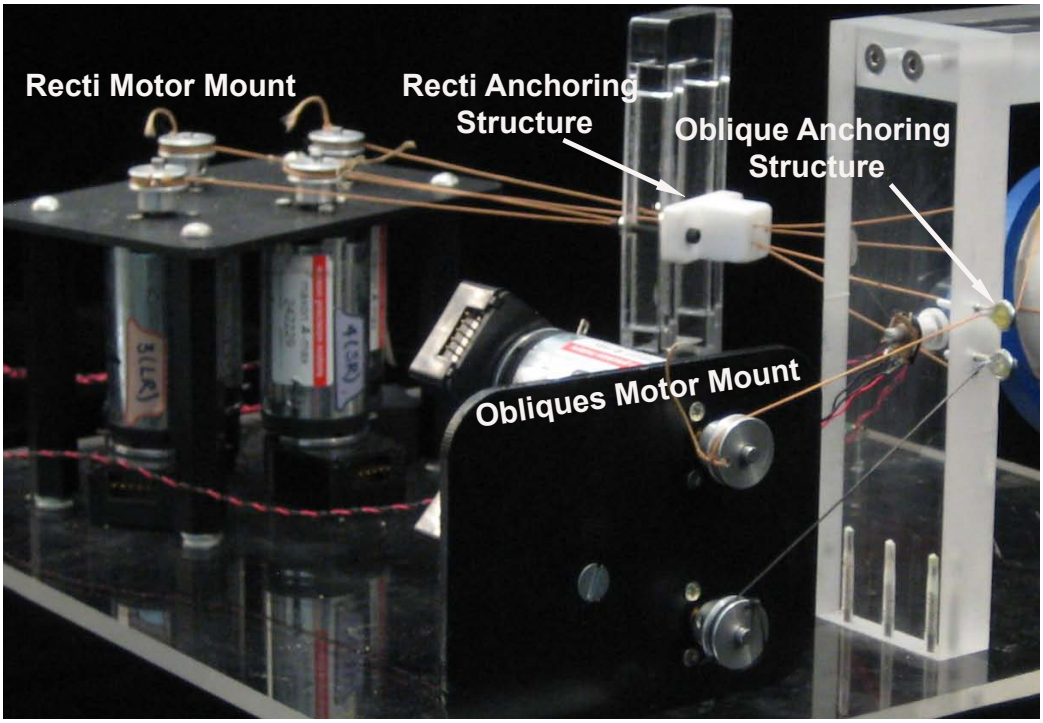

Figure 4.4: Motor mountings and cable routings

However, while it is important to capture characteristics of this orbital support, exactly replicating all of its features is not necessary to achieve a similar functionality. For instance directly representing all the features such as compliance of the globe, periorbital fat, and lubrication inside the orbit is not critical. Rather it is important to reproduce the purpose of these elements. Consequently, the modelled support mechanism must keep the globe in an anterior position, provide a smooth and interference free path for the cables, and also allow for the 3D rotation of the globe. Moreover, as mentioned in Section 4.2 the elastic and damping forces of the connecting tendons will be accounted for in software.

To satisfy these requirements, I have custom designed a globe support structure that provides a practical and functional solution for the problem of supporting a spherical globe given the mechanical and material constraints. The corresponding design decisions were greatly influenced by the need for a flexible and open structure. This is essential for easy access to all parts of the model, which would facilitate operation and future modifications. The following design criteria were used throughout the various stages of the design process:

1. Provide a low friction mechanism that allows for the 3 rotational DOF of the globe, with the centre of rotation fixed at the centre of the globe

2. Ensure clearance of the cables throughout the entire range of operation

3. Present an optimal location for the camera and its connecting cables

4.3.1 Considered Solutions

Before deciding on the final design of the globe support structure, a number of methods were considered; models of some of these were built and tested in order to identify the design limitations. The initial concept was based on supporting the globe on ball-terminated screws[43], as illustrated in Figure 4.5. This was a simple design in terms of construction; however, the task of optimally locating the screws to avoid interference with the cables and their IPs proved to be complex. In addition the ball-terminated screws increased the dynamic friction of the system. I then considered supporting the globe using elastic stalks connected to the ground, Figure 4.6. However this design was also rejected since the elastic stalks

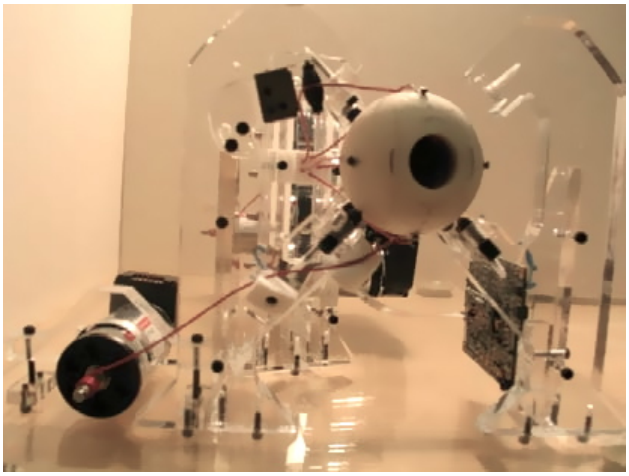

Figure 4.5: Globe support structure design based on the ball terminated set screw

would not provide a purely rotational support and would allow the globe to translate. Furthermore, similar to the screw supports preventing interference with the cables requires optimally locating the elastic stalk attachment to the globe which is challenging to find. I finally decided on a gimbal support structure, which is what the final support structure is based on. The detailed design of these solutions are provided in Appendix A.

4.3.2 The Gimbal Globe Support Structure

It was apparent from early on that an off-the-shelf gimbal will not be sufficient to meet the specific characteristics required from a globe support structure. Consequently, gimbal support structure was custom designed to include the following desired features:

1. Have a single attachment point between the gimbal and the globe, to ensure

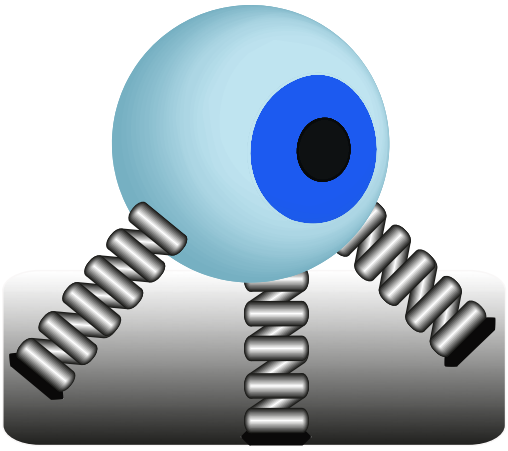

Figure 4.6: Concept of the elastic stalk support

clear routing of the cables.

2. Present an optimal location for the camera and its connecting cable.

3. Incorporate angle sensors for the 3 DOF.

4. Have yaw[3], the most frequent eye movement, as the inner most gimbal rotation to minimize the device's moment of inertia (MI) in this direction.

Ideally, the MI would be equal around all axes of the model. However, in practice this is difficult to achieve with a gimbal system since the globe's MI around all of the gimbal axes is increased by that of the moving gimbal elements except for the inner most rotation where only the globe is in motion. This results in 3 different MIs for the globe depending on which direction the globe is moving. Therefore, it is extremely important to not only reduce the individual added MIs due to the

[3]See Section 4.3.3 for definition

gimbal parts, but to also minimize the difference between them. The two factors that determine MI are the mass of the part and the moment arm[4]. Consequently, the structural strength of the gimbal system needs to be optimized to minimize the amount of mass needed in each stage.

With these specifications in mind, the general shape of the gimbal was decided based on an iterative design process. Various structural designs were prototyped, examined and adjusted in order to arrive at a suitable final design. In the following section, I will explain the detailed design of the final eye robot. For the design details of the earlier versions of this gimbal system please refer to Appendix A.

4.3.3 The Eye Robot - Structural Design

Figure 4.7 illustrates the final design of the eye robot with the gimbal support structure. Considering the right hand coordinate system illustrated in this figure, yaw is rotation about the **Z** axis, pitch is rotation about the **Y** axis, and finally roll defines rotations about the **X** axis.

An important aspect of gimbal design is the sequence of rotations it implements. As discussed previously, since a gimbal forms a serial kinematic chain, the proximal axes of rotations have larger inertia than the distal ones. The standard Helmholtz and Fick gimbals used in the eye movement literature [22] have torsion ("roll") as the final axis, but the most common eye movement is a horizontal rotation ("yaw"). Therefore our gimbal implements pitch, followed by roll, with yaw as the final rotation. The key to achieving this sequence lies in the unique de-

[4]Moment arm is defined as the radius of gyration of the gimbal part

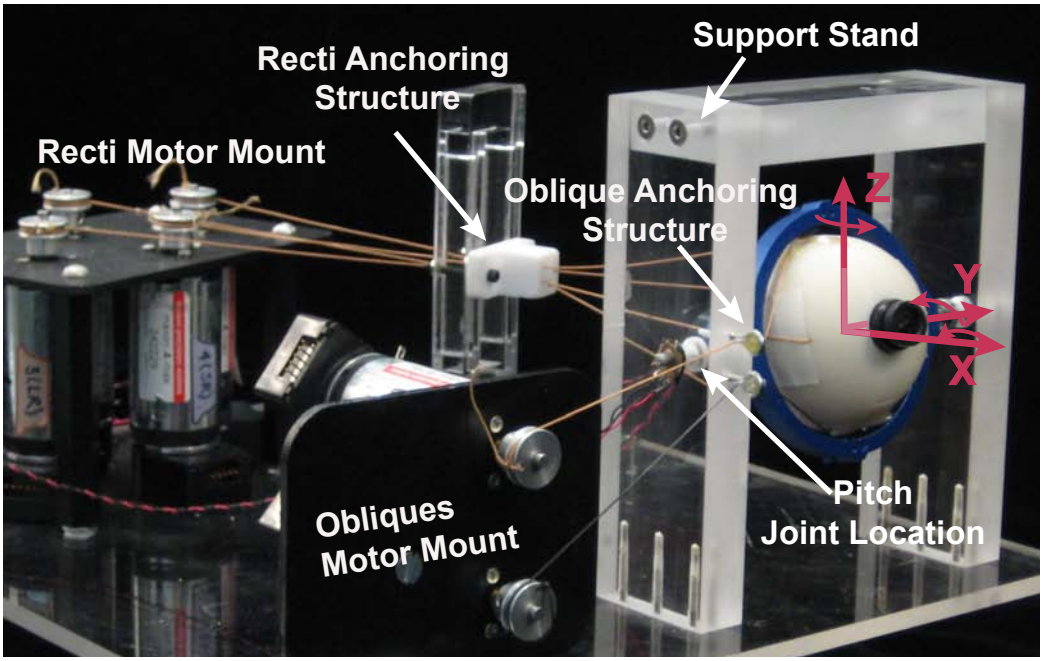

Figure 4.7: The eye robot, final design of the gimbal globe support structure

sign and placement of the gimbal elements, which are discussed in the following paragraphs.

Figure 4.8 illustrates the inner gimbal element labeled C-bracket. This element along with the globe's interior were custom-designed to bear the shaft and the rotational joints of the yaw and roll movements. The C-bracket and the globe, respectively, accommodate the rotational joints and shafts required for the globe's yaw rotation. The globe is divided into two sections, the top hemisphere and the bottom hemisphere. Each hemisphere has 8*mm* long bosses on the bottom of its inner surface. These bosses are drilled down 10*mm* into the thickness of the globe to hold the stainless steel precision shafts that support the yaw rotation,

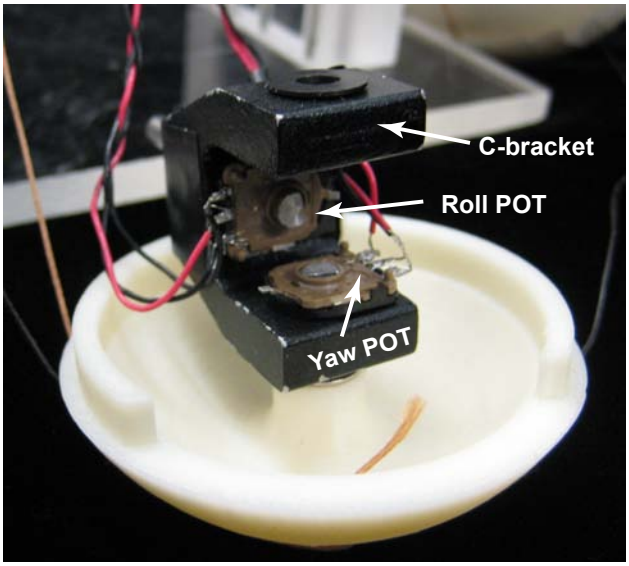

Figure 4.8: C-bracket, the inner structure of the eye robot

Figure 4.9b & 4.9c.

The corresponding rotational joints for these shafts are the 2 openings that are drilled across the length of the C-bracket, as labelled in Figure 4.9c. Given this arrangement, during yaw rotations the globe is the only element in motion. Thus, the globe must include a posterior slot, labeled "trace slot" in Figure 4.9a, to accommodate the roll shaft that is attached to the stationary C-bracket inside the globe.

The roll rotations of the eye robot are supported by a single joint, located at the centre of the C-bracket, Figure 4.9c. The globe and its content cantilever off of the stainless steel precision shaft responsible for this rotation and this shaft is fastened to the back-ring (Figure 4.9e) and rotates with respect to the rest of the

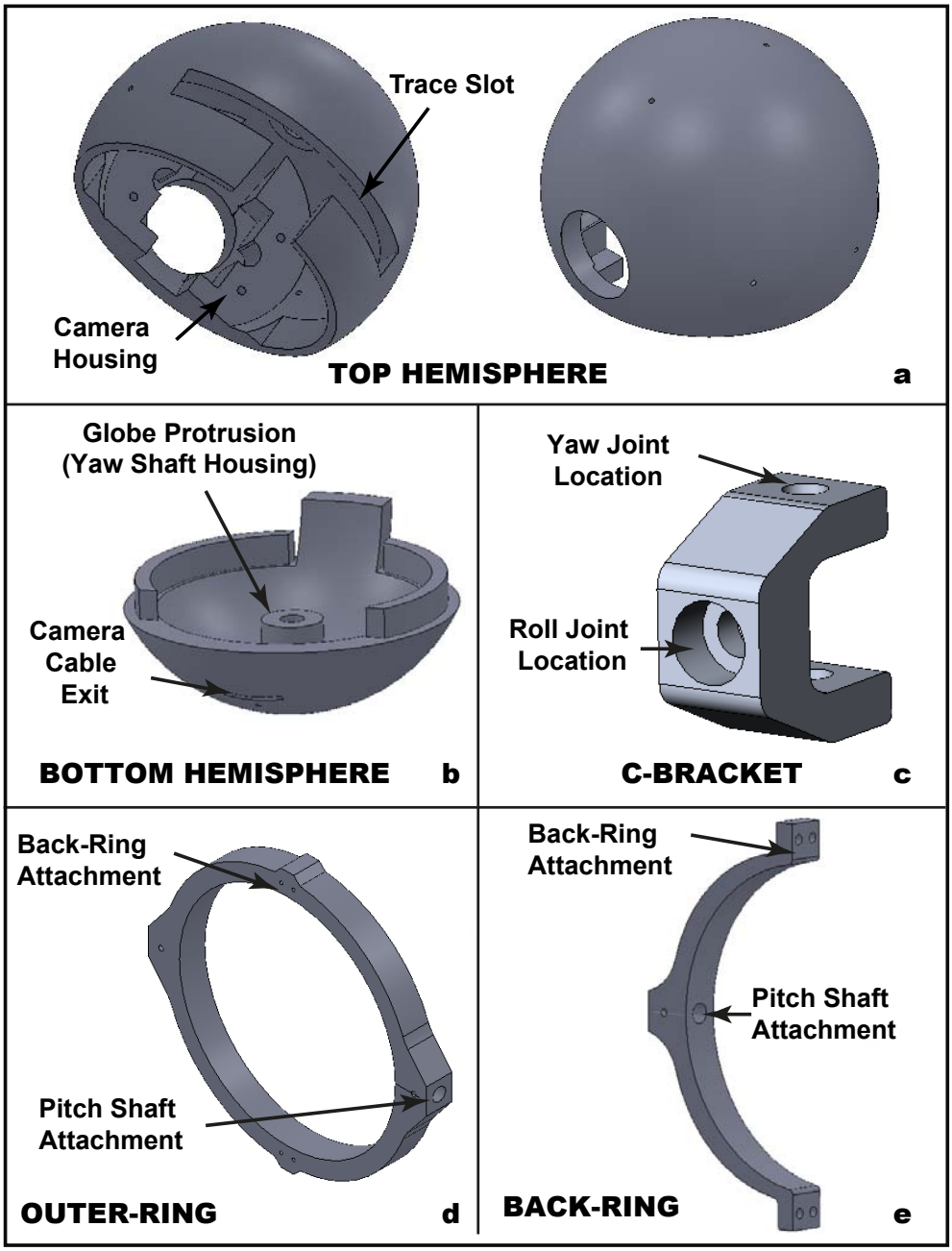

Figure 4.9: Solid model of the eye robot parts

gimbal. Considering such attachments, it is apparent that during intorsion[5] and extorsion[6] the globe's MI is increased by the MI of the C-bracket, which moves with the globe.

Finally, pitch rotations are supported by the two joints inside the support stands, labelled in Figure 4.7 and the two shafts fastened to either sides of the outer-ring along its centre line, Figure 4.9d. This makes pitch the outermost rotation, which means that during elevation and depression of the globe all the gimbal elements (C-bracket, back-ring, and outer-ring) are also in motion, thus increasing the globe's MI. To reduce the inevitable increase that the gimbal imposes on the globe's MI during pitch and roll rotations, I have decreased the moment arm of each element as much as possible given the geometrical and structural constraints. Specifically, by placing the C-bracket inside the globe and making its height as short as possible, the element is brought close to the centre of rotation of the globe, which significantly reduces its effective MI. Furthermore, I have carefully chosen the diameter of the outer-ring and back-ring to minimize the gap between the ring and the surface of the globe, without compromising a clear routing for the cables.

[5]Rotation towards the centre of the body

[6]Rotation away from the centre of the body.

4.3.4 The Eye Robot - Manufacturing

The Eye Robot - Sizing and Material Selection

The majority of the dimensions in the eye robot were constrained by the measurements of a suitable camera. The camera is to be used in the implementation of a biologically inspired controller and thus its incorporation in the design is of great importance. The selection process for the camera was mainly driven by its size and its capability to provide live image information with a minimum speed of 30 frames per second. Based on these requirements the Point Grey, Dragonfly2 camera was selected. Dragonfly2 is a remote head camera, meaning that the the camera can be detached from its processing board thus, making it relatively compact, 20 $mm \times 30$ $mm \times 23$ mm. Furthermore, this camera has a speed of 60 frames per second, which is sufficiently above the required speed of 30 frames per second.

Figure 4.10 illustrates an exploded view of the globe's inner structures. The C-bracket holds the roll and yaw joints and their subsequent angle sensors. Thus, I began the sizing process by first selecting the dimensions of the C-bracket based on the smallest available angle sensor, a 11 $mm \times 11$ $mm \times 2.2$ mm potentiometer labelled in Figure 4.8. To get an accurate measurement from the potentiometers, they must be fixed to the C-bracket. Therefore, lengths a and c, as labelled in Figure 4.11a, must be at least as long as the $11mm$ width of the potentiometer. Given the values chosen for the lengths of a and c, I calculated the smallest possible inner diameter that would leave sufficient space for the camera inside the

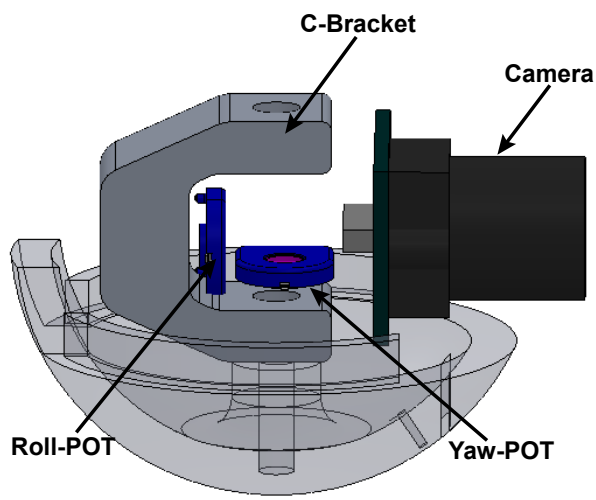

Figure 4.10: Exploded view of the globe's inner structures

globe without any interference between it and the C-bracket, as illustrated in Figure 4.10. Thus, by choosing a $2mm$ wall thickness, the globe's final dimensions are $ID = 56\ mm$ and $OD = 60\ mm$. This 2 mm globe wall thickness does not provide sufficient support for the 17 mm yaw shafts; this is the reason for adding the two 6 mm bosses inside the globe, labelled in Figure 4.9b. The thickness of the back wall(t_b) and top and bottom walls (t_t) of the C-bracket, labelled in Figure 4.11a, were determined last. t_b was selected to accommodate the two 4 mm thick ball bearings required to support the roll joint, while t_t was restricted by the 6 mm high polymer bushings used to reduce friction in the yaw joints. It should be noted that the size of these bearings were limited by the allowable 4 mm diameter hollow potentiometer shaft.

The back-ring and the outer-ring inner radii were chosen to bring them as close as possible to the circumference of the globe thus, reducing their effective

MI. Furthermore, the 8 *mm* thickness of these elements is a direct consequence of having to accommodate the 4 *mm* roll and yaw shafts, which were imposed by the hollow shaft potentiometers.

I selected the outer radii of the outer-ring and back-ring to reduce their mass to a minimum without jeopardizing their structural strength. As a result, I began by choosing a material that would provide the optimum mass-strength ratio considering the manufacturing methods available to me. Given the somewhat complex shape of these elements I deduced that a 2D or 3D prototyping process would be the most suitable option. Therefore, I chose 3D rapid prototyping to fabricate the earlier version of the eye robot out of polycarbonate, the strongest materials available for this method (Tensile strength, 68 *MPa*). However, when this earlier version of the eye robot was tested under maximal loading it was apparent that the 4.8% tensile elongation of polycarbonate is too large to meet the maximum desired deformation of 0.1 *mm*. Consequently, the high stiffness and strength of aluminium was utilized to achieve the deformation requirements and keep the mass relatively low. This material choice narrowed the manufacturing process to "Water Jet Cutting", a 2D prototyping method. Thus the final dimensions of the outer-ring and back-ring were calculated considering the maximum applied forces as well as the precision capabilities of the Water Jet Cutter being used. The force analysis and dimensional optimization of these elements were carried out using Cosmos, the analysis simulator in SolidWorks.

The optimized thicknesses of the back-ring and the outer-ring achieved by the process that was just explained are not suitable for supporting the 4 *mm* diameter

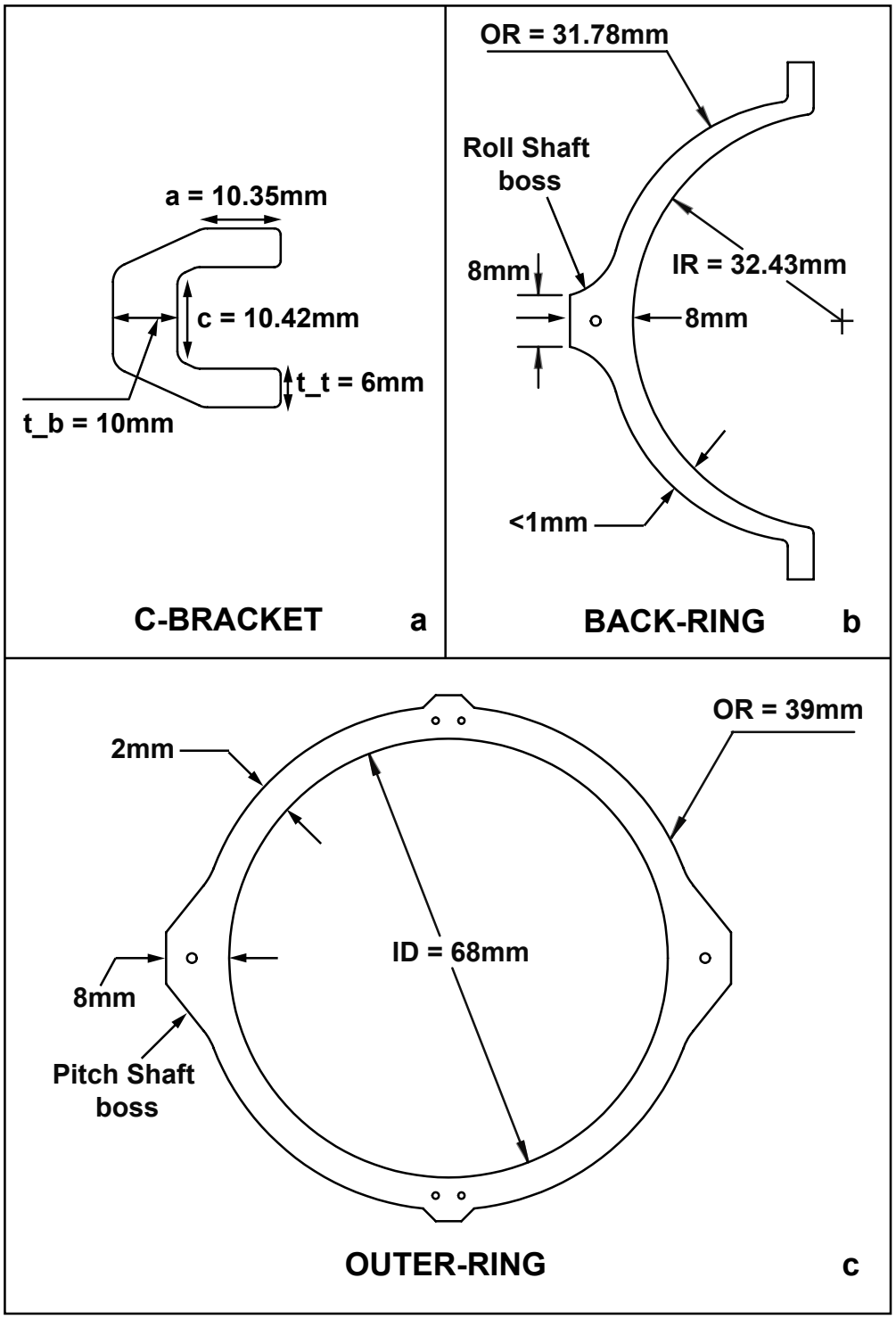

Figure 4.11: Dimensioning of the eye robot part

shafts of roll and pitch rotations and would therefore induce undesirable stresses in the outer gimbal elements. This is because the optimization process used disregarded the requirement that the shafts for the pitch and roll rotations must respectively be supported by the 2 *mm* thick outer-ring (Figure 4.11c) and < 1 *mm* thick back-ring (Figure 4.11b). In addition, the globe and everything inside of it cantilevers off of the roll shaft held by the radial thickness of the back-ring (Figure 4.11b) and subsequently the entire weight of the gimbal structure is supported by the pitch shafts held by the radial thickness of the outer-ring (Figure 4.11c). Consequently, the outer-ring and back-ring were protruded 8 *mm* (respectively labelled as pitch and roll shaft boss in Figure 4.11b and Figure 4.11c) at their shaft connection areas. This provided the required support for the load bearing shafts without adding excessive material and weight.

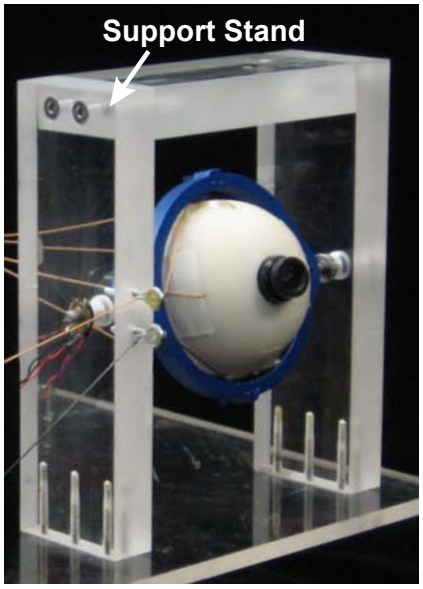

Figure 4.12: Acrylic support stand

An acrylic structure, labelled "support stand" in Figure 4.12, acts as the support that holds the outer gimbal element as well as the anchoring mechanisms of the oblique muscles. The 48 *mm* depth of this structure extends back to the furthest point of the back-ring, a design decision intentionally made to facilitate future modifications for including the orbital pulleys in the design. The orbital pulleys attach the globe to the inner walls of the socket and as discussed in Section 3.1, their function is a controversial subject amongst the experts and requires further investigation. Thus it is important that the design would include the potential of adding the pulleys. Much like the trochlea of the SO, the orbital pulleys are thought to act as flexible anterior anchoring points for the Recti muscles [27, 39]. The conceptual design for mechanically representing these connective elements is to fasten panels with rows of holes (labelled *"pulley routing plate"* in Figure 4.13) to the back walls of the extended acrylic support thus reproducing a posterior anchoring for the cables as they are routed through the appropriate holes inside the panels. A sketch of this conceptual design is illustrated in Figure 4.13.

Manufacturing Process

Rapid prototyping methods provide a fast and relatively cheap alternative for manufacturing prototypes, which greatly facilitates iterative testings of various designs. Consequently, 2D water jet cutting and 3D fused deposition modelling were utilized for fabricating the eye robot, and, as discussed briefly in the previous section, the most suitable processes were chosen based on the materials selected.

As suggested by its name, a water jet cutter uses high velocity and pressure jet

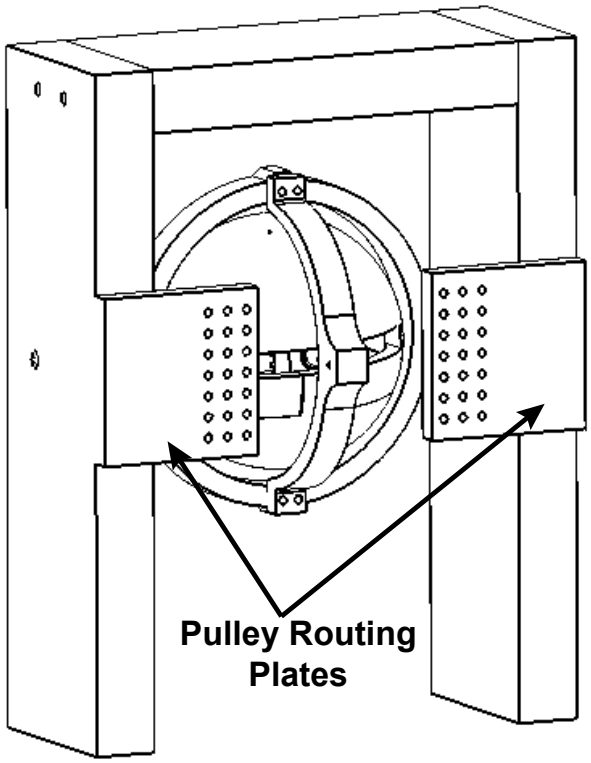

Figure 4.13: Conceptual design for incorporating the ocular muscle pulleys in the current eye robot

of water to cut through metals and other materials such as granite. Here, I utilized the 2D *"Abrasive water-jet cutting machine MAXIEM 1515"* available at UBC's mechanical machine shop to fabricate the aluminum and acrylic pieces of the eye robot. This cutter is connected to a 20hp direct drive pump and has a position accuracy of ± 0.005" and a Kerf of 0.035"(± 0.01") for $1/8$" mild steel[7]. Using a water jet cutter provides a quick and efficient prototyping method, capable of cutting intricate shapes, directly from computerized engineering drawings, into the

[7]Specifications are provided by the MECH Machine Shop website

material of choice. Furthermore, the pressurized water jet used to cut through the material also acts as a cooling agent thus, preserving the material's intrinsic properties during the cutting process. This feature is especially beneficial when the material involved is easily deformable by heat, such as various types of plastics.

However, when 3D shapes such as the globe of the eye robot are required, water jet cutting becomes inadequate. As a result, I used the rapid prototyping services of the company "RED EYE" to fabricate the globe. RED EYE uses *"Fused Deposition Modelling(FDM)"*, an additive manufacturing method that transforms 3D CAD models into physical prototypes. The CAD file is sliced and is used to define a tool path for the heated extrusion head. The extrusion head then deposits $0.125mm$ layers of liquified thermoplastics, which hardens immediately after release, to build the part one later at a time, from bottom top. As a result, materials practical for this process are limited by their heat resistance properties and include various types of plastics. I chose to use ABS M30 for its high impact, tensile and flexural strength[8]. Moreover, ABS M30 posses a strong layer bonding, which results in high quality, durable and strong parts, capable of including detailed features. In essence FDM is an excellent method for producing durable prototypes with great dimensional accuracy[9].

[8]Tensile Strength = $36Mpa$, Tensile Elongation = 4%, Flexural Stress = $61MPa$

[9]Depending on the size of the part, achievable accuracies vary between $\pm 0.127mm$ or $\pm 0.0015mm/mm$, the greater of the two.

Joint Details

Each joint must provide a low friction and rigid support for the gimbal elements, while applying sufficient constraints to eliminate joint play by restraining its movement to a specific rotational direction. Thus, a suitable design of the gimbal joints is essential for obtaining a high quality performance from the eye robot.

The roll joint in particular requires an intricate design because it is a single cantilevered joint that must support the entire weight of the globe and its content, while firmly holding them in place under the applied tendon loads. I utilized radial ball bearings to satisfy the load bearing requirements of this joint. The bearing balls, which are held in place by the rotating inner race and the fixed outer race, greatly reduce the rotational friction while transmitting the radial loads attributed to the cantilevering masses. To ensure that the bearings provide sufficient support I have chosen to use two bearings housed in the $10mm$ diameter counter bore hole at the centre point of the C-bracket's back wall, labelled in Figure 4.14. Subsequently, one end of the roll shaft fixes to and rotates with the inner-race of the bearings, while the other end attaches to the back-ring using a setscrew, Figure 4.14. To increase the contact area between the shaft and the setscrew and thus, ensuring a rigid attachment, I have cut a D profile on the shaft and used a flat end setscrew. Next, I examined the loads on the roll joint in order to apply the appropriate joint constraints. Pulling forces on the globe, exerted by the activated cables, are transferred to the C-bracket, the resulting force path of these loads are illustrated in Figure 4.14. To prevent the C-bracket from moving under these axial loads, a force path must be provided to transfer the loads to the back-ring (This

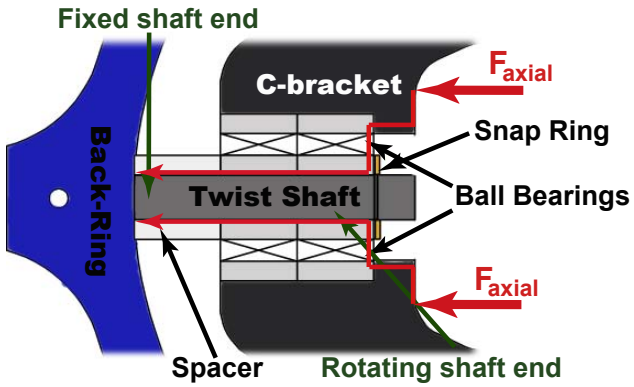

Figure 4.14: Cross section of the roll joint

path is illustrated in Figure 4.14). Thus, I have used a stainless steel spacer to provide a medium for this force transfer. Moreover, placing a snap ring (labelled in Figure 4.14) against the inner race of the front bearing provides the necessary forward joint constraint to prevent unintentional disassembly.

The entire gimbal system rests on the two pitch joints, Figure 4.15. Thus, similar to the roll joint, these joints must sustain a large radial load while allowing a low frictional rotation. Consequently, again I used two radial ball bearings to achieve these goals and housed them inside a 10*mm* diameter counter-bore hole on the side walls of the supporting stands. Same as the roll shaft, each pitch shaft fits to and rotates with the inner race of the bearings on one end and attaches to holes inside the outer-ring using a setscrew. Once again, I utilized a D profile on the shaft and a flat-ended setscrew to produce a rigid attachment. Considering the relatively low sideway forces, horizontal slack is not of much concern. Nonethe-

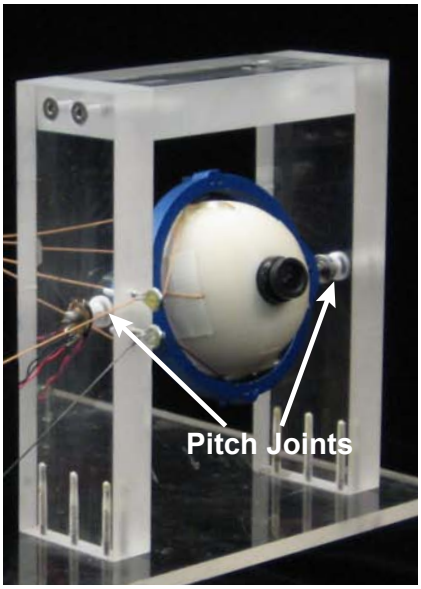

Figure 4.15: Pitch joints

less, to ensure a strong bond between the bearing and its shaft, I glued the outer surface of the yaw shaft to the bearing's inner race.

Because of their placement, yaw joints do not sustain much of the weight of the assembly and thus, these joints are the simplest in design. Therefore, given the absence of large radial loads, reducing rotational friction becomes the top demand from a bearing. Consequently, I have chosen to use flanged polymer bushings for reducing the friction in yaw rotation. These bushings are friction fitted into the holes on the top and bottom walls of the C-bracket, where the yaw shafts, attached to the globe, slide through them with a loose fit. The effective vertical slack is ultimately dependant on the tolerances of the manufactured parts; however, slack is substantially reduced by sandwiching the C-bracket between the globe's top

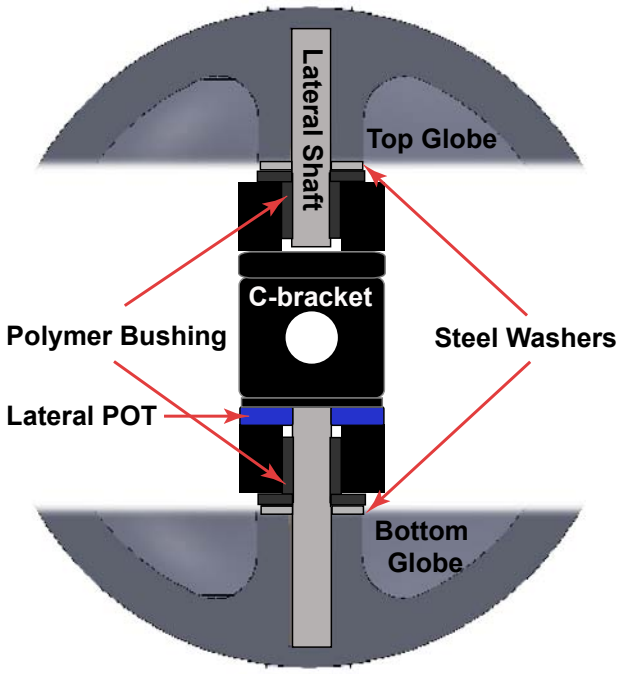

Figure 4.16: Cross section of the globe-C-bracket assembly

and bottom hemisphere, Figure 4.16 illustrates the cross-section of this globe, C-bracket assembly. However, in doing so, as the globe rotates in the yaw direction, the smooth surface of the bushing's flange will move against the uneven surface of the globe's boss. Therefore, in order to avoid the sliding friction due to this movement I have placed a smooth stainless steel washer where the bushing flange meets the globe's boss. Table 4.4 summarizes the details of all the joints explained in this section.

Rotational Direction	# of Joints	Fixed to	Rotates wrt	Fixed by	Rotates in
Yaw	2	Globe	C-bracket	Friction Fit	Polymer Bushings
Roll	1	Back-ring	C-bracket	Setscrew	Radial Ball Bearings
Pitch	2	Outer-ring	Support Stand	Setscrew	Radial Ball Bearings

Table 4.4: The eye robot joint details

Assembly Process

The assembly process begins by the assemblage of the roll joint. I start by snapping a zinc plated steel retaining ring onto the roll shaft. I then tight fit the two bearings onto the shaft, making sure that the bearings and the snap ring all press against each other tightly. Subsequently, this combination is attached to the C-bracket by using lock-tight to fix the outer race of the bearings to the back wall of the bracket. Next, the steel retaining ring is pressed against the rear bearing, sandwiching the bearings between itself and the snap ring. At this point, I pass the roll potentiometer through the end of the roll shaft and glue the sensor onto the bracket's back wall using epoxy. Figure 4.17 illustrates the exploded view of this assembly.

To continue the assembly process, I friction fit the polymer bushings and yaw shafts inside their housing in the C-bracket and the top and bottom globe hemisphere, respectively. The stainless steel washers are then glued onto the surface of the globe's bosses to reduce their effective sliding friction. Finally, before fitting the two globe pieces together, I placed the C-bracket's assembly through the yaw shaft in the bottom hemisphere and glued the yaw potentiometer onto the floor of

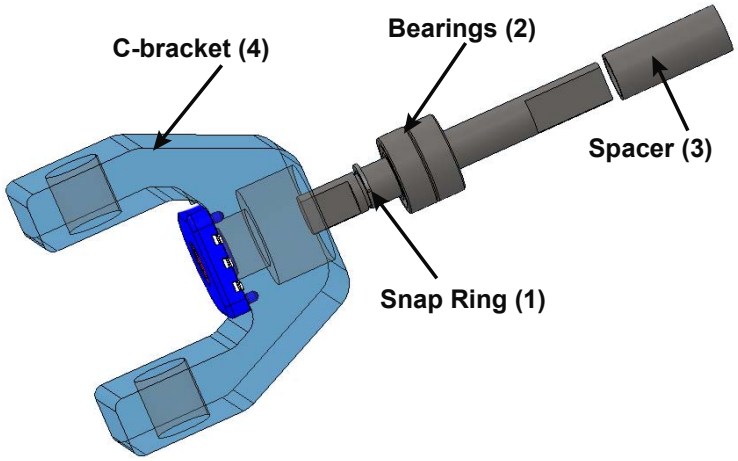

Figure 4.17: C-bracket assembly, the numbers represent the assembly sequence

the C-bracket. Figure 4.18 illustrates the exploded view of this assembly.

The final step is attaching the outer gimbal element to the support stands so that the globe/C-bracket combination can be fastened to it. Thus, before assembling the three pieces of the support stand, I fixed the bearings to the housings inside the two sidewalls of the support stand and glue the pitch shafts to the inner race of these bearings using cyanoacrylate (super glue) . As discussed, this is done to enhance the connection bond of the shaft and the bearings thus eliminating joint play under the forces of the oblique cables. I then sandwich the outer gimbal element between the two sidewalls and fasten it to the pitch shafts as illustrated in the exploded view shown in Figure 4.19. Finally, the pitch potentiometer is glued

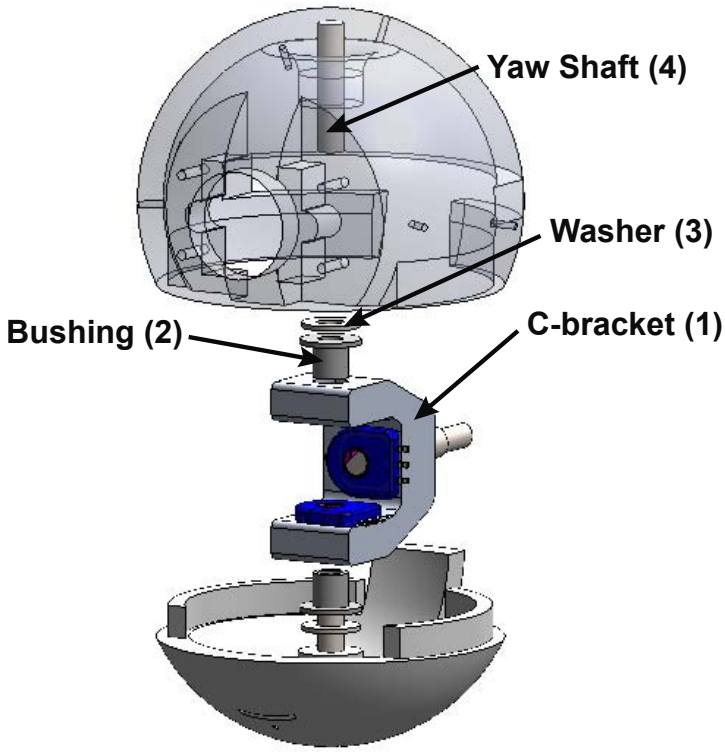

Figure 4.18: Globe assembly, the numbers represent the assembly sequence

to the outer surface of the support stand wall and the globe is attached to the outer gimbal element.

4.3.5 The Eye Robot - Mechanical Characteristics

I have assessed the overall structural strength of the system by evaluating the strength of its building blocks under the two existing conditions of deactivated and activated motors. However, different elements and various parts of the same element are loaded depending on which condition is being considered. When

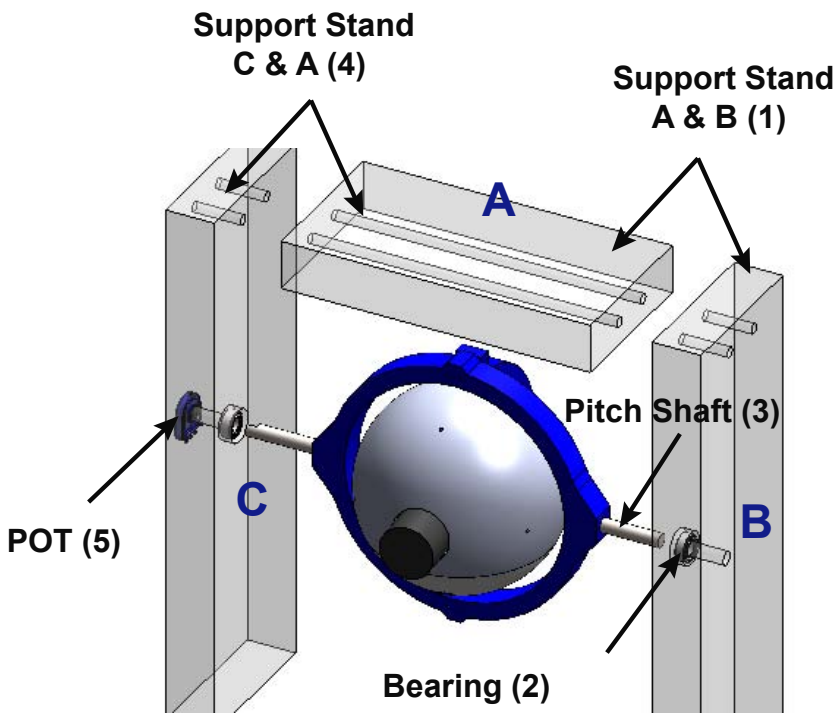

Figure 4.19: Final assembly, the numbers represent the assembly sequence

considering the deactivated situation, the yaw and roll shafts and the elements that these shafts are attached to, namely the back and outer rings, are loaded under the weight of the structural elements. On the other hand, when the motors are activated, the tensioned cables pull on the globe, loading all the gimbal elements. The structural strength of a part under the applied loads is expressed in terms of its factor of safety. However, it is also important for the components to have small deflections since large deflections would affect the positioning accuracy of the

globe. Implementing a definite upper boundary for these deflections is difficult. However, considering the size of the structure I have imposed a rough maximum allowable deflection of 0.1 *mm*.

Under static conditions, when the motors are not running, the weight of the globe and the gimbal elements are the only forces on the structure and thus the shafts are under bending loads. The total weight on the roll shaft is distributed over the length of the two bearings. Thus, by taking the equivalent concentrated load **P** to be at the midpoint of this length we arrive at the beam bending diagram shown in Figure 4.20 with a maximum deflection given by:

$$\delta_{max} = \frac{Pa^2}{6EI}(3l - 1) \tag{4.7}$$

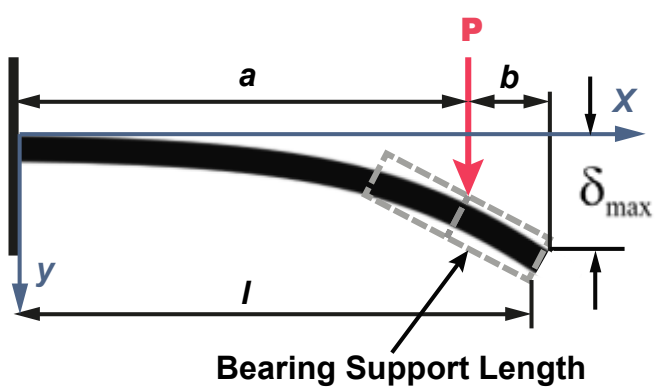

Figure 4.20: Beam bending diagram for the roll shaft

Thus, considering the 69 *g* weight on the 4 *mm* stainless steel[10] shaft, the max-

[10] $E_{SS316} = 1.93 \times 10^{11}\ Pa$

imum deflection of the roll shaft is 8.5×10^{-7} mm, which is considerably below the $0.1mm$. The reaction forces of this mass loading is applied to the holes in back-ring and the inner-bracket, where these elements attach to the roll shaft. The effect of these reaction forces are evaluated using Cosmos, the analysis simulator in Solidworks and quantified as the deflection of the elements and their factors of safety[11]; these results are summarized in Table 4.5.

Gimbal Element	Maximum Deflection [mm]
Inner-bracket	2.15×10^{-6}
Back-ring	1.47×10^{-5}

Table 4.5: Performance of the gimbal elements when the motors are not activated

When all the motors are activated, the recti and oblique cables pull the globe back and to the left and thus, loading all the gimbal elements as shown in Figure 4.21. The applied forces that were used to carry out these analysis were taken to be the tension in the cables when the DC motors were activated by the maximum allowable current. Letting F_{max}, I_{max}, K_i, and R_{pulley} respectively represent, maximum cable tension [N], maximum output current [A] from the amplifier, motor torque constant [Nm/A], and motor pulley radius [m], the maximum tension in each cable is described by the following:

$$T_{max} = I_{max} K_i / R_{pulley} = 7N$$

[11]This factor of safety is calculated based on the $27.6MPa$ yield strength of the aluminum alloy 1060 used

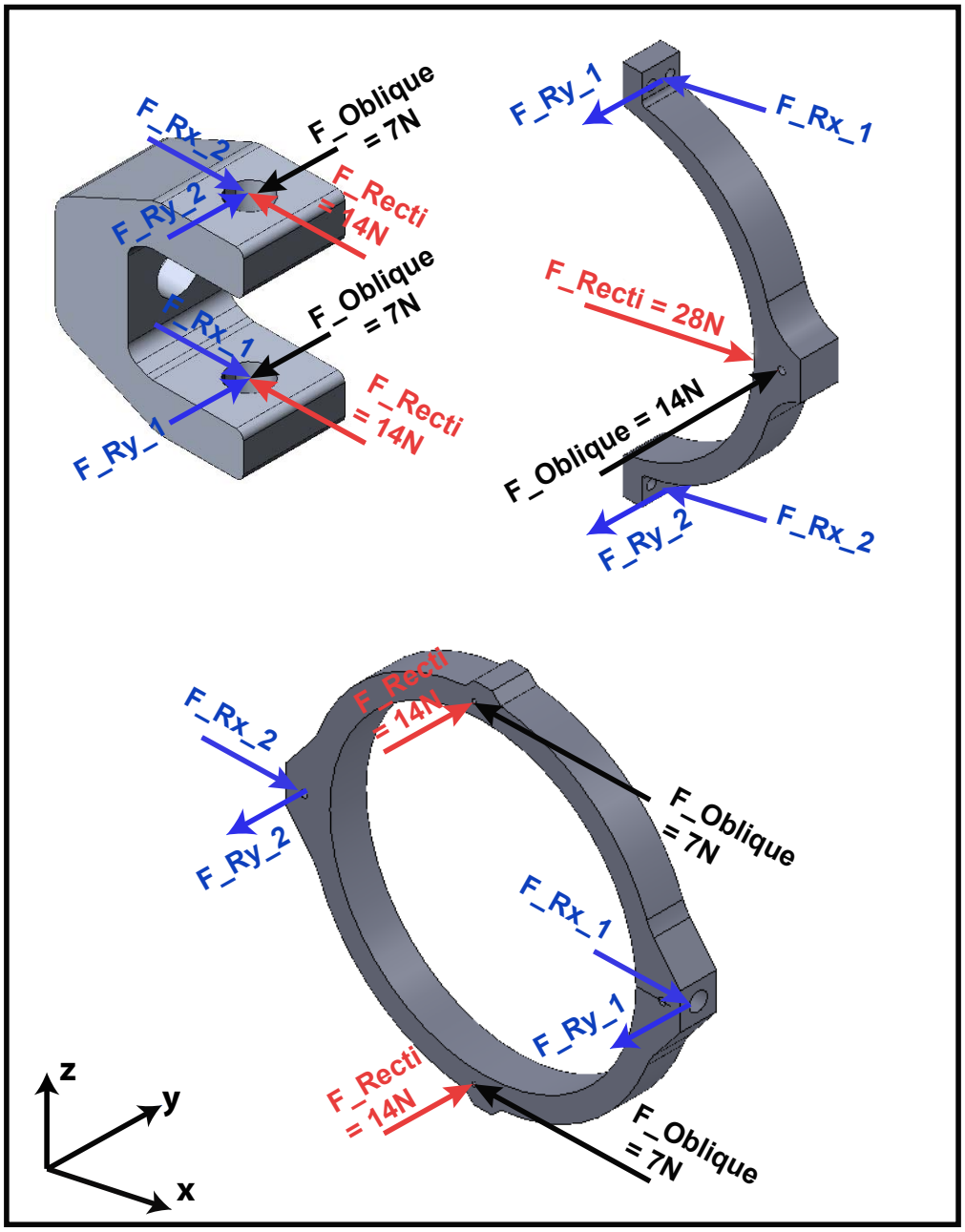

Figure 4.21: Free body diagram of the gimbal elements when the motors are activated (the reaction forces are represented by the blue arrows)

Consequently, $F_{max-back-ring}$, the maximum applied load to the back ring, is calculated by summing the maximum tension (T_{max}) of the four recti cables. While $F_{maxouter-ring}$, the maximum applied load to the outer-ring, is the sum of the maximum tension in the two oblique cables.

Gimbal Element	Maximum Deflection [mm]	F.O.S	Deflection F.O.S
C-bracket	1.1×10^{-3}	7	88
Back-ring	1.9×10^{-2}	2	53
Outer-ring	1.3×10^{-2}	4	8

Table 4.6: Performance of the gimbal elements under activated motors *(Deflection F.O.S is calculated as Def_{req}/Def_{actual}, where the required deflection is set as $0.1mm$)*

The performance of the gimbal elements under these loadings was once again simulated using Cosmos by evaluating the factor of safety and maximum deflection of each element. Table 4.6 summarizes these results. The maximum deflection of all three majorly loaded elements are significantly smaller than $0.1mm$ and the *Deflection F.O.S* in Table 4.6, described as $\frac{Allowable\ Deflection}{Maximum\ Part\ Deflection}$, quantifies these results. The structural strength of each part is quantified by the *F.O.S* values in Table 4.6. These values are based on the yield strength of the aluminum, alloy 1060, used in the eye robot. Once again, it is apparent that the support structure is capable of supporting the maximum possible loads on the device.

Two other components that are considerably loaded when the motors are activated are the two shafts responsible for pitch rotation. The maximum applied loads on these shafts are when the four recti cables are pulling on the globe; this

load is divided across the two steel shafts. Upon viewing the robot structure superiorly, Figure 4.22 illustrates the deflection of a pitch shaft under such loadings. Here **P**, the applied load, is half of the maximum applied loads from the recti motors. The maximum deflection for this beam bending condition is given by

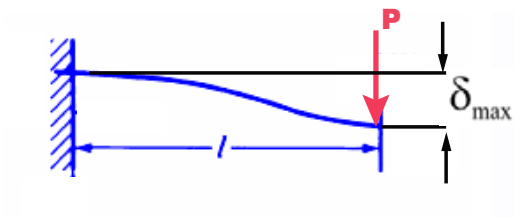

Figure 4.22: Beam bending diagram for the pitch shafts

Equation 4.8, using which the maximum deflection of the pitch shafts are calculated to be 5×10^{-6} mm, a value that is substantially smaller than $0.1mm$.

$$\delta_{max} = \frac{Pl^3}{12EI} \tag{4.8}$$

As it was throughly discussed, the design of the eye robot was greatly influenced by the need to minimize the MI of the gimbal elements, considering the mechanical limitations, and specifically to minimize this effect on yaw rotations. Table 4.7 lists the MI for each of the rotational directions (Yaw, Pitch, roll). The second column of this table describes the directional MI, while the third column illustrates the effect of the gimbal elements on the globe's MI, by expressing the ratio between the actual directional MI, including the gimbal elements, and the globe's directional MI without the gimbal elements. Consequently, it is appar-

ent that the main goal of the design process, namely minimizing the effect of the gimbal elements on the globe's yaw MI, is met given the 1.07 ratio in the yaw direction. Furthermore, as expected, globe's roll MI is also not very much influenced by the gimbal elements, while its pitch MI, the outer most gimbal rotation, is the most effected.

Rotational Direction	MI With Gimbal Parts[Kgm^2]	$\frac{Actual\ directional\ MI}{Globe's\ directional\ MI}$
Yaw	2×10^{-5}	1.07
Pitch	6×10^{-5}	2.6
Roll	2.5×10^{-5}	1.14

Table 4.7: MI of the three rotational directions of the globe, including the gimbal

Chapter 5

Mechatronic Design

The purpose of this chapter is to present the mechatronics design of the eye robot. The first section gives an overview of the the controller architecture including the controlled variables and the corresponding inputs and measured outputs. Next, based on this architecture the selection process of the required sensors and actuators will be discussed. The eye robot kinematics and the control algorithm design that results from it are discussed and finally the implementation of this control algorithm is described at the end of the chapter.

5.1 Architecture of the Controller

As mentioned in Section 3.2, the motivation for the design and implementation of a control algorithm for the eye robot is to evaluate the kinematic and dynamic performance of this robotic eye and as such the algorithm is not meant to mimic the existing oculomotor control theories, this will be left for a future project. Conse-

quently, for the intended purposes of the controller presented here, I have regarded the eye robot as a redundant tendon driven robot that is to be driven to a desired position. More specifically, controlling the globe's 3D orientation is dependent on the ability to project this 3D quantity to the 6D space of the motor angles. The general architecture of such controller is illustrated by the block diagram in Figure 5.4, where:

$$
\begin{aligned}
\theta_d &= \textit{Desired } [3 \times 1] \textit{ globe orientation} \\
\hat{\theta}_g &= \textit{Measured } [3 \times 1] \textit{ globe orientation} \\
\Delta\theta_g &= \textit{Error between the desired globe orientation and the current orientation} \\
J(\theta_g) &= \textit{Jacobian mapping} \\
\Delta L &= [6 \times 1] \textit{ Change in tendon length vector} \\
F &= [6 \times 1] \textit{ Force input vector to the } 6\ DC - \textit{motors}
\end{aligned}
$$

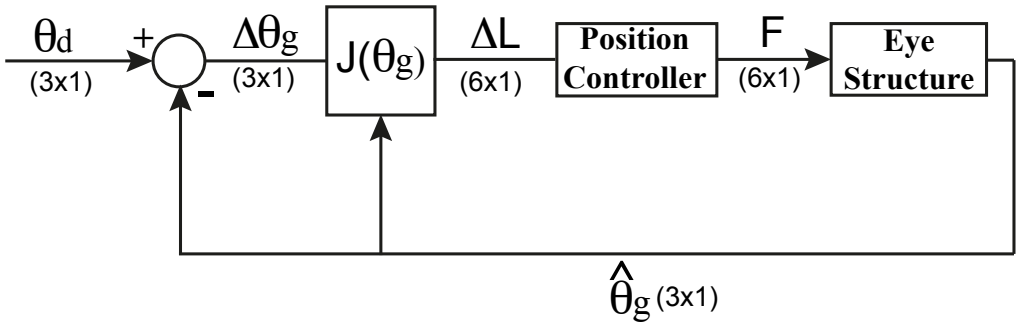

Figure 5.1: General block diagram for position controlling the eye robot

As described by this block diagram, the orientation of the globe of the eye robot can be controlled with a feedback controller. Using the kinematics of the eye robot structure we arrive at the Jacobian, which maps the 3D globe orientation error, calculated as the difference between the desired and the measured values, to the corresponding 6D change in the tendon lengths. Then we position control the 6 motors to the appropriate angle such that the desired tendon length (ΔL) is wrapped around the motor. The output of this controller is the resulting force input to the eye structure.

5.2 Sensors and Actuators

In this section I will present the process of selecting the position sensors and DC motor actuators required to implement the controller described in Section 5.4.

5.2.1 Actuators

As mentioned previously, it was decided to implement the contraction of the 6 EOMs using DC motors. To perform as suitable actuators, the motors must meet the force and dynamic requirements of the eye robot structure. Thus, I began by considering the maximum power that the motors need to supply, which can be described by the following power equation.

$$P_{maxreq} = \tau_{maxreq} \cdot \omega_{maxR} \tag{5.1}$$

Here, τ_{maxR} is the highest required torque and ω_{maxR}, the maximum angular velocity that the globe would have. ω_{maxR} was scaled from the oculomotor system data reported in the literature using the dimensionless Π groups derived in Chapter 4.

A given Π variable stays constant across all dimensions, for instance the dimensionless variable, $\Pi_\omega = \omega\sqrt{\frac{I}{K}}$, would be equal for both the biological eye and the robot. Thus, the maximum angular velocity of the robot can be described, in terms of the biological value, by Equation 5.2.

$$\begin{aligned} &\omega_R(\sqrt{\tfrac{I_R}{K_R}}) = \omega_B(\sqrt{\tfrac{I_B}{K_B}}) \\ &\omega_R = \omega_B\sqrt{\tfrac{I_B K_R}{K_B I_R}} \end{aligned} \tag{5.2}$$

In a similar manner K_R in Equation 5.2 can be found by using $\Pi_K = \frac{K}{\tau}$ and $\Pi_\tau = \frac{\tau^3}{IB^2}$, which respectively correspond to the system's stiffness and input torque. If we assume that the damping of the robot B_R is twice the damping in the biological eye, B_B[1], then the input robot torque can be expressed in terms of the reported maximum $12[mNm]$ [69] active torque of the EOMs as:

$$\begin{aligned} &\tau_{aR} = \tau_{aB}(\tfrac{I_R(2B_B)^2}{I_B B_B^2})^{1/3} \\ &\tau_{aR} = \tau_{aB}(\tfrac{4I_R}{I_B})^{1/3} = 103[mNm] \end{aligned} \tag{5.3}$$

[1]This is a reasonable assumption since the damping of the eye robot will be implemented in software and thus it can be tuned to a desired value.

Thus, K_R is now defined by:

$$K_R = \tau_{aB}(\frac{I_R}{I_B})^{1/3}\tau_{aB}K_B \tag{5.4}$$

Substituting Equation 5.4 in 5.2 $\omega_R = 3.5[rad/s]$. Table 5.1 lists all the biological values and their corresponding robot equivalent[2]. The maximum required power

Table 5.1: Variables of the oculomotor system and their equivalent value in the eye robot

Variables	Oculomotor System [69]	The Eye Robot
I $[Kgm^2]$	4×10^{-7}	6×10^{-5}
$\omega_{max}[rad/sec]$	14	3.5
K $[[mNm]/rad]$	6	52

can now be calculated:

$$P_{maxreq} = \tau_{maxreq} \cdot \omega_{maxreq} = 0.4W$$

Keeping these requirements in mind, I compared them to the the specifications of the available Maxon Amax DC motors in the lab (AMax-25, Maxon Motor AG). These permanent magnet DC motors have a nominal torque rating (i.e. Maximum allowable continuos torque given the a 12V input voltage) of 0.042 $[Nm]$ and a corresponding nominal angular velocity of 325 $[rad/s]$. Therefore, the nom-

[2]In order to assess the worst possible scenario, in these calculations I have used the highest MI of the eye robot, which is in the pitch direction.

inal output power of these motors is:

$$P_{nominalM} = \tau_{nominal} \ .\omega_{nominal}$$
$$= 14W >> P_{maxreq}$$

Considering that the nominal output power of the available motors were much larger than the calculated maximum required torques, I decided to use the Maxon Amax-25 PM DC motors. However, upon making this decision there are other factors that must be taken into consideration such as the effect of the motor friction. Specifically, the minimum required torque from these motors must be larger than the no load torque of the maxon motors, considering the pulley diameters available for the given motor shafts. For these motors I have selected a pulley with a groove diameter of $13mm$. The minimum torque of the EOMs is the tonic torque that exist when the eye is stationary and it is reported to be $4.9[mNm]$ [40, 52], which scales to $42[mNm]$ given the eye robot dimensions. Thus, to provide this minimum torque the motor must supply,

$$\tau_{Mmin} = \tau_R \frac{R_{Pulley}}{R_{globe}}$$
$$\tau_{Mmin} = 9 \ [mNm]$$

The reported no load friction for the Maxon motor is $1.5[mNm]$ which is more than 8 times smaller than the minimum requirements and thus it would not create any limitations. Furthermore, although power requirements are a good initial tool for selecting the appropriate DC motor, it is not sufficient for the motor to only be

capable of producing the required power, rather it must be capable of providing the appropriate maximum torque and speed without exceeding its power ratings. Thus, considering the pulley ratios, the maximum required torque from the motor is $\tau_M = 103[mNm]\frac{13mm}{60mm} = 22[mNm]$, which is about half of the nominal torque of the Maxon Amax-32. Similarly the maximum required speed from the motor is $\omega_M = 3.5[rad]\frac{60mm}{13mm} = 16[rad/sec]$, compared to the $325[rad/sec]$ nominal speed of the selected motors. It is therefore apparent that the selected motors exceed the requirements by a large margin and thus they would be able to manage factors, such as system friction, that are not accounted for in the calculations presented here.

5.2.2 Sensors

As discussed in Section 5.1 the orientation of the globe will be controlled using the feedback system. Therefore, we need a position sensor to measure the yaw, pitch and roll of the eye robot considering the biological and mechanical design requirements.

Foveola, the portion of the fovea with the highest visual acuity has a 0.35 mm diameter, which translates to $1deg$ of visual angle. Therefore, the globe orientation should be controlled to a fraction of this value, which we have selected to be $1/10^{th}$, and this requirement should be reflected in the resolution of the position sensor. Consequently, the selected sensor must measure angles with an accuracy of $< 0.1°$. Furthermore, as illustrated in the controller block diagram, illustrated in Figure 5.4, the controlled quantity is a change in the globe orientation and thus,

it is important to know where we are starting from. This means that we need an absolute measurement of the yaw, pitch and roll. A factor that played an important roll in the selection process of the angle sensor was the size and the configuration of the sensor. As briefly discussed in Chapter 4, two of the three sensors must fit on the C-bracket inside of the globe, a requirement that imposed a big restriction on the selection process. In view of the requirements discussed in the above

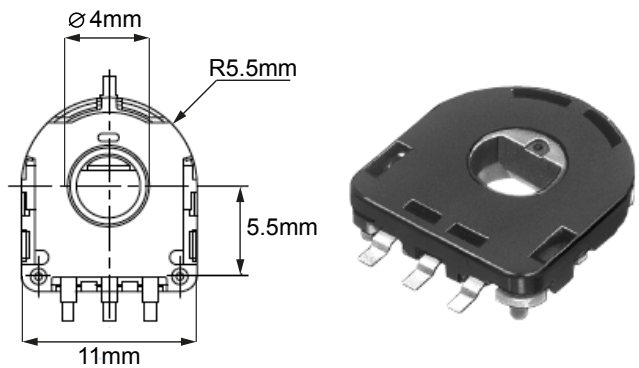

Figure 5.2: Potentiometers used for measuring the angular position of the globe

paragraph, I have chosen to use potentiometers (RDC506, Alps Electric, Tokyo) for measuring the yaw, pitch and roll of the eye model. The primary reason for selecting these sensors is their small dimensions, Figure 5.2. A further advantage of potentiometers is that they produce absolute angle measurement. When driven at its rated voltage of 5 V, RDC506 has a linear output with a slope of 0.016 V/Deg, Figure 5.3. The potentiometers are connected to a 16-bit analog to digital convertor (AD) (PCI-6620, National Instruments, USA). Therefore, considering the 320° angular range of the potentiometer, the effective resolution is

given by $\frac{320^\circ}{2^{16}-1} = 0.005^\circ$, which is 2 orders of magnitude smaller that the desired maximum angular error of 0.1°.

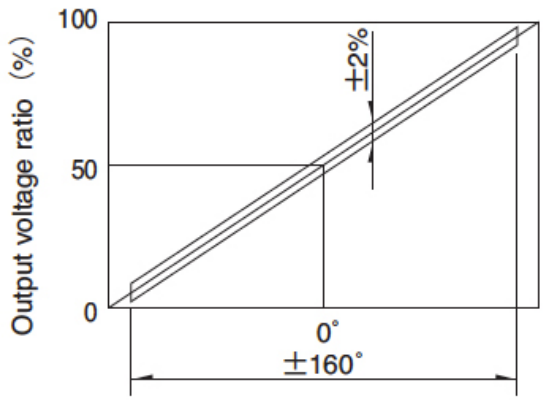

Figure 5.3: Voltage output of the potentiometer, given the angular movement input. This plot is taken from RDC506 spec sheet.

A draw back of using a potentiometer is the friction that it introduces to the system. It is important that this friction is small relative to the operating torques. RDC506 has a maximum friction torque of $2[mNm]$, which is much smaller than the $42[mNm]$ tonic eye robot torques.

5.3 Kinematics and Control

This section includes the derivation of the control algorithm discussed in Section 5.1, the block diagram of the controller is repeated here in Figure 5.4. This control algorithm requires analyzing the kinematics of the eye robot structure and implementing a position controller.

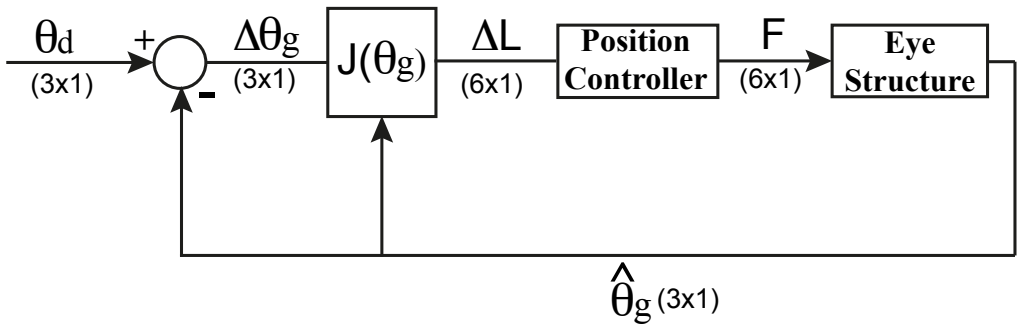

Figure 5.4: General block diagram for position controlling the eye robot

5.3.1 Kinematics

In this section I have used the kinematics of the eye robot structure to arrive at the Jacobian mapping of the controller in Figure 5.4. The presented Jacobian would map 3D displacements of the globe to the corresponding 6D changes in the tendon lengths.

The rotational kinematics of the eye can be expressed with the aid of a rotation matrix. To define this rotational kinematics, let us consider two right handed coordinate systems, a *globe* frame, denoted by **g** in Figure 5.5, which is attached to the centre of the globe and moves with the globe, and a *world* frame, denoted by **w** in Figure 5.5, which is fixed to the centre of the globe and stays stationary as the globe rotates. Furthermore, we define the reference or primary position of the globe as the instance in space where the head and globe coordinates coincide with each other. Then the globe-fixed coordinate frame's transformation matrix is

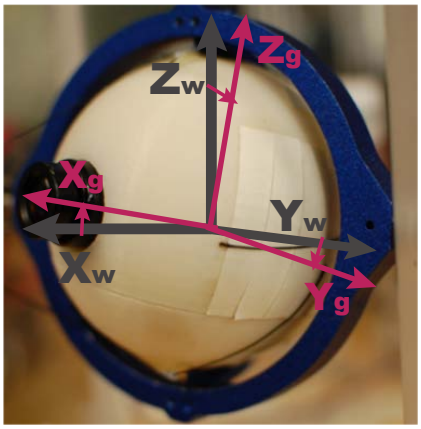

Figure 5.5: We define two right hand coordinate systems both of which have origins at the centre of the globe. The *globe coordinate* rotates with the globe, while the *world coordinate* stays fixed.

given by matrix multiplication of the yaw, pitch and roll rotation matrices given

in Equations 5.5 - 5.7[3].

$$R_{yaw}(\alpha) = \begin{vmatrix} cos(\alpha) & -sin(\alpha) & 0 \\ sin(\alpha) & cos(\alpha) & 0 \\ 0 & 0 & 1 \end{vmatrix} \tag{5.5}$$

$$R_{pitch}(\beta) = \begin{vmatrix} cos(\beta) & 0 & sin(\beta) \\ 0 & 1 & 0 \\ -sin(\beta) & 0 & cos(\beta) \end{vmatrix} \tag{5.6}$$

$$R_{roll}(\gamma) = \begin{vmatrix} 1 & 0 & 0 \\ 0 & cos(\gamma) & -sin(\gamma) \\ 0 & sin(\gamma) & cos(\gamma) \end{vmatrix} \tag{5.7}$$

The order of this matrix multiplication is determined by the kinematics of the gimbal, which has a serial kinematic chain with intersecting joint axes. Therefore, the gimbal imposes rotations about a moving coordinate frame (known as *passive rotation*) with a pitch, roll, yaw rotation sequence and thus the corresponding transformation matrix for the globe-fixed coordinate is given by

$$\mathbf{R_g} = \mathbf{R_{pitch}}\mathbf{R_{roll}}\mathbf{R_{yaw}}$$

This can be used for estimating the orientation of the globe from the gimbal joint rotation sensors.

[3]Vector quantities are distinguished by bold font lower case variables and matrices are differentiated by bold font upper case variables.

Subsequently, in order to drive the globe to a desired orientation expressed by $\mathbf{R_g}$, we must transform this 3D orientation to the equivalent motor angles. This can be done by relating a small displacement $\Delta\mathbf{R_g}$ of the globe to a small displacement of the motors ($\Delta\theta$).

A small (right) displacement $\Delta\mathbf{R_g}$ of the globe is most conveniently parameterized in exponential coordinates. Namely, I parametrize $\Delta\mathbf{R_g}$ by a unit vector representing the equivalent rotation axis and the angle describing the rotation about this axis. There are a number of methods for computing the exponential coordinate of a rotation matrix [11]. Here I have used the *matrix-to-quaternion* and *quaternion-to-exponential* formula to convert R_g to its exponential form. A quaternion is defined to be $(q_o, \mathbf{q})$, where q_o is a scaler and $\mathbf{q}$ is a vectore. Thus, I have formulated a conversion from SO(3) to the angle-axis form as follows:

Matrix to Quaternion[4]

$$\mathbf{d} = \mathbf{R_g} - \mathbf{R_g}^T, \quad \mathbf{r} = \begin{pmatrix} -\mathbf{d}(2,3) \\ \mathbf{d}(1,3) \\ -\mathbf{d}(1,2) \end{pmatrix}$$

$$\theta_{gq} = tan^{-1}\left(\frac{\| \mathbf{r} \|}{trace(\mathbf{R_g}) - 1}\right) \tag{5.8}$$

$$\mathbf{q_g} = [\underbrace{cos(\theta_{gq}/2)}_{q_{og}} \quad \underbrace{\frac{\mathbf{r}}{\| \mathbf{r} \|} sin(\theta_{gq}/2)}_{\mathbf{q_{gq}}}]$$

[4]The g subscripts refer to the globe quantitates.

Quaternion to Exponential

$$\begin{aligned} \phi &= 2cos^{-1}(q_{og}) \\ \mathbf{v} &= \begin{cases} \frac{\mathbf{q_{gq}}}{sin(\phi/2)} & \text{if } \Phi \neq 0 \\ 0 & \text{if } \Phi = 0 \end{cases} \end{aligned} \tag{5.9}$$

This parameterization can then be described by:

$$\Delta\mathbf{R_g} = \exp[\theta_\mathbf{g}]$$

where the direction of the vector θ_g describes the direction of the unit vector $\mathbf{v}$ and its magnitude is the angle of rotationθ_g. The bracket ([ ]) notation is used to represent the matrix of the cross-product $\theta_g\times$.

For control we need to relate the globe's displacement (θ_g) and torque (τ_g) to the cable motors' displacements (θ) and torque (τ). If we assume, as in [8], that a cable i takes the shortest path between its insertion point $\mathbf{p}_i$ and the anchor or pulley point $\mathbf{a}_i$, then

$$\mathbf{N}_i = \frac{\mathbf{R_g}\mathbf{p}_i \times \mathbf{a}_i}{\parallel \mathbf{R_g}\mathbf{p}_i \times \mathbf{a}_i \parallel} \tag{5.10}$$

Here $\mathbf{N}_i$ is the vector normal to the plane of the cable at the insertion, expressed in world coordinates. Therefore a tension f_i in the cable, wrapped on a globe of radius r_g, will contribute a torque $\tau_{g,i} = r_g f_i N_i$ on the globe. The tension is

produced by the DC motor, wrapping around a motor pulley of radius r_m. Thus

$$\tau_{g,i} = r_g \frac{\tau_m}{r_m} \mathbf{N}_i. \tag{5.11}$$

From this we can extract and assemble the columns of the Jacobian $\mathbf{J}$, which is defined by the relation $\tau_g = \mathbf{J}^T \tau$.

$$\mathbf{J}^T = r_g \left(\frac{1}{r_1} \mathbf{N}_1 \cdots \frac{1}{r_6} \mathbf{N}_6 \right). \tag{5.12}$$

Then *principle of virtual work* can be used to relate $\Delta\theta_{\mathbf{g}}$ to $\Delta\theta$. Namely, the work done by the motors must be equivalent to the work done by the globe. Therefore,

$$\tau_{\mathbf{g}} \,.\, \Delta\theta_{\mathbf{g}} = \tau \,.\, \Delta\theta$$

This inner product can also be expressed by

$$\underbrace{\tau_{\mathbf{g}}{}^T}_{\tau^T\ \mathbf{J}} \Delta\theta_{\mathbf{g}} = \tau^T \Delta\theta$$

Therefore the displacements are now related by

$$\Delta\theta = \mathbf{J}\Delta\theta_g$$

5.3.2 Controller

The block diagram in Figure 5.6 expands on the more general controller architecture discussed earlier in the chapter. Here the ”Position Controller” block is expanded to illustrate the detail of this part of the controller. In this section the final control architecture used in the eye robot will be described.

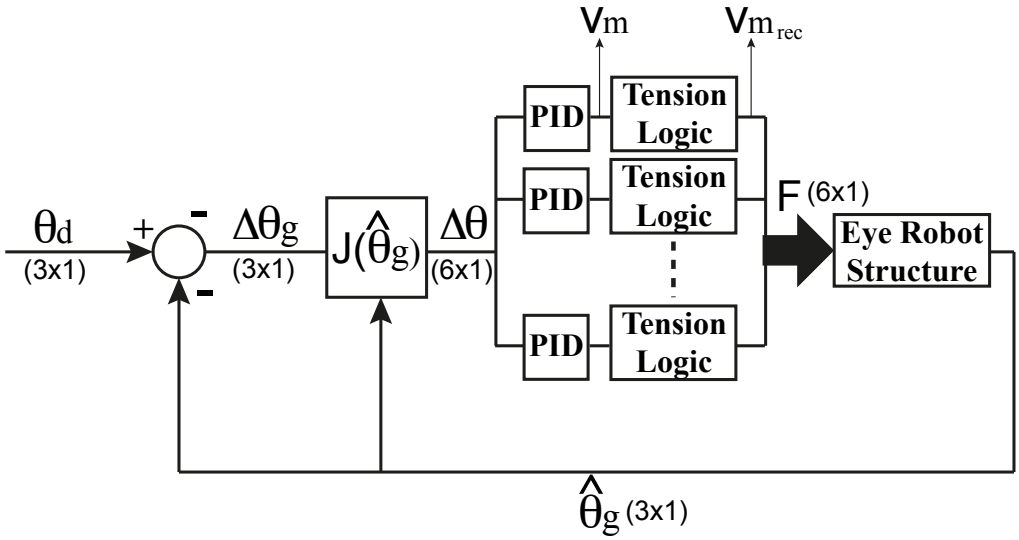

Figure 5.6: Block diagram for the position controller used to drive the eye robot. $\hat{\theta}_g$ represents the current globe angle measured by the potentiometers.

The $J(\hat{\theta}_g)$ block in Figure 5.6 uses the kinematics mapping developed in the previous section to relate globe orientation to motor angles. $J(\hat{\theta})$ is updated every time step based on the measured globe angles. For a desired globe orientation, θ_d, $J(\hat{\theta}_g)$ maps the globe position error, $\Delta\theta_g$, to tendon displacements, ΔL, which are scaled by the motor pulley diameters to correspond to motor angle commands,

$\Delta\theta$. This relationship is described by the following equations

$$\Delta\theta = r_g \left(\frac{1}{r_1}\mathbf{N}_1 \cdots \frac{1}{r_6}\mathbf{N}_6 \right)^T \Delta\theta_g$$

Finally, given the motor angle commands, the motors are current controlled to the desired displacements using a PID controller.

The eye robot is a 2N configuration tendon driven system, using the classification of tendon driven robots in the literature [24]. In a 2N configuration, one DOF of the system is controlled by 2 actuators pulling on antagonist tendons. Given the structure of this antagonist system, the torque from each motor can be transformed to the joint only by pulling (i.e., you can not push on a cable). A control challenge that emerges from this characteristic of a 2N tendon driven robot is ensuring that tendons are tensioned under both passive (antagonist) and active (agonist) conditions. Therefore, we have implemented a simple logic similar to [24] to ensure that the cables are tensioned at all times. This is represented by the "Tension Logic" block in Figure 5.6. The block takes the motor voltage command, V_m, and outputs the rectified motor voltage command, V_{mrec} using the following logic:

$$\begin{aligned}
&if\ V_m > 0 \\
&\quad output = V_m \\
&else \\
&\quad output = 1
\end{aligned}$$

5.4 Implementation

I programmed and designed the control algorithm using Simulink, a visual programming language developed by MathWorks. Simulink is an interactive environment whose "customizable block libraries" greatly simplifies the design of the control system. Furthermore, the "Real-Time Workshop" in Simulink provides a convenient procedure for testing and implementing the designed controller on the the eye robot. The real time workshop consists of the Host Computer, the Target Computer, and the plant which includes the sensors and the actuators as well as the mechanical structure, Figure 5.7 maps the relationship between these three components for the setup used to control the eye robot.

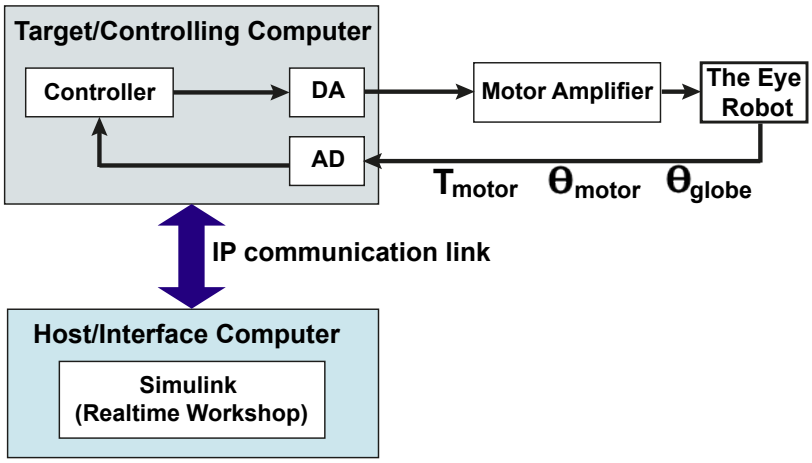

Figure 5.7: Communication map of the controlling computer and the eye robot

The host computer runs Simulink, Simulink Coder, and a C compiler and communicates with the target via an IP communications link. Through this connection

the Simulink model code, generated by Simulink Coder, is downloaded onto the target computer, which ultimately sends motor commands and receives sensor data to and from the eye robot through the digital to analog convertor (DA) and AD boards. The sensor data saved on the target computer, can either be viewed by the target or acquired and saved by the host to further examine the performance of the controller.

The PID controller outputs a current command corresponding to desired motor torque.Thus, we require a motor control amplifier capable of current control mode. Furthermore, position control of a motor requires the motor control amplifier to be capable of controlling acceleration and deceleration in both directions. Finally, input and output of the amplifier must have a linear relationship to eliminate the effect of the motor amplifier on the dynamics of the eye robot. To satisfy the above requirements, I have chosen a Maxon servomotor control amplifier (LSC 30/2, Maxon Motor AG). LSC 30/2 is a linear 4 quadrature servo controller capable of accelerating and decelerating Amax 32 in both directions. This servo amplifier has a number of operational modes, including a current control mode. In the current control mode LSC 30/2 takes as input voltage commands (between $0 - 10[V]$) from the PID controller and outputs current commands (between $0 - 2A$) proportional to the commanded voltage, thus keeping the motor current at the value predetermined by the PID controller.

Chapter 6

Assessment

In this chapter, the mechanical and mechatronics capabilities of the eye robot and its ability to function as a testbed for scientific research is assessed. First, I evaluate the tracking accuracy of the eye robot for the principal directions of rotation and 2D trajectories. I then verify that the robot's MIs are comparable with the scaled inertia of the real eye. Finally, I assess the capability of the eye robot to achieve mechanical responses similar to the real eye. In particular, the rise time and peak velocity of the robot's response to commanded steps, which resemble saccadic eye movements, are compared to saccade recordings from human subjects.

Tracking Accuracy

As explained in section 3.2, the aim is for the eye robot to have a fast, overdamped response and to reach the target position to within $\frac{1}{10}^{th}$ of a degree. An

overdamped response is characterized by the percent overshoot (P.OS) [1] of the step response. Specifically, a completely overdamped response would have zero *P.OS*.

I use step inputs in yaw, pitch and roll to assess the quality of tracking in the principal directions of rotation. Figures 6.1 - 6.3 illustrate the position and velocity profile of the eye robot's response to step inputs in the principal directions. The dashed line represents the target position while the solid line illustrates the eye robot's response to these inputs.

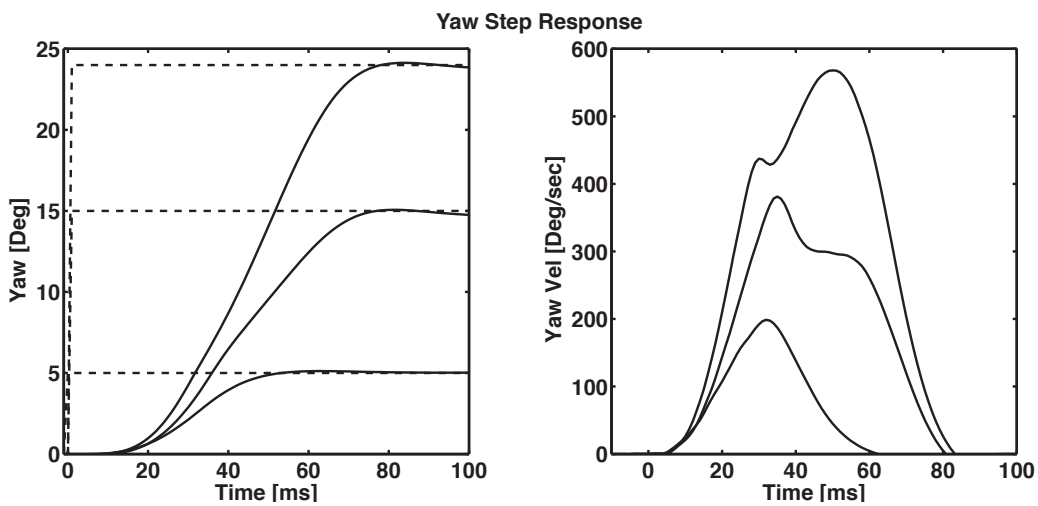

Figure 6.1: System's response to 5°, 15°, and 24° inputs in yaw

Similar step inputs were repeated 50 times in all three rotational directions and the resulting mean steady state error (E_{ss}), and *P.OS* are presented in Table 6.1. The E_{ss} in all directions are on the orders of $\frac{1}{100}^{th}$ of degrees, demonstrating that the eye robot is in fact capable of achieving the desired tracking accuracy

[1] $P.OS = 100 \times \frac{Overshoot}{Steady\ state\ value}$

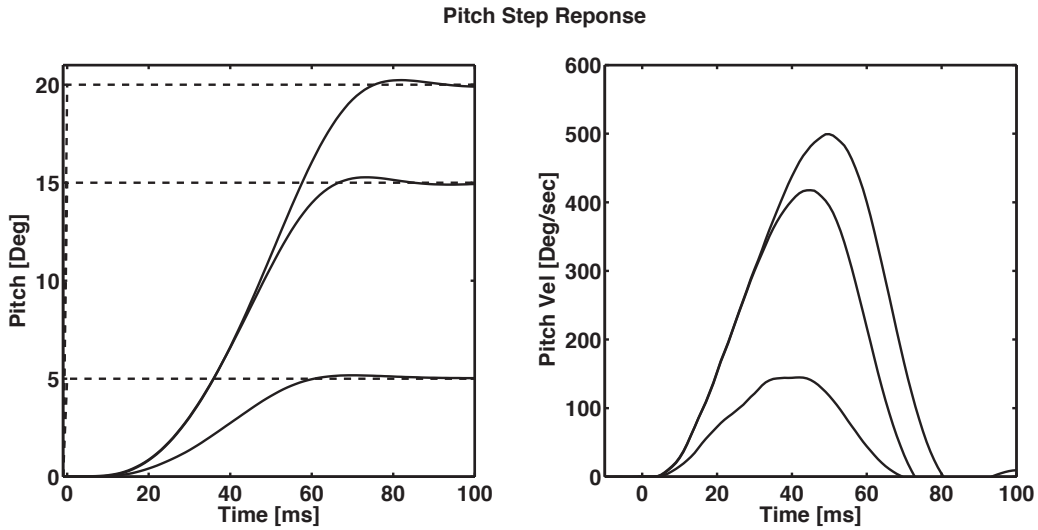

Figure 6.2: System's response to 5°, 15°, and 20° inputs in pitch

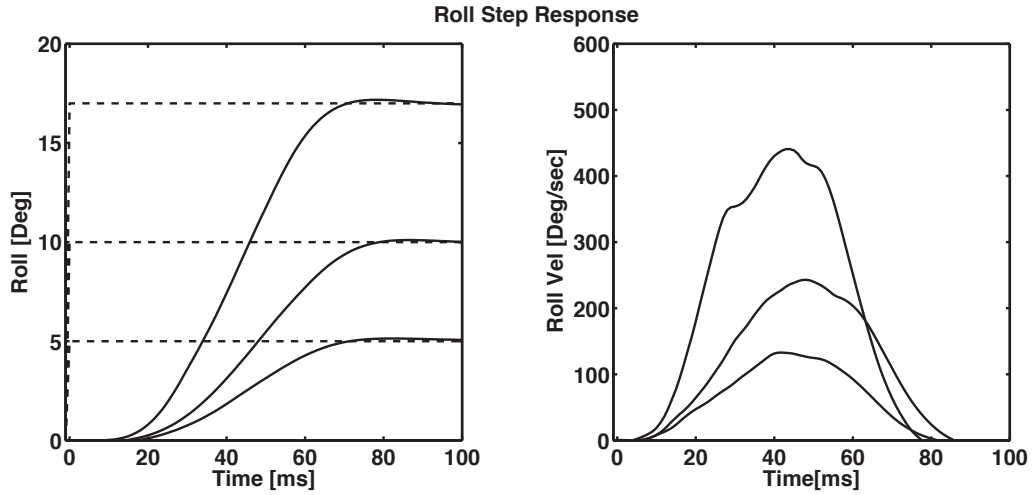

Figure 6.3: System's response to 5°, 10°, and 17° inputs in roll

in the three principal directions of rotation. Furthermore, examining the step responses reveals that for the most part they are close to overdamped with very small overshoots. These small overshoots are attributed to the tradeoffs involved in designing the controller. Achieving a fast overdamped response using a PID controller introduces two potentially opposing goals: short rise-time and low overshoot, which enforces optimizing the PID parameter choices to achieve the best tradeoff between these requirements. Namely, an overdamped response requires decreasing the proportional gain and increasing the derivative gain, both of which increase the rise-time of the response. This effect can therefore be minimized if we allowed for a slower rise-time. However, the most important characteristic of a saccadic movement is the speed of the saccade and, in fact, the saccade responses can be accompanied by small overshoots. As such, here I have chosen achieving a small rise-time as the primary goal and have accepted small overshoots.

Table 6.1 lists the statistics of these values for 50 step inputs with the step magnitudes varying between $5^\circ - 30^\circ$, in the three directions.

Table 6.1: Statistics for steady state error (E_{ss}) and percent overshoot ($P.OS$) for the eye robot's step input response based on 50 data points

Rotational Direction	E_{ss} [Deg]	P.OS [%]
Yaw	0.03 ± 0.04	1 ± 0.25
Pitch	0.06 ± 0.07	2.2 ± 0.95
Roll	0.05 ± 0.06	1.6 ± 0.50

To evaluate the system's ability in tracking 2D trajectories I commanded rotations about axes on the coronal plane[2] at a rate of 50 Deg/s. The rotations mapped

[2]The vertical plane that divides the body into ventral and dorsal planes

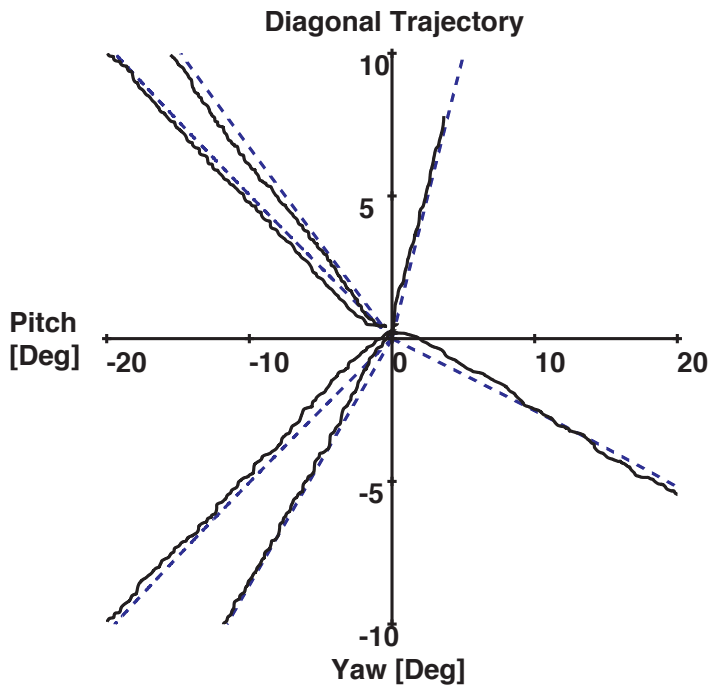

Figure 6.4: System's response to rotations about axis on the coronal plane

to a linear and a circular path on the field of view. Figures 6.4 and 6.5 illustrate responses of the eye robot to these commanded trajectories. Once again, the dotted line is the commanded path and the solid line represents the system's response. The trajectories were each repeated 10 times and the resulting maximum errors are reported in Table 6.2.

Table 6.2: Maximum error for the circular and linear trajectories

Trajectory path	Max Error [Deg]
Linear	2 ± 0.5
Circular	3 ± 0.1

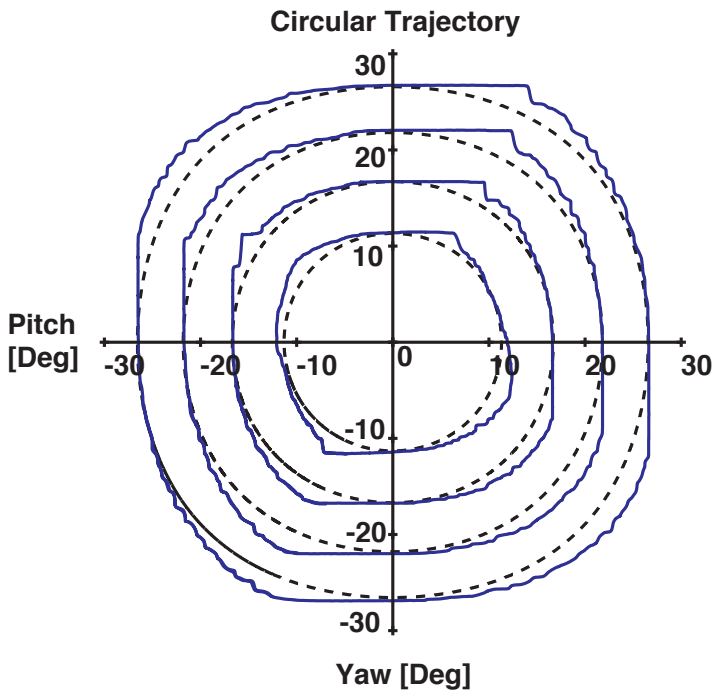

Figure 6.5: System's response to a circular path on the field of view

These results indicate that the tracking accuracy of the eye robot is decreased considerably, for commanded 2D trajectories. Such large tracking errors are likely due to the static friction of the motors. This is apparent when considering the circular trajectory, because the maximum deviation of the robot from its commanded path occurs at the 4 corners of the circle, where the velocity becomes zero instantaneously and thus, the motors must stop and start moving. Furthermore, when considering a linear trajectory the error must decrease over time. Figure 6.6 illustrates that the error profile of a given linear path increases until it reaches a maximum before starting to decrease and remaining at a constant value for the rest of the path.

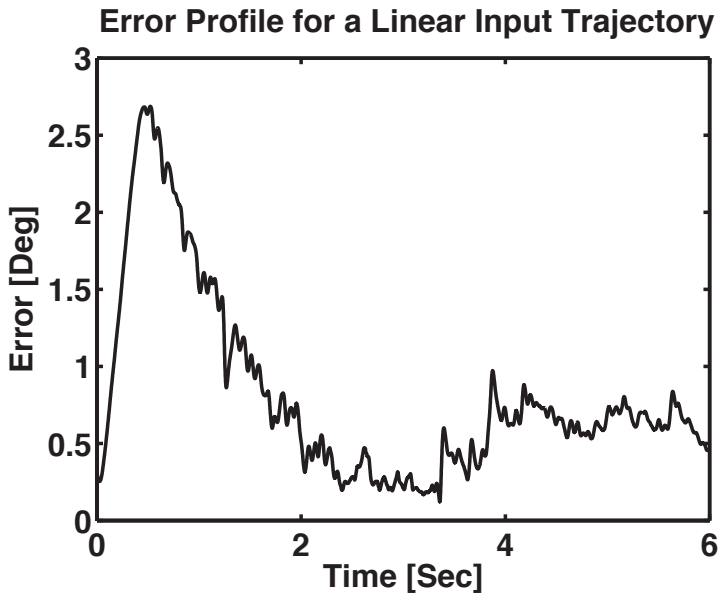

Figure 6.6: Error profile for a linear trajectory input

The assumption that motors static friction is responsible for the large tracking errors found can be validated further by comparing the measured maximum errors and the minimum required error that would put the motors in motion, considering their static friction. The reported static friction of the Maxon Amax motors is quantified by a no-load current of 58 mA. Thus, under no-load conditions, a minimum of 58 mA is required to rotate the motor shaft. Furthermore, these motors are being controlled through amplifiers that provide a linear mapping between commanded voltages (from the PID output), varying between $0\ V - 10\ V$, and motor current inputs, varying between $0\ A - 1.5\ A$. This means that a minimum of

$$\frac{0.058\ A}{\frac{1.5\ A}{10\ V}} = 0.4\ V$$

is required to rotate the motor shaft. Considering that the PID controller has a proportional gain of 8, this voltage value corresponds to a angle input of,

$$\frac{0.4\,V}{8} = 0.05\,rad = 2.9\,Deg$$

Consequently, a minimum of about 3 *Deg* error is required before the motors are able to rotate. This value is comparable with the maximum reported errors in Table 6.2. Consequently, in order for the eye robot to be able to perform trajectories with the acceptable tracking accuracy of $0.1\,Deg$ $(0.002\,rad)$ the motors must be replaced with ones with a lower static friction value or we should explicitly compensate for the static friction in the control algorithm. One such algorithm has been developed by Astma [4].

Substitution of the motors would be further justified if it is found that the motor static torques are in fact the dominating source of friction in the system. To examine this possibility I have calculated and compared the motor stiction to the friction forces, and their subsequent effect on the required globe torque, that are present in the following system components:

- Dyneema tendons and globe surface
- Dyneema tendons routing through plastic tubes
- Bearing and bushing frictions

The Maxon motors have a reported static friction torque of 1.5 *mNm*. This is

converted to its equivalent torque on the globe, τ_{mg}, by the following equation.

$$\tau_{mg} = 1.5\ mNm\ \frac{R_g}{R_m} = 7\ mNm$$

Here R_g and R_m are respectively the globe and motor pulley radius. I have quantified the effect of the friction between the cables and the globe surface by calculating the maximum torque that the dyneema cable could apply to the globe before it slips. This is given by the product of the normal force exerted on to the globe due to the tension in the cable, and the coefficient of static friction of dyneema. During static conditions the cables are tensioned by the motors with 0.84 N. The normal force due to this tension can be calculated by examining the FBD of the cable, illustrated in Figure 6.7. Considering the force balance of this FBD, N, can

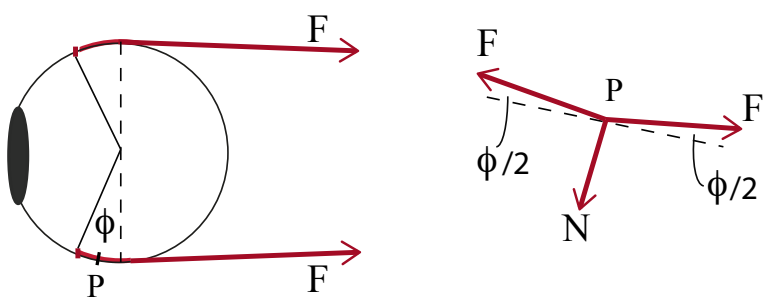

Figure 6.7: FBD of a tensioned cable with a wrap angle Φ

be expressed as a function of the cable tension, F, and the wrap angle of the cable, Φ by:

$$N = 2F\,sin(\Phi/2)$$

The maximum possible wrap angle is 60°, when the globe is fully rotated to

the right or left, and dyneema's coefficient of static friction, μ_d, ranges between $0.08 - 0.12$. Thus, the maximum torque, τ_{gc}, that is applied to the globe due to the cable -globe friction is:

$$\tau_{gc} = 2\mu_d F sin(\Phi/2) R_g = 3\ mNm$$

Similarly, routing of the cables through nylon tubes introduces a friction torque, τ_{cr}, on the globe that can be described as a function of the cable entering angle, θ_i, and exiting angle, θ_o, as illustrated in Figure 6.8. In this figure ΔF represents

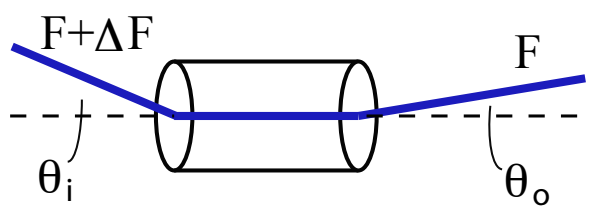

Figure 6.8: Routing of the cables through nylon tubes

the force dissipated due to friction which is approximated by,

$$\Delta F = F(e^{\mu(\theta_i+\theta_o)} - 1) = 0.072\ N$$

Therefore, the torque on the globe due to this friction force is, $2\ mNm$. Finally, the bearing friction torque,τ_{bb} is calculated to be

$$\tau_{bb} = F_r \mu_{bb} r_{ib} = 0.01\ mNm$$

Here, F_r is the maximum radial force, distributed between the two pitch ball bearings, and it is applied by the tension in the four recti cables as they pull the globe posteriorly. μ_{bb} is the coefficient of static friction, which is reported as 0.003 for the single row ball bearing used here, and finally r_{ib} is the bearing's bore radius. The friction in the bushings of the yaw joints are maximum when the globe is

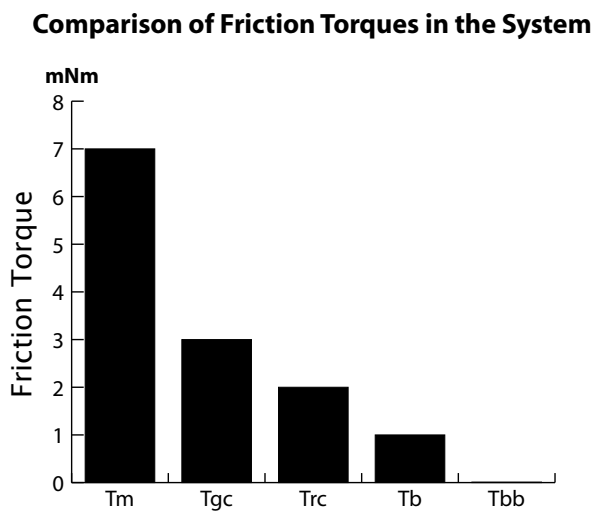

Figure 6.9: Bar graph comparing the friction torques in the system. T_{mg} is the motor static friction torque, T_{gc} is the dyneema cable and globe surface friction torque, T_{rc} is the friction torque due to the routing of the cables, T_b is the bushing friction torque, and T_{bb} is the ball bearing friction torque.

being pulled back by the 4 recti muscles, with a force F. Therefore, considering that the coefficient of friction, μ_p, of the bushing polymer (G300), ranges between 0.1 and 0.15, the maximum friction torque, τ_b, on the globe due to the polymer

bushings is calculated to be

$$\tau_b = F\mu_p r_s = 1\ mNm$$

where r_s is the radius of the shaft. These results are illustrated by the bar graph in Figure 6.9. From this graph it is easy to realize that the motor stiction force is indeed the dominant source of friction in the system, by more than 2 times, and thus reducing this friction source would have a significant effect on the performance on the robot.

Assessment of MI

Another significant factor, for assessing the capability of this eye system to emulate biologically plausible motions, is the MI of the system. It has been shown that the inertial forces in the biological eye are negligible in comparison to the existing passive forces [52]. Thus, a primary design goal is to maintain this relationship amongst the model's forces and many of the design decisions are driven by the requirement of reducing the MI especially in yaw, which is the most frequent eye movement direction. To determine whether the model MIs are sufficiently small, we need to compare the model's MIs with the scaled MI of the real eye. The design requirement is met if the model's MIs, in all three principal directions, are smaller than or in the same order magnitude of the scaled MI.

An exact scaling of the real eye's MI requires detailed geometric and material properties, which are difficult to find. Nonetheless, we could estimate the MI scale

factor to the right order of magnitude, by viewing the real eye and the model as spheres. In doing so, the moment of inertia of the model and the real eye can be expressed by,

$$I \propto Mr^2 \;\; \Rightarrow \;\; I \propto (\rho r^3) r^2$$
$$I \propto r^5$$

Then the scale factor between the MI of the real eye, I_E, and the model eye, I_M, is defined by the ratio of their radii as follows,

$$\frac{I_M}{I_E} = (\frac{R_M}{R_E})^5$$

Therefore, considering that the eye robot's globe diameter is 2.5 times the real eye, the $4E-7\ Kgm^2$ inertia of the real eye is scaled, by a factor of about 100, to $4E-5\ Kgm^2$.

Figure 6.10 compares the model's inertias, in its principal directions (I_y, I_p, I_r), with this scaled MI, I_s. It is evident that the model's MI in all 3 directions are within the same order of magnitude as the scaled MI. These results imply that the anisotropy of the MIs of yaw, roll and pitch, imposed by the gimbal structure, will not have a significant impact on the dynamic response of the system since all inertial forces are negligible. MI, I_s.

The MIs used in Figure 6.10 only include the gimbal and the globe and ignore the motor rotor's inertia. Thus, for a more accurate comparison with the scaled biological MI, which includes the inertia of the EOMs, we must include inertia of the motors. Considering that the motors rotate about their own axis and are connected

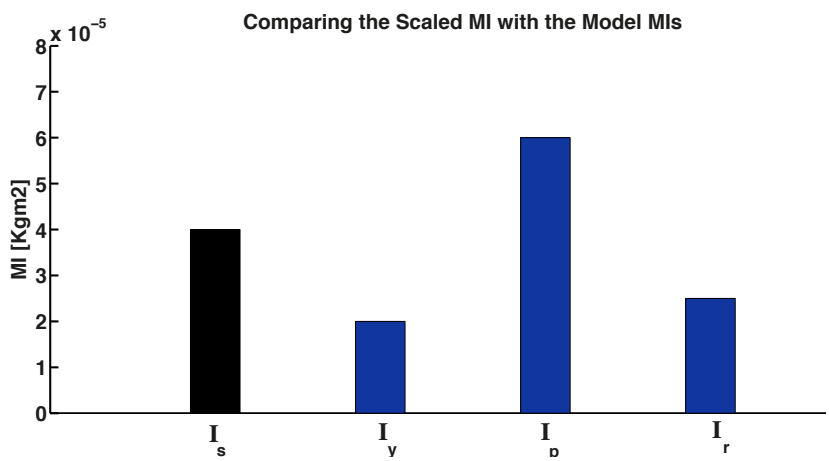

Figure 6.10: Comparison of model's MI and the scaled MI of the real eye

to the globe through the dyneema cables, their effective inertia at the centre of the globe can be expressed by Equation 6.1. Here, I_{re} is the effective motor inertia at the globe, I_r is the actual motor inertia and R_g and R_p are respectively the globe and the motor pulley radii.

$$I_{re} = I_r(\frac{R_g}{R_p})^2 \tag{6.1}$$

Therefore, the $4 \times 10^{-6}\ Kgm^2$ inertia of the motor rotor[3] is scaled to its equivalent $8 \times 10^{-5}\ Kgm^2$ inertia at the globe centre.

The results of including the motor inertias are presented by the bar graph in Figure 6.11. The addition of the motor inertias imposes a 1 order of magnitude difference between the scaled biological inertia and the robot's inertias. Nevertheless, Robinson [52] has shown that inertial forces in the biological eye remain negligible even when they are increased by 2 orders of magnitude. Thus, the 1 or-

[3]Value taken from the motor data sheet

der of magnitude difference between the MI of the robot and the scaled biological value is still sufficient for considering the inertial forces as negligible compared to the passive and active forces. Furthermore, upon examining Equation 6.1, it

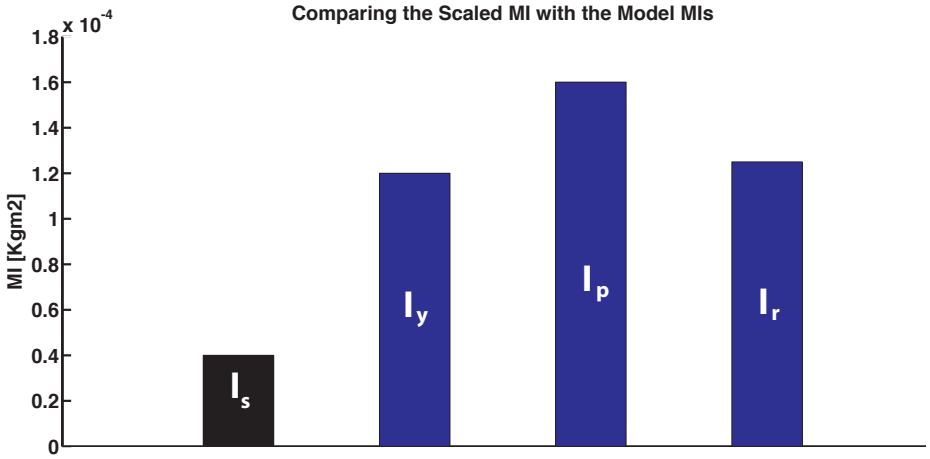

Figure 6.11: Comparison of model's MI and the scaled MI of the real eye, including the motor's inertias

is apparent that the effective MIs of the motors can be considerably reduced by increasing the radius of the motor pulleys. However, this must be done while accounting for the maximum torque required from the motors and ensuring that changing the pulley radius will not compromise this requirement.

Speed Evaluation

Being able to achieve speeds comparable to the real eye is another important quality that the eye robot must posess if it is to function as a testbed for implementing real eye movements; this is particularly important for saccades, the fastest eye

movement. When considering a saccade, we can quantify the speed of the response with its rise time[4] and peak velocity. The eye robot must be capable of reaching peak velocities achieved by real saccadic movements. However, these peak velocities must be appropriately scaled using $\Pi_\omega = \omega\sqrt{\frac{I}{K}}$, the angular speed Π group developed in Section 4.1. Therefore, given a biological peak velocity, ω_{maxB}, the equivalent robot peak velocity, ω_{maxR} is defined by:

$$\omega_{maxR} = \omega_{maxB}\sqrt{\frac{K_R I_B}{K_B I_R}}$$

which scales down the model's peak velocity, as a function of the ratio of the biological inertia to the robot's inertia.

In Figure 6.12, responses of the eye robot to 5 *Deg* and 15 *Deg* step commands in yaw and pitch are compared with 5 *Deg* and 15 *Deg* human saccade recordings in yaw and pitch.

Table 6.3: Rise times of robot's and biological saccade responses

	Yaw5 *Deg*	Yaw15 *Deg*	Pitch5 *Deg*	Pitch15 *Deg*
Real Eye $[ms]$	13	23	18	23
Robot Eye $[ms]$	23	38	31	35

The biological data, shown as the dashed line, are recorded using a 2D eye tracking system, which uses an infrared camera to track the pupil. The robot data plotted here, are not scaled by the Π variables; nonetheless, the robot reaches peak velocities as high as the biological values, indicating that it is certainly ca-

[4]Here rise time is defined as the time required to reach 63% of the steady state value.

pable of achieving comparable scaled speeds. Furthermore, the rise times of these responses are reported in Table 6.3. Once again, despite the fact that the robot values have not been scaled appropriately, they are very close to the saccadic rise times. Thus, considering speed requirements, the presented eye robot provides a suitable testbed for examining oculomotor behaviors.

Although the eye robot is capable of reaching biologically comparable peak velocities, its velocity profile starts to increase at a much lower rate in comparison with the biological response. This steep slope in the real eye's velocity profile, suggests that the biological controller turns on to a maximum rate before cutting out once the target position is reached. This is a known characteristic of the saccadic *Pulse-Step* controller. Another indication of existence of such saccadic controller is the system's response to a force step input. When a step force is applied to the biological globe, it rotates with a time constant of 250 *ms* [52]. However, as illustrated in Figure 6.12, typical saccades have markedly shorter durations. This indicates that the eye is not normally driven with a step input force, rather it is driven to its desired orientation, with a pulse of maximum torque and a step input is only applied to keep the globe at this desired orientation. Consequently, it appears that the motor size is sufficient to allow the eye robot to achieve peak velocities comparable to the real eye, and that the limitations in achieving comparable biological tracking rates are limitations of the current controller rather than the intrinsic capabilities of the hardware.

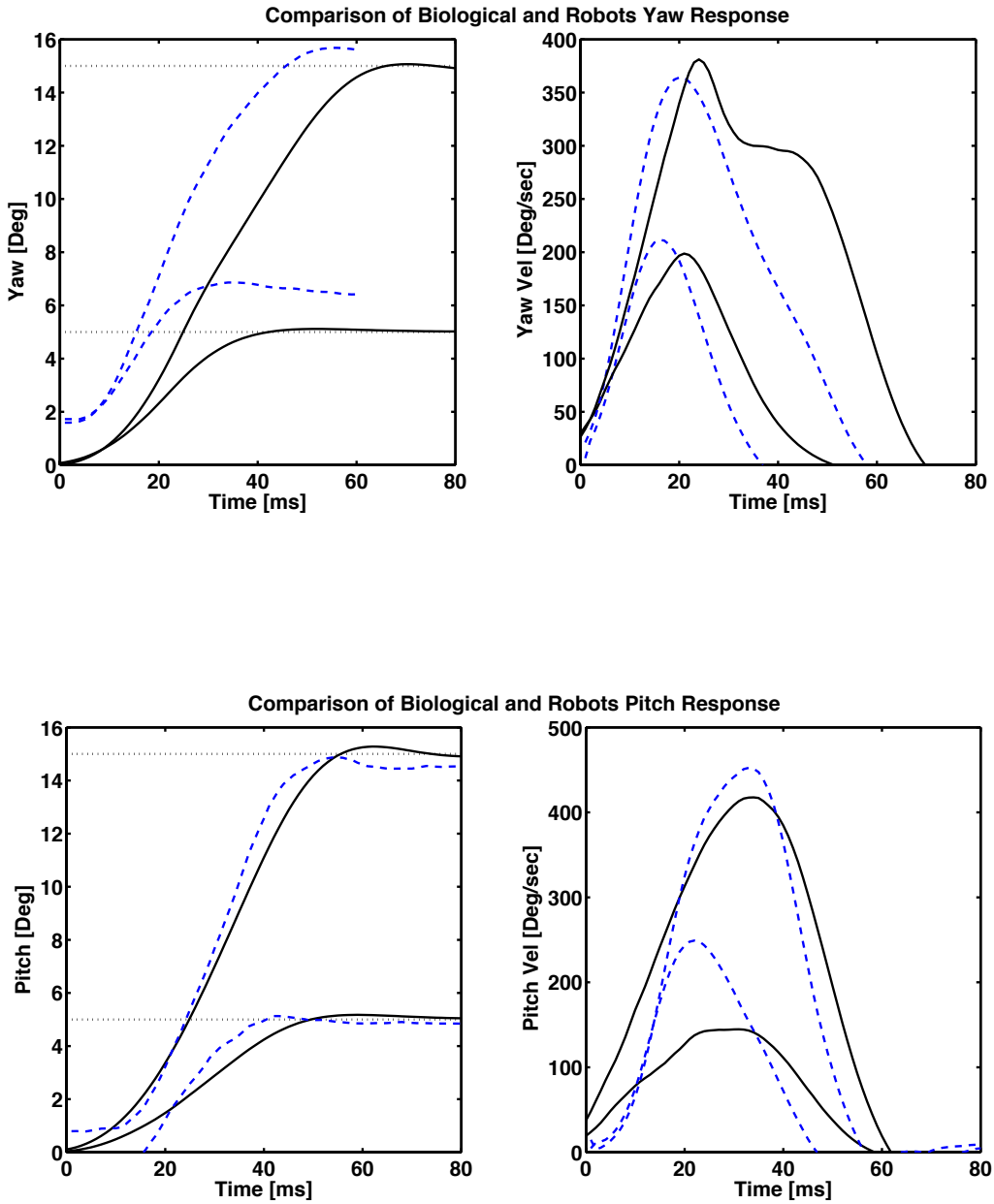

Figure 6.12: Comparison of the eye robot responses, to step inputs, with human saccade recordings

Chapter 7

Conclusion

7.1 Progress Assessment

The objective of this research is to create a novel physical model of the human eye to be used as a platform for testing theories regarding oculomotor control as well as providing insight on how to control tendon driven robots.

The design of this model was divided into two parts: the structural (Chapter 4) and the mechatronics (Chapter 5) design. In Chapter 3, it was shown that to create an eye model that mimics the geometric and anatomic properties critical in the static and dynamic performance of the human eye, we must have an appropriately scaled three dimensional model of the biological eye that represents the agonist/antagonist EOMs accurately.

Subsequently, Chapter 4 provided solutions for incorporating these requirements in the design of the eye robot. Using Π dimensional analysis, the ocu-

lar plant was expressed as a function of four non-dimensional variables called Π groups. These groups were used to scale biological quantities such as torque, stiffness, velocity and acceleration to appropriate values for the scaled up eye model. The activation of the EOMs are represented by 6 DC motors, which drive the globe through cables that represent the ocular tendons. Furthermore, the insertion and anchoring locations of the tendons are chosen to ensure that the cables are routed in the correct angular position. Finally, a custom made gimbal structure provides a low friction support, which allows the eye robot's globe to rotate in three directions. Considering that yaw is the most frequent eye rotation direction, it is important to ensure that the velocity of the globe is maximized in this direction, which means reducing the globe's inertia in yaw. Furthermore, given that a gimbal forms a serial kinematic chain, distal axes of rotations have smaller inertia than the proximal ones. Therefore, an important aspect of gimbal design is to implement a sequence of rotation where yaw would be the the inner most gimbal rotation. The presented gimbal implements pitch, followed by roll, with yaw as the final rotation and the unique design and placement of the gimbal elements is key to achieving this sequence.

In Chapter 5, a control algorithm was designed to evaluate the kinematic and dynamic performance of the eye robot. To develop the presented controller, the eye robot was regarded as a redundant tendon driven robot, to be driven to a desired position. The globe's 3D orientation was subsequently controlled by projecting this 3D quantity to the 6D space of the tendon lengths using the jacobian of the eye system, which was developed based on the system's kinematics.

Finally, in Chapter 6, we assessed the acceptability of the eye system for emulating oculomotor behaviors by verifying 3 main characteristics of the eye robot. Specifically, it was shown that the eye robot is capable of achieving satisfactory tracking accuracy in the 3 principle directions of rotation. However, due to high motor static frictions, the model does not have the same performance for 2D trajectories. By comparing the robot's responses, to commanded step inputs, with human saccade responses, it is evident that the robot is capable of reaching biologically comparable speeds. Furthermore, I demonstrated that the MIs of the robot are sufficiently small in comparison with the scaled biological inertia and thus, similar to the oculomotor system, the inertial forces in our eye model are negligible.

7.2 Research Implications

The main contribution of this thesis is a novel 3 dimensional tendon driven model of the human eye and a corresponding controller for driving this redundant system. This study has focused on designing a geometrically accurate model, which can be used for several purposes. Most notably, it incorporates the aspects of the anatomy that are functionally crucial for using this model as testbed for implementing oculomotor control theories. This physical model can also be used in conjunction with simulated models of the eye to understand diseases or injuries affecting vision and find treatments for these conditions. In addition, using this testbed to explore biological visual systems could give insight in how a biologically inspired vision system could be effective in real world applications.

7.3 Future Work

A major limitation of the current design is the frictional forces that are present in the system. Most notable are the friction forces introduced between the cables and the globe's surface due to the rough finish on the globe. This drawback may be resolved by applying a smoother globe finish, which is left as future work for following versions of the model.

Another significant source of friction is the static friction in the motors. These frictional losses are attributable to the rotational bearings as well as the graphite commutator; their overall value is determined by the input current required to run the motor under no-load conditions. For the Maxon motor being used here, this value is reported as 58 mA or 1.4 mNm. This could potentially lead to complications when implementing a biological controller, especially when slow tracking motions are involved. A brushless DC motor could be used to reduce the frictional losses.

Furthermore, as discussed previously, there are two major steps for transforming theories regarding various computational neuroscientific models into facts:

1. Building a geometrically accurate physical model

2. Developing a biologically inspired controller

The main focus of this research is the creation of the physical model and thus the development of a biologically inspired controller is left as future work.

Bibliography

[1] L. Aryananda and J. Weber. Mertz: A quest for a robust and scalable active vision humanoid head robot. In *Proceedings of IEEE/RAS Int. Conf. on Humanoid Robots*, pages 513–532. Citeseer, 2004. → pages 5

[2] T. Asfour, K. Welke, P. Azad, A. Ude, and R. Dillmann. The karlsruhe humanoid head. In *Humanoid Robots, 2008. Humanoids 2008. 8th IEEE-RAS International Conference on*, pages 447–453. IEEE, 2008. → pages 6

[3] C. Atkeson, J. Hale, F. Pollick, M. Riley, S. Kotosaka, S. Schaul, T. Shibata, G. Tevatia, A. Ude, S. Vijayakumar, et al. Using humanoid robots to study human behavior. *Intelligent Systems and their Applications, IEEE*, 15(4): 46–56, 2000. → pages 5

[4] W. Atsma. *Inference of central nervous system input and its complexity for interactive arm movement*. PhD thesis, The University of British Columbia, 2006. → pages 95

[5] A. Bahill, M. Clark, and L. Stark. The main sequence, a tool for studying human eye movements. *Mathematical Biosciences*, 24(3-4):191–204, 1975. → pages 16, 23

[6] W. Becker. The neurobiology of saccadic eye movements. metrics. *Reviews of oculomotor research*, 3:13, 1989. → pages 23

[7] R. Beira, M. Lopes, M. Praga, J. Santos-Victor, A. Bernardino, G. Metta, F. Becchi, and R. Saltarén. Design of the robot-cub (icub) head. In *Robotics and Automation, 2006. ICRA 2006. Proceedings 2006 IEEE International Conference on*, pages 94–100. IEEE, 2006. → pages 5, 6

[8] D. Biamino, G. Cannata, M. Maggiali, and A. Piazza. Mac-eye: A tendon driven fully embedded robot eye. In *Humanoid Robots, 2005 5th IEEE-RAS International Conference on*, pages 62–67. IEEE, 2005. → pages 7, 35, 82

[9] W. Boger III. Binocular vision and ocular motility: Theory and management of strabismus. *Archives of Ophthalmology*, 104(3):339, 1986. → pages 3

[10] L. Brand. The pi theorem of dimensional analysis. *Archive for Rational Mechanics and Analysis*, 1(1):35–45, 1957. → pages 25

[11] R. W. Brockett. Robotic manipulators and the product of exponentials formula. *Mathematical Theory of Networks and Systems*, pages 120–129, 1984. → pages 81

[12] E. Buckingham. On physically similar systems; illustrations of the use of dimensional equations. *Physical Review*, 4(4):345–376, 1914. → pages 25

[13] D. Caldwell, G. Medrano-Cerda, and M. Goodwin. Characteristics and adaptive control of pneumatic muscle actuators for a robotic elbow. In *Robotics and Automation, 1994. Proceedings., 1994 IEEE International Conference on*, pages 3558–3563. IEEE, 1994. → pages 31

[14] P. Carbonell, Z. Jiang, and D. Repperger. Nonlinear control of a pneumatic muscle actuator: backstepping vs. sliding-mode. In *Control Applications, 2001.(CCA'01). Proceedings of the 2001 IEEE International Conference on*, pages 167–172. IEEE, 2001. → pages 31

[15] J. Demer. Ocular kinematics, vergence, and orbital mechanics. *Strabismus*, 11(1):49–57, 2003. ISSN 0927-3972. → pages 19

[16] J. Demer. Evidence supporting extraocular muscle pulleys: refuting the platygean view of extraocular muscle mechanics. *Journal of Pediatric Ophthalmology & Strabismus*, 43(5), 2006. ISSN 0191-3913. → pages 5, 19

[17] J. Demer, S. Oh, and V. Poukens. Evidence for active control of rectus extraocular muscle pulleys. *Investigative ophthalmology & visual science*, 41(6):1280, 2000. → pages 19, 32

[18] J. Findlay, I. Gilchrist, and O. U. Press. *Active vision: The psychology of looking and seeing*, volume 2. Oxford University Press Oxford,, UK, 2003. → pages 1

[19] G. Fry and W. Hill. The center of rotation of the eye. *American journal of optometry and archives of American Academy of Optometry*, 39:581, 1962. → pages 21

[20] A. Fuchs. Saccadic and smooth pursuit eye movements in the monkey. *The Journal of Physiology*, 191(3):609, 1967. → pages 23

[21] E. C. C. G. K. von Noorden. *Binocular Vision and Ocular Motility:Theory and Management of Strabismus*. Mosby, 2001. → pages 14

[22] T. Haslwanter. Mathematics of three-dimensional eye rotations. *Vision Research*, 35(12):1727–1739, 1995. → pages ix, 42, 121

[23] E. Hering. The theory of binocular vision, 1868 ed. translated by b. bridgeman and l. stark, 1977. → pages 14

[24] S. Jacobsen, H. Ko, E. Iversen, and C. Davis. Control strategies for tendon-driven manipulators. *Control Systems Magazine, IEEE*, 10(2):23–28, 1990. → pages 85

[25] R. Jampel and D. Shi. Evidence against mobile pulleys on the rectus muscles and inferior oblique muscle: central nervous system controls ocular kinematics. *Journal of pediatric ophthalmology and strabismus*, 43(5):289–295, 2006. ISSN 0191-3913. → pages 19

[26] A. Koene and C. Erkelens. Properties of 3d rotations and their relation to eye movement control. *Biological cybernetics*, 90(6):410–417, 2004. → pages 19, 32

[27] L. Koornneef. The first results of a new anatomical method of approach to the human orbit following a clinical enquiry. *Acta morphologica Neerlando-Scandinavica*, 12(4):259, 1974. → pages 52

[28] H. Kozima and H. Yano. A robot that learns to communicate with human caregivers. In *Proceedings of the First International Workshop on Epigenetic Robotics*, pages 47–52. Citeseer, 2001. → pages 5

[29] M. Land, N. Mennie, J. Rusted, et al. The roles of vision and eye movements in the control of activities of daily living. *PERCEPTION-LONDON-*, 28(11): 1311–1328, 1999. → pages 1

[30] G. Lang. *Ophthalmology: a short textbook*. Thieme, 2000. → pages 3

[31] R. Leigh and C. Kennard. Using saccades as a research tool in the clinical neurosciences. *Brain*, 127(3):460, 2004. → pages vii, 22, 23

[32] R. Leigh and D. Zee. *The neurology of eye movements*. Oxford Univ Pr, 1999. → pages 5

[33] R. Leigh and D. Zee. *The neurology of eye movements*. Number 55. Oxford Univ Pr, 1999. → pages 15, 16, 23

[34] R. Leigh and D. Zee. *The neurology of eye movements*. Number 55. Oxford Univ Pr, 1999. → pages 11

[35] A. Lenz, S. Anderson, A. Pipe, C. Melhuish, P. Dean, and J. Porrill. Cerebellar-inspired adaptive control of a robot eye actuated by pneumatic artificial muscles. *Systems, Man, and Cybernetics, Part B: Cybernetics, IEEE Transactions on*, 39(6):1420–1433, 2009. → pages 8

[36] Y. Matsuoka, P. Afshar, and M. Oh. On the design of robotic hands for brain-machine interface. *Neurosurg Focus*, 20(5):1–9, 2006. → pages 2

[37] J. McClung, B. Allman, D. Dimitrova, and S. Goldberg. Extraocular Connective Tissues: A Role in Human Eye Movements? IOVS January 2006 47: 202-205; doi: 10.1167/iovs. 05-0860. → pages 19

[38] A. Mehmood, B. Camescasse, F. Ouezdou, and G. Cheng. Simulation and design of 3-dof eye mechanism using listing's law. In *Humanoid Robots, 2008. Humanoids 2008. 8th IEEE-RAS International Conference on*, pages 429–434. IEEE. → pages 8, 9

[39] J. Miller. Functional anatomy of normal human rectus muscles. *Vision research*, 29(2):223–240, 1989. → pages 52

[40] J. Miller and D. Robins. Extraocular muscle forces in alert monkey. *Vision research*, 32(6):1099–1113, 1992. → pages 74

[41] H. Misslisch and D. Tweed. Neural and mechanical factors in eye control. *Journal of neurophysiology*, 86(4):1877, 2001. ISSN 0022-3077. → pages 19

[42] H. Miwa, T. Okuchi, H. Takanobu, and A. Takanishi. Development of a new human-like head robot we-4. In *Intelligent Robots and Systems, 2002. IEEE/RSJ International Conference on*, volume 3, pages 2443–2448. IEEE, 2002. → pages 5, 6

[43] R. Pedrosa. Design and construction of a tendon-driven eye model, 2008. → pages 39, 117

[44] C. Pfeiffer, K. DeLaurentis, and C. Mavroidis. Shape memory alloy actuated robot prostheses: initial experiments. In *Robotics and Automation, 1999. Proceedings. 1999 IEEE International Conference on*, volume 3, pages 2385–2391. IEEE, 1999. → pages 31

[45] D. Pongas, F. Guenter, A. Guignard, and A. Billard. Development of a miniature pair of eyes with camera for the humanoid robot robota. In *IEEE/APS Intl Conference on Humanoid Robots*. Citeseer, 2004. → pages 5, 6

[46] J. Porter and R. Baker. Muscles of a different'color'. *Neurology*, 46(1):30, 1996. → pages 8, 31

[47] J. Porter, R. Baker, R. Ragusa, and J. Brueckner. Extraocular muscles: Basic and clinical aspects of structure and function*. *Survey of ophthalmology*, 39 (6):451–484, 1995. → pages 13

[48] C. Quaia and L. Optican. Commutative saccadic generator is sufficient to control a 3-D ocular plant with pulleys. *Journal of neurophysiology*, 79(6): 3197, 1998. ISSN 0022-3077. → pages 19, 31, 32

[49] C. Quaia and L. Optican. Dynamic eye plant models and the control of eye movements. *Strabismus*, 11(1):17–31, 2003. ISSN 0927-3972. → pages 7, 20, 30, 34, 35

[50] T. Raphan. Modeling control of eye orientation in three dimensions. I. Role of muscle pulleys in determining saccadic trajectory. *Journal of neurophysiology*, 79(5):2653, 1998. ISSN 0022-3077. → pages 19, 32

[51] L. Remington. *Clinical anatomy of the visual system*. Elsevier, 2005. → pages 13

[52] D. Robinson. The mechanics of human saccadic eye movement. *The Journal of Physiology*, 174(2):245, 1964. → pages 16, 23, 74, 99, 101, 104

[53] D. Robinson. Models of the mechanics of eye movements. *Models of oculomotor behavior and control*, pages 21–41, 1981. → pages 24

[54] C. Schnabolk and T. Raphan. Modeling three-dimensional velocity-to-position transformation in oculomotor control. *Journal of neurophysiology*, 71(2):623, 1994. → pages 31, 32

[55] I. Stavness, A. Hannam, J. Lloyd, and S. Fels. Dynamic modeling of human jaw and laryngeal biomechanics. → pages 2

[56] M. Thurtell, M. Kunin, and T. Raphan. Role of muscle pulleys in producing eye position-dependence in the angular vestibuloocular reflex: a model-based study. *Journal of neurophysiology*, 84(2):639, 2000. → pages 19, 32

[57] B. Tondu and P. Lopez. Modeling and control of mckibben artificial muscle robot actuators. *Control Systems Magazine, IEEE*, 20(2):15–38, 2000. → pages 31

[58] D. Tweed, H. Misslisch, and M. Fetter. Testing models of the oculomotor velocity-to-position transformation. *Journal of neurophysiology*, 72(3): 1425, 1994. → pages 31

[59] M. Vande Weghe, M. Rogers, M. Weissert, and Y. Matsuoka. The act hand: design of the skeletal structure. In *Robotics and Automation, 2004. Proceedings. ICRA'04. 2004 IEEE International Conference on*, volume 4, pages 3375–3379. IEEE, 2004. → pages 9

[60] G. Von Noorden. Summary of the gross anatomy of the extraocular muscles. *Binocular Vision and Ocular Motility. 5th ed. St Louis, MO: Mosby-Yearbook Inc*, pages 41–51, 1996. → pages vii, 34, 35, 36

[61] G. Von Noorden. Summary of the gross anatomy of the extraocular muscles. *Binocular Vision and Ocular Motility. 5th ed. St Louis, MO: Mosby-Yearbook Inc*, pages 41–51, 1996. → pages 13

[62] G. Von Noorden and E. Campos. Binocular vision and ocular motility: theory and management of strabismus. *Mosby, St. Louis*, 62:38–51, 2002. → pages 13

[63] X. Wang, Y. Zhang, X. Fu, and G. Xiang. Design and kinematic analysis of a novel humanoid robot eye using pneumatic artificial muscles. *Journal of Bionic Engineering*, 5(3):264–270, 2008. → pages 7, 35

[64] Q. Wei and D. Adviser-Pai. *Biomechanical modeling and simulation of human eye movement*. Rutgers University, 2010. → pages 34

[65] Q. Wei, S. Sueda, and D. K. Pai. Physically-based modeling and simulation of extraocular muscles. *Progress in Biophysics & Molecular Biology*, 103 (2-3):273–283, December 2010. → pages 8, 12

[66] K. Wright. Anatomy and physiology of eye movements. *Handbook of Pediatric Strabismus and Amblyopia*, pages 24–69, 2006. → pages 15

[67] A. Yarbus. Eye movements and vision. 1967. *New York*. → pages 1

[68] X. Zhang and M. Lee. A developmental robot vision system. In *Systems, Man and Cybernetics, 2006. SMC'06. IEEE International Conference on*, volume 3, pages 2024–2029. IEEE. → pages 5, 6

[69] B. Zuber. *Models of oculomotor behavior and control*. CRC Press, 1981. → pages 24, 72, 73

Appendix A

Design Iteration

A.1 Considered Solutions

The initial approach for the design of an optimum globe support structure was to rest the globe on ball terminated set screw (BTSC) A.1. Eight of these supporting set screws are threaded into four arc shaped holders which support the globe along two of its diameters making a 45° angle with the vertical line through the centre of the globe. Figure A.2 illustrates a prototype that was built based on this concept by a previous colleague [43].

Initially this appeared as an appealing solution primarily because it was a reasonably simple design and it presented the accessible and open concept structure necessary for facilitating experimentation and modifications. Nevertheless, despite this open structure, the clearance of the cables proved to be a difficult problem to solve. Specifically, it was very challenging to find an optimal location for

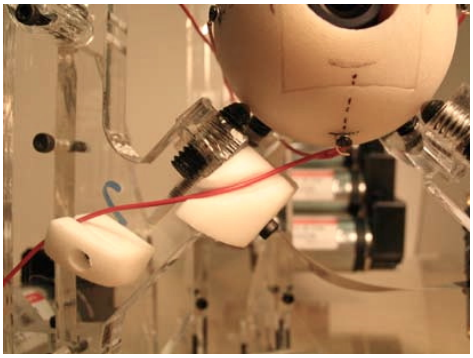

Figure A.1: Ball terminated set screws used to support the globe

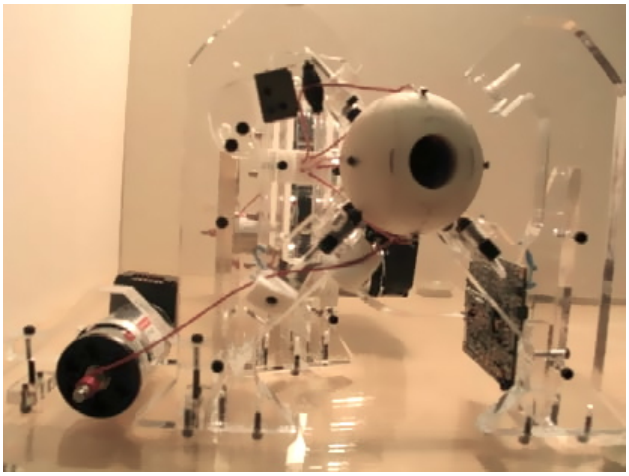

Figure A.2: Globe support structure design based on the ball terminated set screws

the BTSCs, as to avoid interference with the IPs throughout the entire range of motion. Moreover, the ball bearing arrangement had an undesirable high friction, which would add uncertainties to the system and complicate the control process.

To improve on the ball bearing support structure we began exploring alternative conceptual designs inspired by the biological orbital support. In an attempt to

mimic the ligament connections of the ocular plant the elastic stalk support design was considered. Essentially as illustrated in A.3, the globe is grounded through spring elements that are fixed to the ground at one end and to the globe at the other end. In addition to having a close resemblance to the orbital support, the elastic stalks also serve as built in passive stiffness. Therefore by carefully selecting the properties of the the spring elements we could have a physical representation of the ocular passive elements and reduce the complexity of the control algorithm.

However despite their advantages, the elastic stalks are not sufficient to keep the globe from translating. This is because the design is only a partial representation of the biological orbital support and consequently it lacks certain characteristic elements that account for this translating problem in the biological version. Specifically, the elastic stalk design lacks the equivalent of the periorbital fat and tenon's capsule which are responsible for limiting the globe's motion to a purely rotational one. Furthermore, this design shares a similar drawback with the ball bearing structure. Namely once again an optimal location of the elastic stalk attachments is challenging to find without creating interference with the cables. Given this common difficulty it was concluded that an effective design must minimize its contact points with the surface of the globe.

Considering the limitations of the mentioned design concepts, we ultimately decided on supporting the globe in a gimbal system. A gimbal is any support structure that can pivot about an axis, but usually it is defined as a set of three pivoting supports whose axis of rotations are orthogonal to one another. As illustrated in Figure A.4, the gimbal parts are linked to each other and so as one part

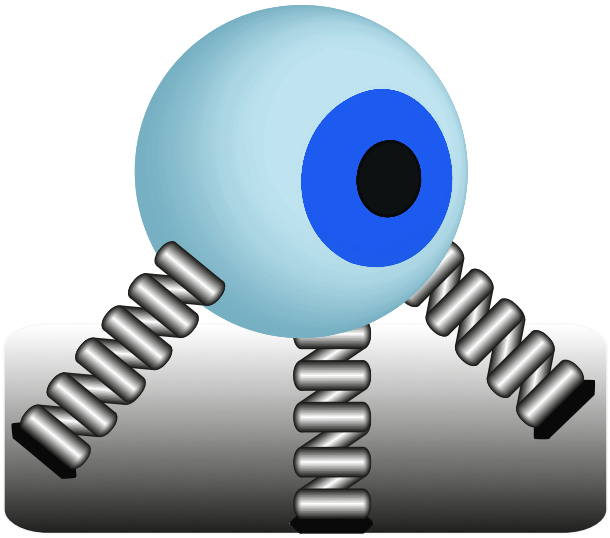

Figure A.3: Elastic stalk support concept

rotates its rotation is passed on to the other two parts. Consequently any object, such as the globe, that is fastened to the most inner rotating element could be oriented in any direction by rotating the gimbal parts. Additionally, this orientation is characterized by a moving reference frame whose order of hierarchy is determined by the linking sequence of the gimbal parts. For instance suppose that the globe is mounted onto the shaft of the gimbal in Figure A.4, then its location is described by first a vertical rotation, followed by a horizontal rotation and finally a torsional rotation about the line of sight. Nevertheless this sequence of rotation is not explicit and may be chosen according to the preferred order of eye movement.

Although the design of the gimbal structure is much more involved, it has a number of advantages compared to the ball terminated set screw as well as the

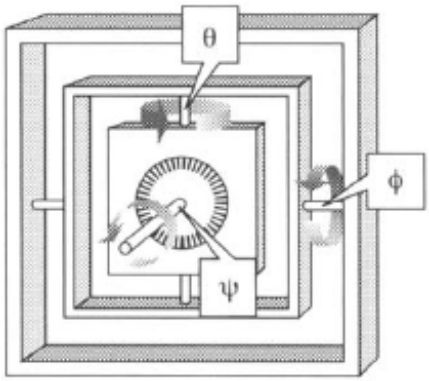

Figure A.4: Conceptual gimbal support structure [22]

elastic stalk design. The gimbal design could be optimized to minimize the contact points of the supporting structure with the globe's surface. This would considerably reduce the complications regarding cables interference. Moreover, given that each gimbal part rotates about a single axis, it becomes much more trivial to find a low friction solution for the motion of each part (example, bearings), ultimately leading to a low friction support structure. Finally using a gimbal system enables the potential of measuring the three individual rotations that make up the final orientation of the globe. This data would be valuable for developing a control algorithm.

A.2 Gimbal Design

The following sections explain the design iterations that were carried out in order to arrive at a suitable shape for the gimbal support structure.

A. General Gimbal Shape

It is extremely challenging to use a theoretical approach for finding a suitable gimbal shape that would provide cable clearance through out the globe's entire range of motion. Consequently, the general shape of the gimbal was chosen using an iterative design process, where physical prototypes were built based on conceptual designs. These elementary prototypes had the unique purpose of evaluating the shape and kinematic characteristics of a given gimbal design. Therefor, they were not concerned with perfecting the details of the mechanical design, including the final size of the globe being used.

Most of the initial prototypes were built from readily available and easily manufacturable materials. For instance various shapes of the gimbal elements were cut from plywood, while styrofoam and plastic spheres were used to represent the globe. Screws fastened on one end, and rotating freely in a through hole at the other end, represented rotational joints. Furthermore, in order to get an accurate understanding of whether a given gimbal shape was suitable for routing the tendons, the cable's insertion points were scaled based on the diameter of the globe being used and tendons were routed to represent the same configuration as the biological tendons.

Figure A.5 shows the prototype of the first gimbal design. This gimbal's sequence of rotation is given by pitch, yaw and roll. Much of the design decisions of this initial prototype were motivated by the aim of creating a system that minimized the gimbal attachments to the globe while ensuring tendon clearance. Consequently, the globe cantilevers off of the inner most element of the gimbal,

therefore reducing the globe-gimbal attachments to 1 point. This point is located at the equivalent location of the optic nerve in the real eye where there are no tendons present and the irregular shape of the second gimbal element and the relatively large ring, provide an excellent platform for routing the cables without any interference with the gimbal parts. However, these beneficially large and irregular shaped elements lead to an unacceptable increase in the MI of the gimbal elements. Therefore, to account for this significant drawback the gimbal parts must be reduced in size and weight while still ensuring cables clearance. Most importantly, the gimbal in Figure A.5 does not have yaw as its inner most rotation. This was a challenging requirement that took a few design iterations to achieve.

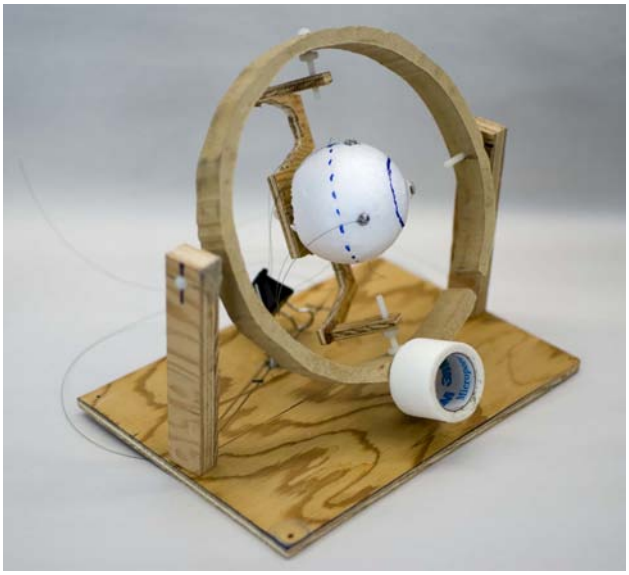

Figure A.5: Prototype1: the first design for the gimbal's general shape

The second iteration of the design, illustrated in Figure A.6, focused on solving the simpler drawback of prototype1, reducing the MI of the gimbal parts while

keeping the routing path of the cables clear. Consequently, this second iteration has the same sequence of rotation as prototype1 but with much smaller MI. This is achieved through reducing the mass and moment arm of the gimbal elements by having lightweight circular shaped elements and bringing them closer to the outer circumference of the sphere. The semi and $3/4$ circular shapes of this gimbal's elements were chosen to reduce weight while ensuring a clear routing path for the oblique cables. In fact, although prototype2 is about half the size of prototype1 ($D_{max1} = 150\ mm\ vs.\ D_{max2} = 70\ mm$), it provides an interference free path for routing all of the cables.

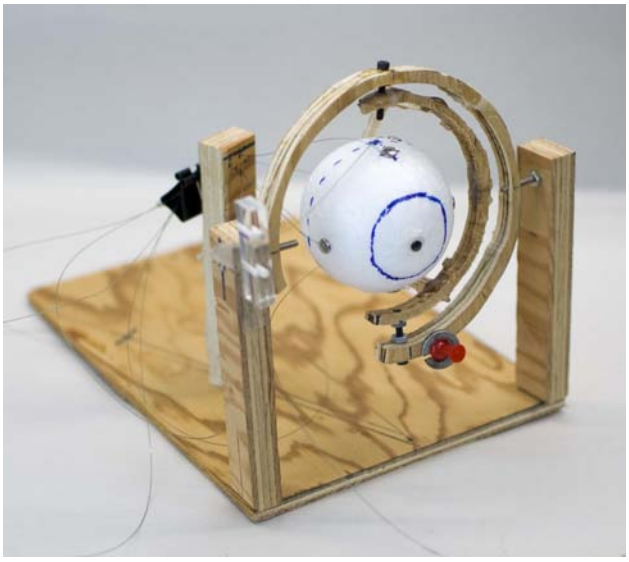

Figure A.6: Prototype2: the second design for the gimbal's general shape

Despite the improvements of prototype2, a third iteration of the gimbal's general shape design had to be carried out in order to set yaw as the inner most rotation of the gimbal support structure. As a result, prototype3 was entirely driven by this

inclination, while keeping the previously determined requirements in mind. Figure A.7 shows the wooden version of prototype3. This gimbal implements a pitch, roll, yaw rotation sequence, which is achieved by the unique shape and placement of the gimbal elements. Most notably is the placement of the C-bracket, as labeled in A.8, that bears the rotational joints of yaw and roll. The globe is custom

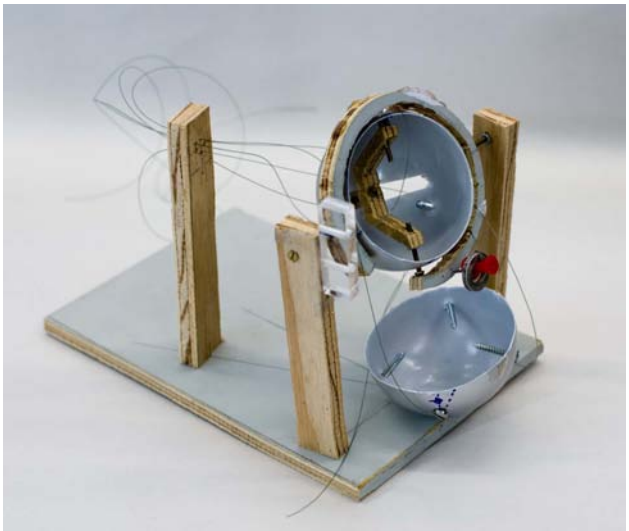

Figure A.7: Prototype3: the third design for the gimbal's general shape

designed to include the yaw shafts, Figure A.8. These shafts are fastened to the globe and rotate freely in the yaw joints located on the top and bottom part of the C-bracket. Therefore, during yaw rotations the C-bracket stays still and the globe must have a posterior slot (labeled *"trace slot"* in A.8) to accommodate the C-bracket's extension through it's back. As in the previous prototypes, roll is handled by a single joint, located at the centre of the C-bracket. The shaft for this rotation is fastened to the back plate of the outer ring. Therefore, during roll

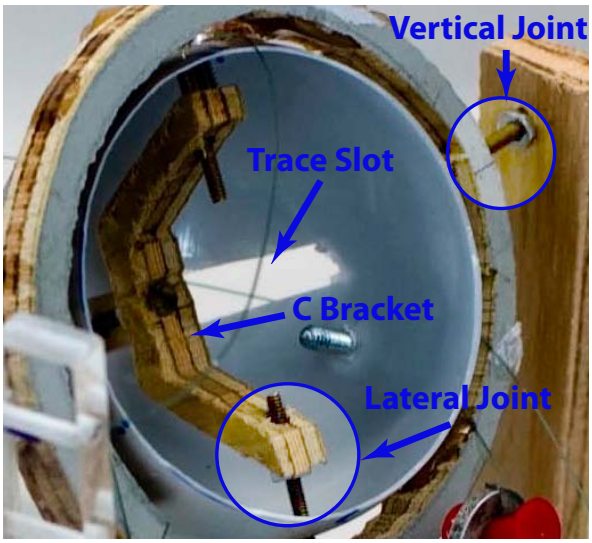

Figure A.8: The mechanism used for the lateral joint in Prototype3

the globe's MI is increased by that of the C-bracket that moves with it. Finally, pitch in this gimbal is achieved by the rotation of the two shafts, fixed along the centre line of the outer ring, through the joints in the support stands, Figure A.8. Given this arrangement, the globe has the largest added MI during pitch since all the gimbal elements (the outer ring, its back plate and the C-bracket) are moving with the globe. The added inertias to roll and pitch are minimized by placing the C-bracket inside the globe, which reduces the moment arm of this element immensely. Furthermore, we have brought the outer ring as close as possible to the surface of the globe, which once again reduces the added inertia by reducing the moment arm. In addition, the gimbal element's mass were optimized by careful material selection and shape design to further reduce the added MI.

B. Rapid Prototype Model of Prototype3

The general gimbal shape achieved by prototype3 satisfies the major design requirements set originally, namely:

- Placing the most frequent eye movement, yaw, as the inner most rotation
- Minimizing the gimbal element's MI by reducing the mass and moment arm
- Decreasing the gimbal/globe contact to a single point
- Providing a clear routing path for all the cables

Consequently, to further investigate the strengths and weaknesses of this design a more precise version of prototype3 was built. The main motivation for building this model was to implement and examine the detailed mechanical design that had been neglected in prototype3. These include joint friction, adequate joint constraints, size and material properties.

Considering the complicated nature of the gimbal parts I used rapid prototyping to construct them. This "additive layer manufacturing" provides a simple process for fabricating complex shaped parts that would otherwise be very difficult to produce using traditional methods such as machining. However, choosing rapid prototyping as the manufacturing technique limits the material selection to the list of plastics suitable for this process. Amongst these I chose polycarbonate, one of the strongest available materials with a tensile strength of 57 MPa. Figure A.9 illustrates the final results, various parts of the model are labeled.

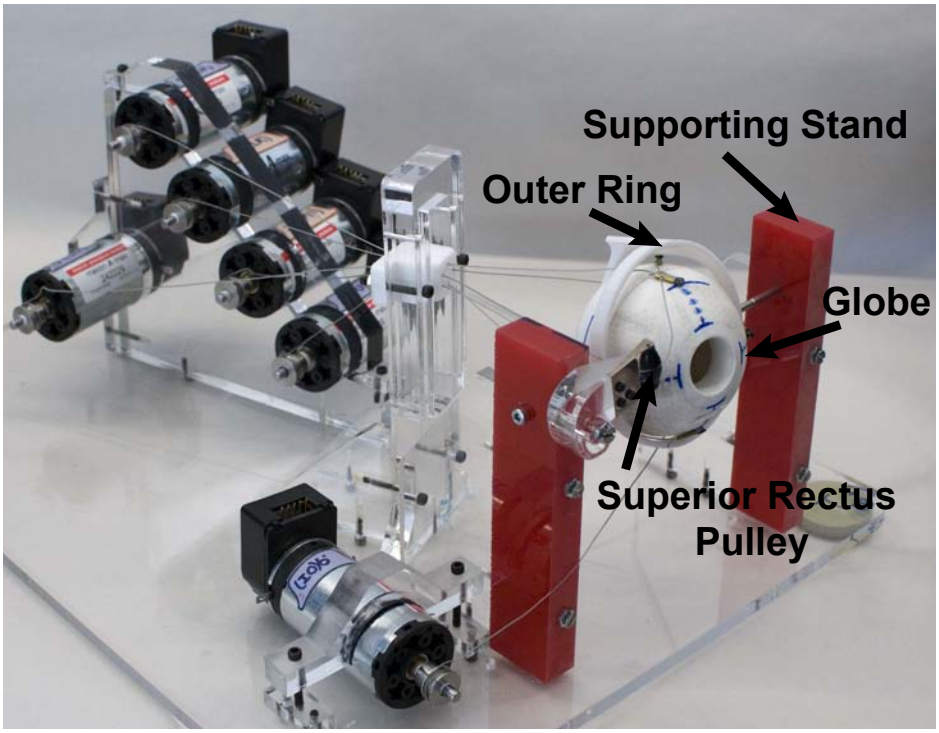

Figure A.9: First rapid prototype of the eye robot

The overall dimension of the model was selected based on the lowest possible globe size. The globe's 46 *mm* inner diameter was restrained by the size of the available camera, 20 $mm \times 30$ $mm \times 23$ mm. Furthermore, to accommodate the C-bracket the globe is parted longitudinally into two components that are friction fitted together, illustrated in Figure A.10. In this model, the yaw shafts are combined into one continuous 2 *mm* stainless steel precision shaft which is fixed in the through hole down the length of the C-bracket, Figure A.10. This arrangement of the yaw rotation shaft acts as a reinforcement in the horizontal direction when the globe is pulled back by the activated cables. Table A.1 summarizes the details of

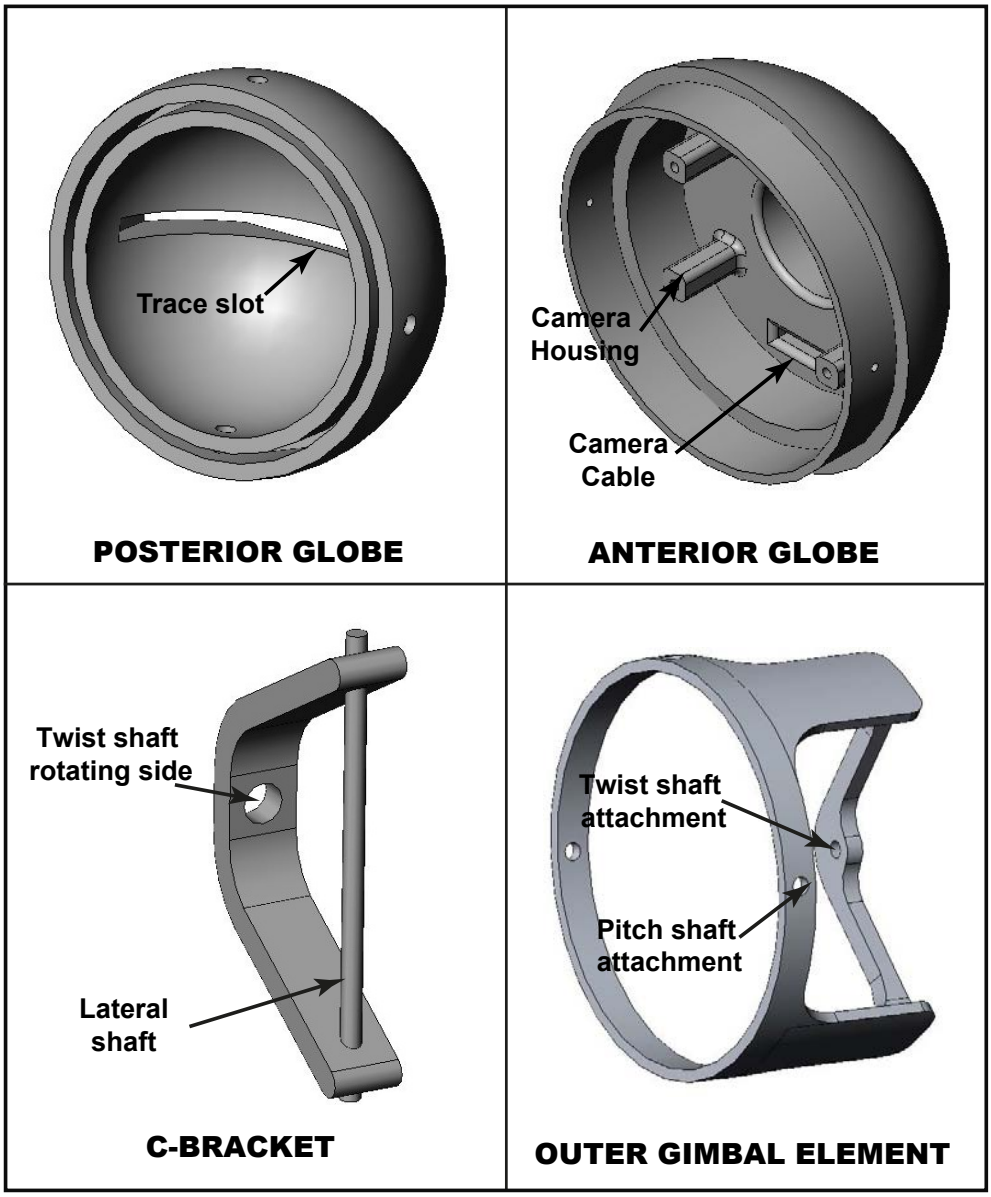

Figure A.10: Elements of first rapid prototype of the eye robot

E1D3 joints. Subsequent to selecting an appropriate globe size the C-bracket was designed to fit inside the empty space of the posterior globe and the outer ring diameter was optimized to minimize its moment arm without jeopardizing a clear routing of the cables.

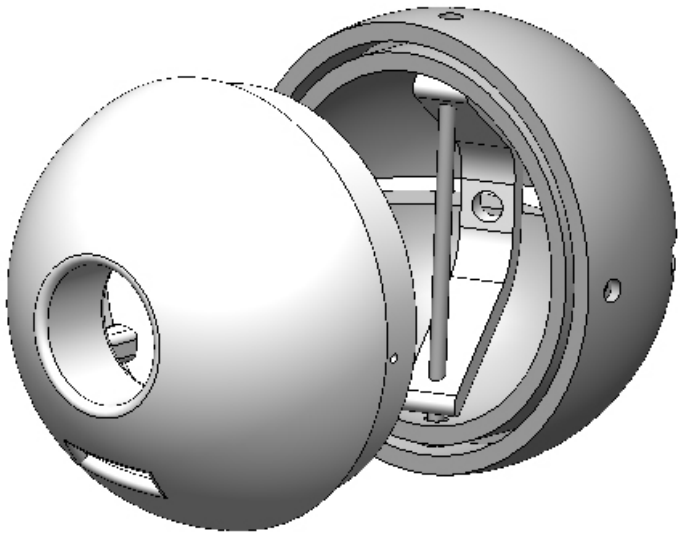

Figure A.11: Globe assembly

Table A.1: Joint details for the first rapid prototype of the eye robot

Rotational Direction	Fixed wrt	Rotates wrt	Fixed by	Rotational joint
Yaw	C bracket	Globe	Glued	Through Hole
Roll	Outer Ring	C Bracket	Threaded	Through Hole
Pitch	Outer Ring	Support Stand	Threaded	Through Hole

An important part of the detailed mechanical design includes studying the structural strength of the system, which is determined by the strength of the individual elements. Therefore, it is crucial that the entire gimbal structure withstands

the applied forces from the activated motors (transferred through the cables) without failing. Here, failure of a part is defined as a deflection of more than 0.1 mm, rather than the typically used yield strength of the material. This requirement is essential for providing a rigid and reliable support structure as well as ensuring a precise and purely rotational globe movement. For instance, if the outer ring was to be deflected to a point that the globe's centre would be shifted from that of the outer ring's, the rotational axes would no longer coincide and would therefore add an undesired translational portion to the globe's motion. To evaluate the structural strength of the this prototype the individual elements were examined under the maximum applied forces. This maximum was taken to be the force transferred to the specific element, when all the 6 motors are fully activated. If F_{max} , I_{max}, K_i, and R_{pulley} respectively represent, maximum motor force produced, maximum output current of the amplifier, motor torque constant, and motor pulley radius, then the maximum motor force can be described by the following relationship.

$$F_{max} = I_{max} K_i / R_{pulley} = 7\ N$$

The maximum applied force to the gimbal system is when all 6 cables are being pulled with the maximum calculated motor force of 7N. Considering this situation, the tension in the 4 recti are predominantly taken by the C-bracket, while those of the obliques are transferred through the outer ring, Figure A.12. Subsequently, the structural strength of the C-bracket and the outer ring were examined using Cosmos in Solid Works. The corresponding maximum deflection and factor of

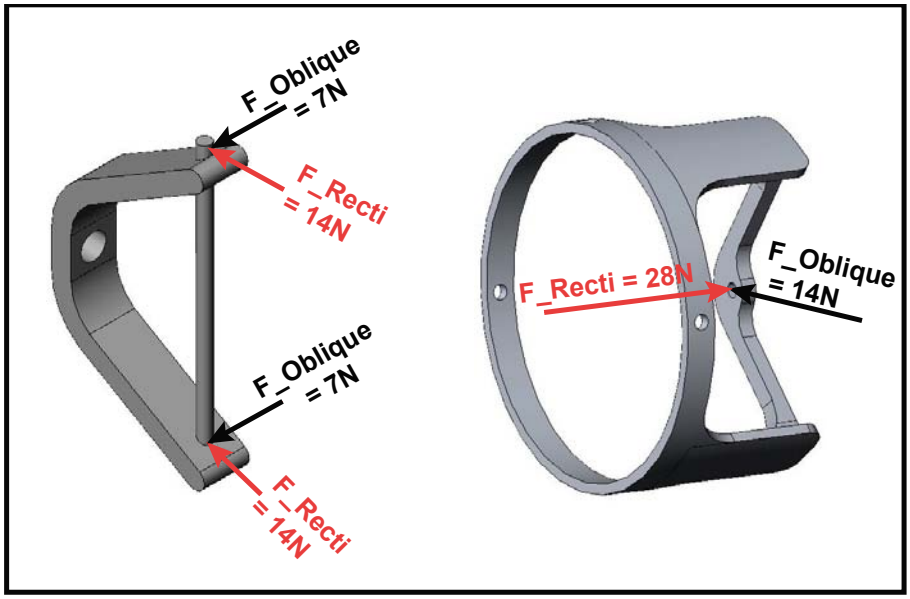

Figure A.12: Free body diagram of E1D3 gimbal elements

safety of the gimbal elements are summarized in Table A.2[1]. Considering, the unacceptably low ”deflection F.O.S.” of this prototype imposed the requirement of a new design. Furthermore, insufficient joint constraint caused undesired globe translation under activated motors and lack of bearing elements in the joints lead to high rotational friction. Consequently, the final eye robot, presented in Section 4.3, was designed to incorporate these requirements.

[1] The F.O.S of each element is calculated based on the 57 *MPa* yield strength of polycarbonate.

Table A.2: Performance of the eye robot prototype under the applied motor loads

Component	Maximum Deflection [mm]	F.O.S	Deflection F.O.S
C-bracket	1.74	1.85	0.057
Outer Gimbal Structure	4.9	1.81	0.02